MUNI
PŘÍRODOVĚDECKÁ
FAKULTA

PARTICLE-IN-CELL SIMULACE ELEKTRON-POZITRONOVÉHO CYKLOTRONOVÉHO MASERU

MATÚŠ LABAJ

Školitel: Mgr. Jan Benáček, Ph.D.
Ústav teoretické fyziky a astrofyziky
Přírodovědecká fakulta
Masarykova Univerzita

Brno – 2022

BIBLIOGRAFICKÝ ZÁZNAM

Autor:	Bc. Matúš Labaj Přírodovědecká fakulta, Masarykova Univerzita Ústav teoretické fyziky a astrofyziky

Název práce:	Particle-in-Cell simulace elektron-pozitronového cyklotronového maseru
Studijný program:	Fyzika
Obor:	Astrofyzika
Vedoucí práce:	Mgr. Jan Benáček, Ph.D.
Akademický rok:	2021/2022
Počet stran:	xii + 100
Klíčová slova:	pulzar, rádiová emise, particle-in-cell, simulace

BIBLIOGRAPHIC ENTRY

Author:	Bc. Matúš Labaj Faculty of Science, Masaryk University Department of Theoretical Physics and Astrophysics

Title of Thesis:	Particle-In-Cell Simulations of Electron-Positron Cyclotron Maser
Degree Programme:	Physics
Field of Study:	Astrophysics
Supervisor:	Mgr. Jan Benáček, Ph.D.
Academic Year:	2021/2022
Number of Pages:	xii + 100
Keywords:	pulsar, radio emission, particle-in-cell, simulations

ABSTRAKT

Pulzary jsou intenzivně zkoumaným typem neutronových hvězd. Jejich fyzikální procesy jsou jednou z otevřených otázek moderní astrofyziky. Pulzary vykazují silnou rádiovou emisi, avšak její mechanizmus je stále z velké časti nejasný. V této práci je zkoumaný jeden z navrhnutých mechanizmů, elektron–pozitronový cyklotronový maser, skrze studium plazmových vln vygenerovaných v Particle-In-Cell simulacích. Práce je rozdělená do třech častí. První část pojednává o historii pulzarů a fyzice neutronových hvězd, jako i o navrhnuté teorii elektron-cyklotronového maseru. Stručný souhrn principů metody Particle-In-Cell, numerický kód TRISTAN, jeho algoritmy a průběh simulace jsou popsaný v druhé časti. V třetí a zároveň poslední části jsou prezentovány použité konfigurace simulací a získané výsledky a je vysvětlena jejich fyzikální podstata.

ABSTRACT

Pulsars are widely investigated type of neutron stars. Their physical processes are one of the open questions of modern astrophysics. Pulsars exhibit strong radio emission; however, the emission mechanism remains largely uncertain. In this thesis, one of the proposed emission mechanisms, the electron–positron cyclotron maser, is investigated by studying the generated plasma waves using Particle-In-Cell simulation method. The thesis is divided into three parts. The first part introduces to the history of pulsars and the physics of neutron stars as well as the proposed electron-cyclotron maser theory. The second part briefly summarizes the Particle-In-Cell principles and presents the TRISTAN numerical code, its algorithms and simulation workflow. In the third and final part, the simulation setup is presented and the obtained results are put into physical perspective.

MUNI
SCI

MASARYKOVA UNIVERZITA
PŘÍRODOVĚDECKÁ FAKULTA
KOTLÁŘSKÁ 2, 611 37 BRNO
IČ: 00216224
DIČ: CZ00216224

ZADÁNÍ
DIPLOMOVÉ PRÁCE

Akademický rok: 2021/2022

Ústav:	Ústav teoretické fyziky a astrofyziky
Student:	Bc. Matúš Labaj
Program:	Fyzika
Specializace:	Astrofyzika

Ředitel *ústavu* PřF MU Vám ve smyslu Studijního a zkušebního řádu MU určuje diplomovou práci s názvem:

Název práce:	Particle-in-Cell simulace elektron-pozitronového cyklotronového maseru
Název práce anglicky:	Particle-in-Cell simulations of electron-positron cyclotron maser
Jazyk závěrečné práce:	angličtina

Oficiální zadání:
Elektron-cyklotronový maser je jedním ze základních emisních mechanizmů rádiového záření. Mechanismus využívám nejen pro interpretaci slunečních rádiových vzplanutí, spektrálních vlastností pulsarů a rádiové emise hvězd, ale i rychlých rádiových záblesků (Fast radio bursts, FRBs). Maser je předpokládá dvojnou plasmové resonanci mezi elektron plasmovou a cyklotronovou frekvencí v kombinaci s nestabilní distribuční funkcí. Přestože jsou emisní vlastnosti maseru velice dobře popsány pro elektron cyklotronovou frekvenci větší než plazmová frekvence, opačný případ má známá řešení pouze pro electron-iontové plasma s chladným pozaďovým plazmatem, které má mnohem větší hustotu než nestabilní loss-cone distribuce.

Cílem studenta je pomocí Particle-in-Cell simulace studovat efekty dvojné plazmové resonance a její disperzní vlastnosti pro případ elektron-pozitronového plazmatu jako funkcí teploty, poměru plazmové a cyklotronové frekvence, nebo poměru hustot mezi pozaďovou a loss-cone distribucí.

Postup:
- Studium základních vlastností dvojné plazmové resonance, vlastností a podmínek kinetické nestability
- Studium kódu Tristan a nastavení Particle-in-Cell simulace pro tuto nestabilitu
- Implementace a otestování počátečních podmínek v kódu na vybraném problému
- Provedení série simulací se změnami parametrů plazmatu na clusteru MetaCentrum nebo superclusteru IT4I
- Zpracování výstupních dat simulací, určení vlastností a evoluce nestability pomocí skriptů v Pythonu
- Porovnání se známými výsledky pro elektron-iontové plazma.

Literatura:
- Matsumoto & Omura, 1993, Tristan, https://www.terrapub.co.jp/e-library/cspp/pdf/03.pdf
- Treumann 2006, 2006, A&ARv, 13, 229
- Benáček & Karlický, 2018, A&A, 611, 60
- Li, Chen, Kong, Hosseinpour & Wang 2019, ApJ, 880, 31
- Ni, Chen, Li, Zhang, Ning, Kong, Wang & Hosseinpour, 2020, ApJL, 891, 25

Vedoucí práce:	Mgr. Jan Benáček, Ph.D.
Konzultant:	prof. RNDr. Marian Karlický, DrSc.
Datum zadání práce:	24. 1. 2021
V Brně dne:	30. 11. 2021

Bc. Matúš Labaj, 24. 1. 2021
Mgr. Jan Benáček, Ph.D., 25. 1. 2021
Mgr. Dušan Hemzal, Ph.D., 8. 2. 2021

ACKNOWLEDGEMENTS

First and foremost, I would like to express my deepest gratitude to Jan Benáček for being a great supervisor and a good friend. Without his insight, this thesis could not be brought to a close. I would also like to thank professor Karlický for his valuable comments regarding the scientific readiness of the thesis.

Next, I would like to thank IT4Innovations for providing me with computational resources as well as working experience with one of the finest supercomputers in Europe.

Last but not least, I am grateful for my family, who tirelessly supported me throughout my whole studies.

DECLARATION

Hereby I declare that I have prepared my diploma thesis independently under the guidance of the supervisor with the use of cited works.

Brno, 2022

Matúš Labaj

If you wish to make an apple pie from scratch,
you must first invent the universe.

— Carl Sagan, *Cosmos*

CONTENTS

LIST OF FIGURES

LIST OF TABLES

LIST OF SYMBOLS

$\mathbf{B}$	Magnetic field vector
c	Speed of light
$\mathbf{E}$	Electric field vector
e	Electron charge
f	Signal frequency; Particle velocity distribution function
f_{p}	Plasma frequency
f_{B}	Cyclotron frequency
$\mathbf{j}$	Electric current density
$\mathbf{k}$	Wave vector
l	Length
m_{e}	Electron mass
$M_{\odot}$	Solar mass
n_e	Electron density
n_{th}	Particle density of the thermal hot component
n_{bg}	Particle density of background plasma component
$\mathbf{r}$	Position vector
t	Time
$\mathbf{v}$	Velocity vector
v_{g}	Group velocity of a wave
v_{th}	Hot electron thermal velocity
v_{tb}	Background electron thermal velocity
ϵ_0	Permittivity of vacuum
ρ_e	Electric charge density
N	Refractive index
μ_0	Permeability of vacuum
ω	Frequency
ω_{pe}	Electron plasma frequency
ω_{ce}	Electron cyclotron frequency

INTRODUCTION

Since their first discovery nearly 50 years ago, pulsars still remain one of the hot topics of astrophysics. Pulsars, or neutron stars in general, can be thought of as *extreme conditions laboratories*: they possess the strongest magnetic fields in the known universe. Their mass density is so high, to be only exceeded by black holes themselves.

Even though pulsars have been subjected to intense research, there is still no consensus on the mechanisms behind many of its phenomena. The origin of their radio emission is one of these. Many radio mechanisms have been proposed in the past, but general agreement is yet to be reached.

The primary aim of the thesis is to look at the problem from the perspective of a certain radiation producing mechanism: the electron–positron cyclotron maser, investigated using high-performance numerical simulations.

The first part of the thesis consists of introduction to the history and physics of neutron stars further presented with the current knowledge (or proposed theory) about the internal structure, the magnetosphere, and ongoing processes of neutron stars. In the second part, fundamentals of the TRISTAN Particle-In-Cell code, the method used for our simulations, and the numerical implementation are presented. In the third and final part, we will discuss the setup of the simulations and obtained results, as well as propose what could be done in the future.

Part I

PULSARS

Possessing some of the strongest magnetic fields in the known universe, pulsars (from ***puls****ating* ***r****adio sources*) are widely investigated type of neutron stars. As their name implies, they generate radio waves. Even though there have been many proposed explanations, the mechanism of radio emission remains largely uncertain.

1 INTRODUCTION TO PULSARS

Pulsars - rapidly rotating and highly magnetized neutron stars - are fascinating objects to study. Even though they are only about 20 km in diameter, they weigh more than our Sun. Pulsars provide us with a wealth of information about not only neutron star physics but also general relativity, interstellar medium, and many others.

1.1 DISCOVERY OF PULSARS

Fritz Zwicky was also the first to infer the existence of dark matter.

The very first mention of neutron stars originated in 1934 when Baade and Zwicky (1934) proposed the possible existence of neutron stars as the endpoint of stellar evolution. Their prediction that neutron stars would possess a very small radius and an extremely high density, consisting mainly of neutrons, was at the time beyond any possibility of actual observation.

Before their observational discovery, further predictions of their extreme conditions were made. Oppenheimer and Volkoff (1939) used a simplified equation of state to predict its total mass, density, and diameter; Hoyle et al. (1964) proposed that the strength of the magnetic field of the neutron star in the center of *Crab Nebula* could be 10^{10} G; Pacini (1967), just before their discovery, proposed that the source of the energy in the Crab Nebula could be credited to the rapid rotation of the neutron star. However, no predictions were made of the immensely powerful *lighthouse* beam of radio waves.

Compact, dense stars, either white dwarfs or neutron stars, were independently predicted to be observable X-ray sources by Hayakawa & Matsouka and Guseynov & Zel'dovich in 1964 (discussed in Boyle, 1984). The first X-ray observations were of the Sun and the *Crab Nebula*. Eventually, more sources were discovered by the UHURU X-ray satellite, cataloged as Hercules X-1 and Centaurus X-3 (Giacconi et al., 1971).

Gamma-ray astronomy as a field was essentially started in the 1970s by satellites SAS-2 and COS-B. The technical difficulty was huge at the time because of the small amounts of photon flux that was hard to distinguish from the cosmic-ray particles. It was surprising to find pulsars in the gamma-ray band (discussed in Gurevich et al., 1993, Lyne and Graham-Smith, 2012).

Figure 1.1: Composite image of Crab Nebula showing the X-ray (blue) and optical (red) images superimposed. A pulsar lies in its centre (Hester, 2002).

1.1.1 *Discovery in Radio Band*

Radio astronomy experienced substantial growth in the decades following the Second World War. The first distinct radio source, Cygnus A, was discovered rather surprisingly during a radio background survey by Hey et al. (1948) for their meteor radar work. Pulsar signal transmission was recorded 10 years before their proper discovery; however, they were not recognized. The difficulty of the recognition was that radio astronomers did not expect that such a rapidly fluctuating signal could be attributed to any celestial source. The signal was instead regarded as some kind of radio interference, generated by human machinery, such as power line discharges or automobile ignition (discussed in Lyne and Graham-Smith, 2012).

1.1.2 *Study of Interplanetary Scintillation*

Scintillation is a phenomenon that causes particles (such as electrons or high-energy photons) passing through transparent material to occasionally flash due to random refraction. In radio astronomy, there are three distinct manifestations of the scintillation of radio waves coming from celestial sources:

A. refraction in the terrestrial ionosphere,

B. refraction in the ionized interplanetary gas in the Solar System,

c. refraction in the interstellar gas of the Milky Way.

Signal coming from a distant point source traverses through a medium with fluctuations of the refractive index. These fluctuations can deviate the paths of radio rays before they reach the observer, and interference may occur, leading to variations in signal strength.

All three types of scintillation were discovered and further investigated in Cambridge, where Anthony Hewish played a key role. Coincidentally, it was the investigation of interplanetary scintillation that led to the discovery of pulsars as a by-product of their research.

Today, Professor Bell-Burnell.

Hewish was working with a doctoral student, Jocelyn Bell, with whom they constructed a receiving antenna for a comparatively long radio wavelength of 3.7 m. At this wavelength, the effects of interplanetary scintillation are large, but they are limited only to sources with a very small angular diameter – it is, therefore, a distinct feature of the quasars, since the radio galaxies do not scintillate.

The discovery of pulsars was made by Jocelyn Bell in July 1967, a month after the start of regular recordings of radio signals. Large fluctuations of the signal were seen at almost the same time on successive days. Unexpectedly, the signal resembled terrestrial interference rather than scintillation (Figure 1.2a).

When a further investigation was conducted, the fluctuations occurred four minutes earlier each day, which could be attributed to a celestial source. By October 1967, Hewish concluded that something new was discovered. He and his colleagues used a recorder with a faster response time, and in November they recorded the now-famous regular pulses with a period of 1.337 s. As there was no explanation for the signal at the time, there were suspicions that the source is an extraterrestrial civilization. The discovery became a sensation with the public and the signal was nicknamed LGM-1: *Little Green Men 1* (discussed in Lyne and Graham-Smith, 2012).

1.1.3 *February 1968: The Nature Letter*

The official announcement of the discovery was published in *Nature* in February of 1968 (see Hewish et al., 1968). It contained a remarkable analysis of the signal pulses, which showed that the source truly lies outside the Solar System due to the Doppler effect of the Earth's motion on the pulse period. The rapid nature of the rotation implied that the source must be very small, presumably either a white dwarf or a neutron star. Interestingly, the letter points toward the neutron star as a possible signal origin even though at the time the mere existence of neutron stars was still only hypothetical. It is worth noting that at the time, the scientific community preferred the idea of a possible configuration of binary systems or white dwarf stars, as they were more familiar (discussed in Lyne and Graham-Smith, 2012).

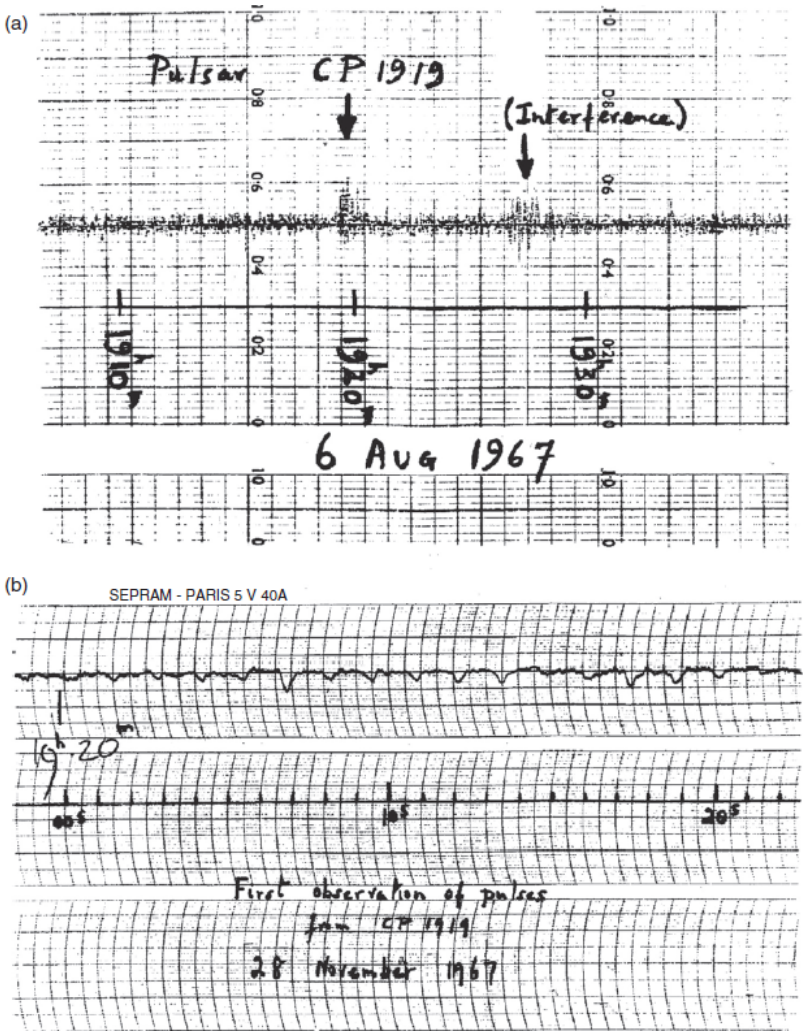

Figure 1.2: Discovery observations of the first pulsar. (a) The first recording of PSR B1919+21. (b) Recording of individual pulses (Hewish et al., 1968).

This was the first Nobel prize awarded in recognition of astronomical research.

For their discovery, Anthony Hewish and Martin Ryle (responsible for the instrumentation of the telescope) were awarded the 1974 Nobel Prize for Physics. Curiously, Jocelyn Bell, who discovered the signal, was not included as a laureate of the shared Nobel Prize.

1.1.4 *Notable Milestones in Pulsar Astronomy*

Over the years, pulsar research has been mainly driven by surveys using large radio telescopes. As well as contributing to a better understanding of neutron stars, these surveys discovered exciting new objects, such as binary pulsar systems. Apart from the pulsar discovery, other landmark discoveries so far are (per Lorimer et al., 2005):

- Discovery of the first binary pulsar B1913+16 by Hulse and Taylor (1975) at Arecibo in 1974. The pair orbits each other ev-

ery 7.75 h and will coalesce in about 200 Myr due to the loss of orbital energy emitted as gravitational radiation. The measurements of orbital shrinkage were the very first experimental demonstration of the existence of gravitational waves. Hulse and Taylor received the 1993 Nobel Prize for Physics in recognition of their discovery.

- Discovery of the first millisecond pulsar B1937+21 by Backer et al. (1983). This remarkable neutron star rotates at a frequency of 642 Hz, which is very close to the theoretical rotation limit. Its rotational period is very stable, making the pulsar an effective clock for short timescales. Up until the discovery of J1748–2446ad (Hessels et al., 2006), it was the fastest spinning neutron star known to date.

- The first pulsar planetary system B1257+12 was discovered by Wolszczan and Frail (1992) at Arecibo in 1990. The system consists of two planets of Earth-like mass and one planet of lunar mass, becoming the very first extra-solar planetary system to be discovered.

Figure 1.3: Arecibo Observatory, Puerto Rico. Many of the key discoveries regarding pulsars were made here. Unfortunately, it is out of commission from 2020 due to collapse of the telescope (Shostak, 1981).

1.2 PULSAR CHARACTERISTICS

Following their discovery in 1967, pulsars were shortly identified as rotating neutron stars. After nearly five decades of observations, roughly 2600 pulsars are known to this date (Manchester, 2017). With

the current state of our knowledge, we can put constraints on its emission properties, used for explanation of the radio emission; propagation of the signal as it passes through the interstellar medium; properties of pulsar population and their implications for the neutron star population in galaxies.

1.2.1 *Emission Properties*

The emission properties of pulsars are commonly explained using the framework of emission produced by the acceleration of charged particles. The standard interpretation of the pulses is that they are produced by the so-called *Lighthouse effect*: an emission beam of a neutron star is observed once per rotation as it sweeps past our line of sight, with its intensity strongly depending on the inclination angle. The emission mechanisms will be discussed in greater detail in Chapter 2.

1.2.2 *Pulse Profiles*

The periodicity of the pulses directly relates to the angular velocity of the neutron star. The most rapidly rotating neutron is PSR J1748–2446ad (Hessels et al., 2006) with a pulse period of only 1.40 ms. In contrast, the PSR J2144-3933 (Young et al., 1999) has a period of 8.5 s, which is the longest period observed so far.

Pulsars are very weak radio sources; therefore, even with the use of the most modern technology, individual pulses of only the strongest sources are observable. For most pulsars, observations are done by folding thousands of pulses together, becoming *integrated pulse profile* (see Figure 1.4). To achieve a stable integrated pulse profile, at least a few hundred to a few thousand pulse periods are required.

It is apparent from Figure 1.4 that the shapes of the pulses vary considerably. In the simplest case (B1933+16), the pulse consists of a single component, reminiscent of a Gaussian peak. Many pulsars possess characteristic double-peaked profiles, such as B1913+16. Although initially thought that millisecond pulsars were more complex than normal ones, observations show that the number of pulse components is comparable. On average, normal pulsars have 3±1 pulse components and millisecond pulsars have 4±1 components (Kramer et al., 1998).

Although pulse profiles tend to be very stable from epoch to epoch, there are some important exceptions. There have been observations that a change could be caused by a change in the orientation of the radio beam to the observer by some kind of precession (Kramer et al., 1998), or by a transition between pulse shapes.

The shape of the profile is also highly dependent on the frequency of observation (see Figure 1.5). Most of the normal pulsars (B1133+16

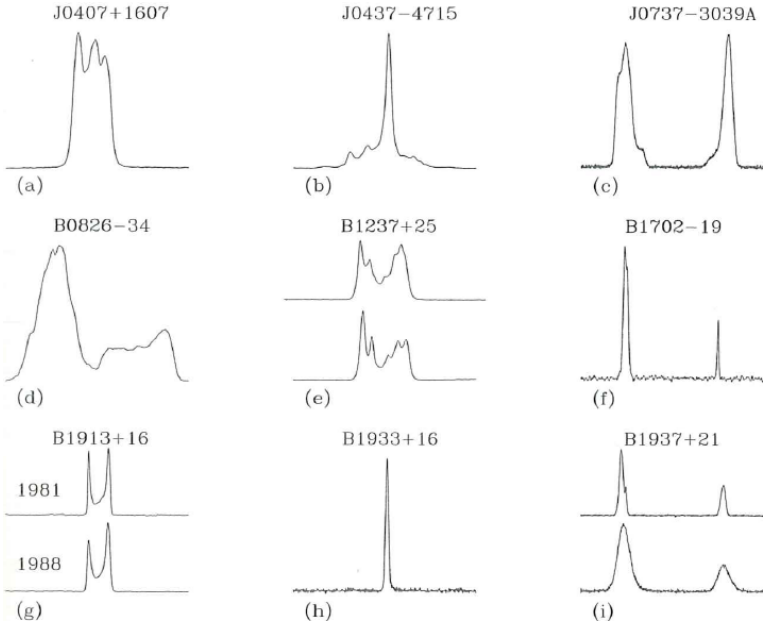

Figure 1.4: Integrated pulse profiles of nine pulsars. Except for B1237+25, each profile shows 360° of rotational phase. For B1237+25, two profiles at 430 MHz are shown, taken at separate epochs (Lorimer et al., 2005).

in Figure 1.5) show an increase in pulse width and separation of profile components with decreasing observing frequency. On the contrary, millisecond pulsars (J2145-0750 in Figure 1.5) show very little evolution with decreasing frequency. These changes are related to geometrical factors and a different spectral index of emitting regions. The reasoning behind the less pronounced changes in pulse profiles of millisecond pulsars is consistent with the idea that their emission region is much smaller than that of normal pulsars (discussed in Lorimer et al., 2005).

1.2.3 *Propagation Through Interstellar Medium*

As stated before, the construction of the radio telescope by Hewish, Ryle, and Bell, which led to the discovery of pulsars, was motivated by the study of the scintillation of radio waves in the interplanetary gas of the Solar System. The pulsar signal was discovered due to diffraction in the interstellar medium. This effect was later joined by other important propagation effects: dispersion, Faraday rotation, and scattering.

1.2.3.1 *Dispersion*

As implied in the discovery paper by Hewish et al. (1968), pulses observed at higher frequencies arrive earlier than their lower-frequency counterparts. This delay is caused by *dispersion*. The pulse delay is

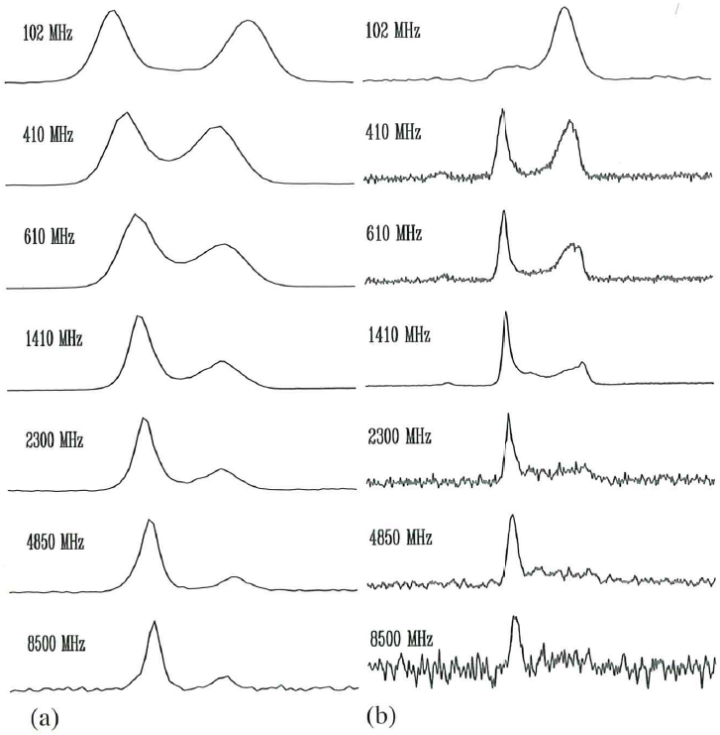

Figure 1.5: Multi-frequency pulse profiles for (a) B1133+16 with 1.16 s period; (b) J2145-0750 with 16 ms period (Lorimer et al., 2005).

inversely proportional to the observing frequency, with the proportionality constant known as *dispersion measure* (DM).

Propagation of a radio signal along a length path d from the pulsar to Earth will be subject to a time delay t with respect to a signal of infinite frequency:

$$t = \left(\int_0^d \frac{\mathrm{d}l}{v_\mathrm{g}} \right) - \frac{d}{c}. \tag{1.1}$$

Expanding the term for group velocity using the refractive index (see Lorimer et al., 2005, p. 86)

$$v_\mathrm{g} = cN = c\sqrt{1 - \left(\frac{f_p}{f}\right)^2}, \tag{1.2}$$

the signal delay can be written as

$$t = \frac{e^2}{2m_\mathrm{e}c} \frac{\int_0^d n_\mathrm{e}\mathrm{d}l}{f^2} = C\frac{\mathrm{DM}}{f^2}, \tag{1.3}$$

where dispersion measure DM is

$$\mathrm{DM} = \int_0^d n_\mathrm{e}\mathrm{d}l. \tag{1.4}$$

Dispersion measure is effectively integrated column density of electrons between the pulsar and the observer, with units being $\mathrm{cm}^{-3}\mathrm{pc}$.

DM is essential for estimating pulsar distances. From the measurement of the pulse arrival time at two or more frequencies, we can infer DM. Then the parameter can be used, with the assumption of a model Galactic density distribution, to estimate the distance (discussed in Lorimer et al., 2005).

1.2.3.2 *Faraday Rotation*

The discovery of a high degree of linear polarization in pulsar radio signals by Lyne and Smith (1968) led to one of the most direct way of measuring the interstellar magnetic field through an effect called *Faraday rotation*.

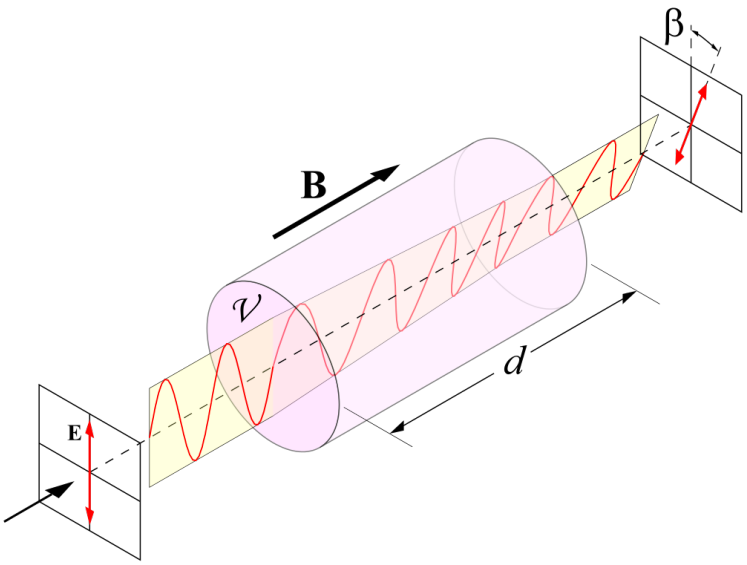

Figure 1.6: Scheme of polarization mechanism caused by Faraday rotation (Wikipedia, 2007).

The pulse delay, dependant on the frequency, can also be expressed using phase rotation. The phase of the pulse observed at infinite frequency, therefore without delay, differs from the pulse at a frequency f by phase lag $\Delta\Psi = -\mathrm{k}d$. Faraday rotation is expressed as phase difference between right and left polarization

$$\Delta\Psi_{\text{Faraday}} = \int_0^d (k_{\mathrm{R}} - k_{\mathrm{L}})\mathrm{d}l. \tag{1.5}$$

The wave number $k = 2\pi/\lambda$ can be written for the case of cold magnetised plasma as

$$\mathrm{k}(f) = \frac{2\pi}{c} f \sqrt{1 - \frac{f_p}{f^2} \mp \frac{f_p^2 f_B}{f^3}}. \tag{1.6}$$

Since $f \gg f_p$ and $f \gg f_B$, we can write

$$\Delta\Psi_{\text{Faraday}} = \frac{e^3}{\pi m_{\mathrm{e}}^2 c^2 f^2} \int_0^d n_{\mathrm{e}} B_{\parallel} \mathrm{d}l. \tag{1.7}$$

As the polarization position angle (PPA) is periodic on π rather than 2π for phase, the change in PPA can be written as

$$\Delta\Psi_{\mathrm{PPA}} = \Delta\Psi_{\mathrm{Faraday}}/2 \equiv \lambda^2 \times \mathrm{RM}, \tag{1.8}$$

where the *rotation measure* RM is defined as

$$\mathrm{RM} = \frac{e^3}{2\pi m_e^2 c^4} \int_0^d n_e B_\parallel \mathrm{d}l. \tag{1.9}$$

By combining both measurements of the rotation measure RM and the dispersion measure DM, the average magnetic field strength weighted by the electron density along the line of sight can be written as (Lorimer et al., 2005)

$$\langle \mathrm{B}_\parallel \rangle \equiv \frac{\int_0^d n_e B_\parallel \mathrm{d}l}{\int_0^d n_e \mathrm{d}l} = 1.23\mu G \left(\frac{\mathrm{RM}}{\mathrm{rad\,m^{-2}}}\right)\left(\frac{\mathrm{DM}}{\mathrm{cm^{-3}pc}}\right)^{-1}. \tag{1.10}$$

1.2.4 *Pulsar Population*

Most of the known pulsars so far lie in the Milky Way. Normal pulsars show a clear concentration towards the galactic plane, whereas the millisecond pulsars, mainly detectable at smaller distances than normal pulsars, are spread more isotropically. This fact implies that the normal pulsars must therefore be Galactic objects of young age, and their distribution should presumably be similar to that of the distribution of young massive stars and supernovae. This is consistent with the standard picture of the birth of neutron stars in the core-collapse supernovae of massive stars.

The first large-scale surveys of the sky were rather insensitive and thus only gave sparse evidence. For example, a survey carried out by Large and Vaughan (1971) managed to find only 29 pulsars in 7 steradians of the southern sky. Nonetheless, by combining this catalog with works of others, it was shown that there must be 10^5 active pulsars in the Galaxy at the very least.

The distribution of the first 1600 normal pulsars to be discovered is shown in Figure 1.7. The concentration is favored along the plane of the galaxy. On the contrary, as seen in Figure 1.8, the millisecond pulsars distribution is more isotropic. Due to large scattering effects, millisecond pulsars are much more biased towards observational biases. Subsequently, mostly local (up to 3 kpc away) millisecond pulsars are detected, which are responsible for the isotropic appearance of their distribution.

In addition to the different spin behavior between normal and millisecond pulsars, another important difference is the preference of millisecond pulsars to exist in binary systems. In about 80% of all millisecond pulsars, orbiting companions are observed, while in the case of normal pulsars, only 1 percent is binary. These companions

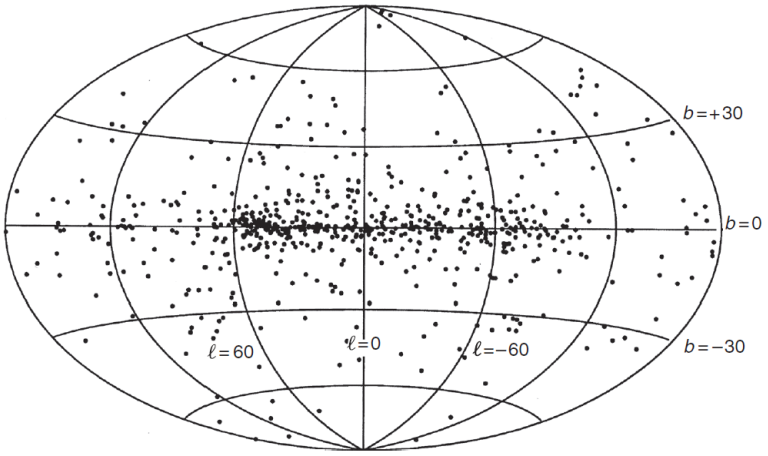

Figure 1.7: Distribution of the known normal pulsars on the sky in Galactic coordinates l, b. Its concentration towards the Galactic plane is apparent (Lyne and Graham-Smith, 2012).

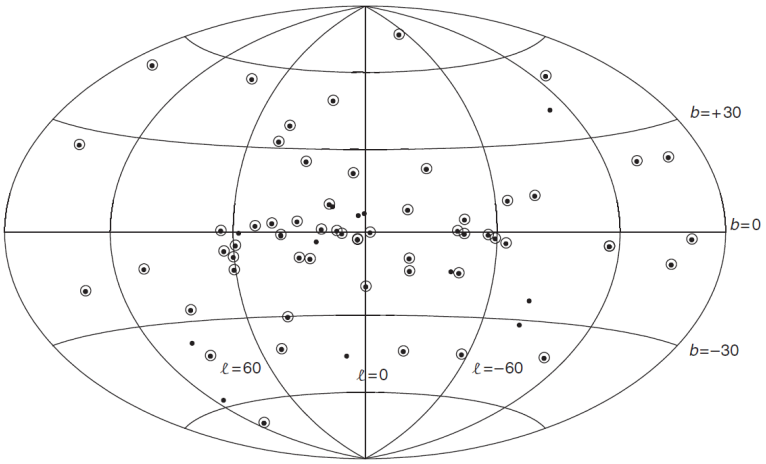

Figure 1.8: Distribution of the known millisecond and binary pulsars on the sky in Galactic coordinates l, b. The distribution is more isotropic that that of normal pulsars (Lyne and Graham-Smith, 2012).

are white dwarfs, main-sequence stars, or other neutron stars. The existence of binaries can be explained with a simple evolutionary scenario, which starts with two main-sequence stars (see Bhattacharya and van den Heuvel, 1991). The initially more massive star evolves first due to mass transfer from the second star and eventually explodes in a supernova, forming a neutron star (discussed in Lorimer et al., 2005 and Lyne and Graham-Smith, 2012).

2

STRUCTURE AND PROPERTIES OF A NEUTRON STAR

The neutron star's internal structure, as well as the structures of its atmosphere, magnetic and electric fields, its surroundings, and emission mechanisms, are still on the list of unsolved problems until this day and our understanding of them is still insufficient. Their internal composition, the equation of state, was first addressed by Oppenheimer and Volkoff (1939). Even though much progress has been made, older ideas are overcome with new ones on a yearly basis. This chapter, therefore, aims to present a theoretical background on a rather introductory level that explains some of the observed neutron star properties and effects, as well as present the relevant emission mechanisms. All equations stated in this chapter are expressed in CGS units.

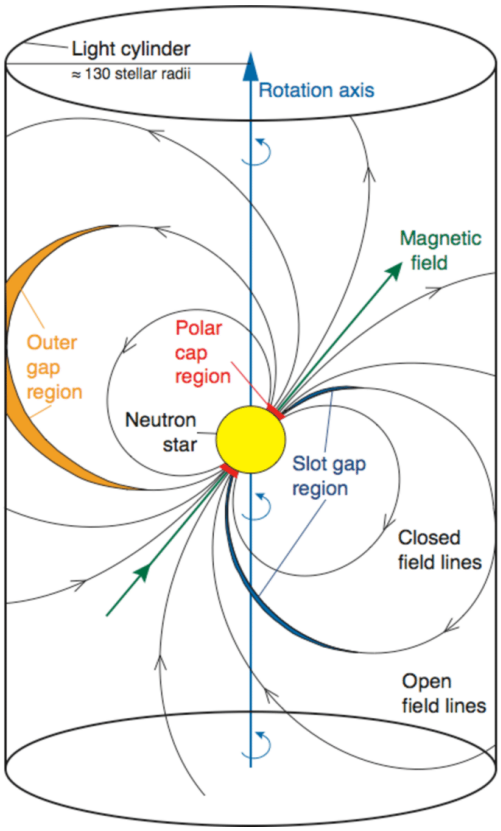

Figure 2.1: Model of a pulsar and its magnetosphere. Sketch is only illustrative and not to scale (Aliu et al., 2008).

2.1 NEUTRON STAR

Once a normal star has exhausted its sources of energy, it collapses with its gravity. For the case of heavy stars, this can result in three possible states – white dwarf, neutron star, or black hole, depending on the core mass of the progenitor star. The mass range for the neutron star progenitors is roughly in the range of about 8 to 20 solar masses.

2.1.1 *Mass and Radius*

The conditions under which a neutron star exists are very extreme and impossible to replicate and study in laboratories. Any calculation of neutron star properties therefore inherently carries necessary uncertainty. Models typically predict an upper mass limit of about 2 solar masses, which can increase due to the presence of a strong magnetic field (Cardall et al., 2001). Direct and comparatively accurate measurements of neutron star masses come from timing observations of binary pulsars (for a summary of the measurements, see Stairs, 2004). The measurements are in good agreement with the typical assumed pulsar mass of $1.4\,\mathrm{M}_\odot$.

On the contrary, accurate measurements of neutron star radii are immensely difficult to obtain. Methods are quite complex. One way is to observe the thermal emission from the neutron star surface at optical and X-ray frequencies, where the observed luminosity can be used to derive the size of the emitting region. However, calculations are complicated by the effects of strong gravity and magnetic field. The theoretical lower limit for the neutron star radius was derived by Glendenning (1992):

$$R_{\mathrm{min}} \simeq 1.5 R_{\mathrm{S}} = \frac{3GM}{c^2} = 6.2\,\mathrm{km}\left(\frac{M}{M_\odot}\right), \tag{2.1}$$

where R_{S} is the *Schwarzschild radius*

$$R_{\mathrm{S}} = \frac{2GM}{c^2} \simeq 4.2\,\mathrm{km}\left(\frac{M}{M_\odot}\right). \tag{2.2}$$

The upper limit was conversely obtained from requirement that the neutron star must be stable against break-up due to centrifugal forces caused by its rotation. Given a neutron star with a rotational period P, this can be written as (Lorimer et al., 2005, p. 58)

$$R_{\mathrm{max}} \simeq \left(\frac{GMP^2}{4\pi^2}\right)^{1/3} = 16.8\,\mathrm{km}\left(\frac{M}{1.4M_\odot}\right)^{1/3}\left(\frac{P}{\mathrm{ms}}\right)^{2/3}. \tag{2.3}$$

The fastest rotating pulsar known, J1748–2446ad, rotates with period of 1.40 ms, providing R_{max} limit value of 21.5 km for mass of $1.35\,\mathrm{M}_\odot$. Most theoretical models (summarised in Lattimer and Prakash, 2001)

predict a radius of $R \approx 10 - 12$ km, which is notably only around 3 times larger than the Schwarzschild radius, demonstrating the closeness of neutron stars and black holes (discussed in Lorimer et al., 2005 and Lyne and Graham-Smith, 2012).

2.1.2 *Internal Structure*

At the current state of knowledge, it is believed that there are two main structural components in a neutron star (Lyne and Graham-Smith, 2012): a crystalline solid crust, thick around 1 km, and an interior consisting of neutron liquid (see Figure 2.2). The border at which these regions divide is at a density near $2.7 \cdot 10^{14}$ g $\cdot$ cm^{-3} - the density of nuclear matter. Between the surface of the crust and the central core of the star, the density increases by an order of nine magnitudes, from the density of 10^6 to 10^{15} g $\cdot$ cm^{-3}.

The outer crust is covered by a rigid crystalline lattice consisting primarily of iron nuclei. Going deeper into the star, the density increases, and it becomes energetically favorable for electrons to penetrate the nuclei and combine with protons to form neutrons (summarised by Pethick and Ravenhall, 1991).

Internal regions of the star are filled with neutron fluid. This fluid along with co-existing proton fluid are both superfluids, bearing no viscosity.

Even deeper regions may contain further exotic states of matter, as the neutrons may be squeezed to form mesons or kaons, resulting in creation of solid core. Furthermore, state transition, where neutrons dissolve into quarks and gluons, is proposed (discussed in Lyne and Graham-Smith, 2012).

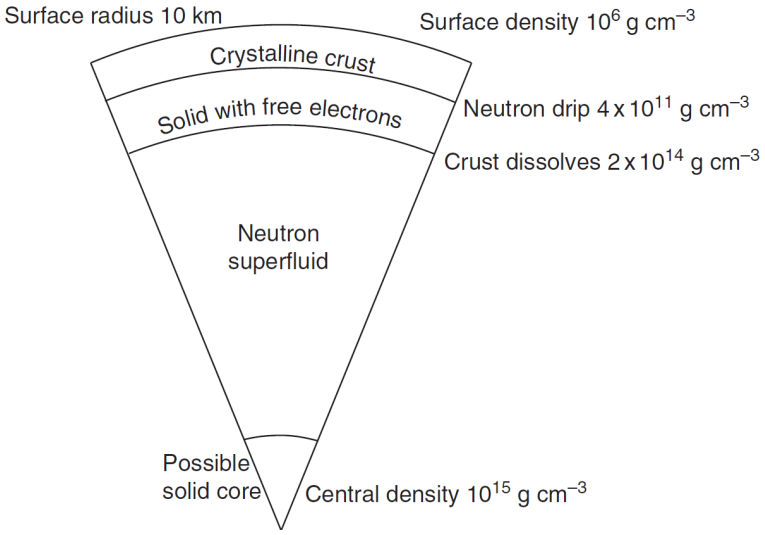

Figure 2.2: Cross-section of a typical neutron star model (Lyne and Graham-Smith, 2012).

2.1.3 *Magnetic Fields*

One of the signature features of pulsars is their enormous magnetic field. The dipole field strength of pulsars is consistent with the collapse of a normal star with a polar field of around 100 G. As the star collapses during supernova explosions, its effective field surface becomes lower, resulting in an increase in magnetic field strength to conserve magnetic flux. Considering that the proton component of the neutron fluid is superconducting, the decay time of the magnetic field is very long compared with the estimated life of pulsars.

1 tesla = 10 000 gauss.

Inside normal pulsars, polar field strengths of order 10^{10} to 10^{12} G are found. The magnetic fields of the most magnetized neutron stars, called *magnetars*, reach values of 10^{15} G, making them the strongest fields in the known universe. On the other hand, the weakest fields in the neutron star category are attributed to the older millisecond pulsars. In this case, the field strength can go as low as 10^8 G.

To put things into perspective, the strongest magnetic field ever achieved in a terrestrial laboratory is $4.55 \cdot 10^5$ G (Hahn et al., 2019).

Although the intensity of the magnetic field is tremendous, its effect on the overall structural properties of the star is negligible. Even though the magnetic energy density is very high, when converted to equivalent matter density, a density matter of order 1 $\mathrm{kg} \cdot \mathrm{cm}^{-3}$ is obtained. This value is significantly lower than the typical matter density of 10^{12} $\mathrm{kg} \cdot \mathrm{cm}^{-3}$, resulting only in a slight modification of the crystal structure near the star's surface (Chen et al., 1974).

The most evident effect of the strong magnetic field presence is the slowdown of the rotation (an increase in the rotational period). The effect propagates through the loss of angular momentum in electromagnetic radiation at the rotation frequency of the magnetic dipole. In fact, the slowdown rate is used as a measure of the magnetic field (discussed in Lorimer et al., 2005, Lyne and Graham-Smith, 2012).

2.2 MAGNETOSPHERE OF PULSARS

Outside the star, all physical processes are dominated by the magnetic field. Magnetic force even outweighs the gravitational by a very large factor: the ratio between gravitational force and induced electrostatic force on an electron near the surface,

$$\frac{GMm}{r^2} \Big/ \frac{e\Omega r B}{c}, \tag{2.4}$$

is of order 10^{-12} for the Crab Nebula pulsar. The external magnetic field is usually substantially misaligned with the axis of rotation. Subsequently, the poles generate electromagnetic waves radiating at rotational frequency, which is responsible for the loss of rotational energy that causes the observed slowdown (discussed in Lyne and Graham-Smith, 2012).

2.2.1 *Induced Electric Field*

As stated above, the magnetic field **B** is very strong near the surface. As the electrical conductivity of the star is very large, the magnetic field may be assumed to be *frozen-in* the neutron star. Consequently, the internal regions of the star must hold the condition

$$\mathbf{E_{in}} + \frac{1}{c}(\mathbf{\Omega} \times \mathbf{r}) \times \mathbf{B_{in}} = 0, \tag{2.5}$$

where **r** is the radius vector from the centre of the star and **Ω** is angular rotation velocity. Due to the high rotation of the star with strong magnetic field, the electric field **E**, caused by charge redistribution inside the pulsar, arises. The electric field is in the same order of magnitude as magnetic field: on the star surface, E is around $10^{12}\,\mathrm{V}\cdot\mathrm{cm}^{-1}$.

Particles that are situated in such a strong electric field are accelerated along the curvilinear magnetic field to very high energies and emit gamma-ray quanta. Gamma-ray quanta are absorbed in the magnetic field, generating electron–positron pairs,

$$\gamma \rightarrow \mathrm{e}_+ + \mathrm{e}_-. \tag{2.6}$$

Thus, the plasma with which the magnetosphere is eventually filled consists mainly of electrons and positrons. The newly created plasma in the magnetosphere screens the longitudinal electric field. Furthermore, the plasma starts to rotate with the star as a solid body. This phenomenon, called *corotation*, is also observed in the terrestrial or Jupiter's magnetospheres.

The corotation of the plasma is induced by the electric field

$$\mathbf{E_c} = -\frac{1}{c}(\mathbf{\Omega} \times \mathbf{r}) \times \mathbf{B}. \tag{2.7}$$

This field $\mathbf{E_c}$ is generated by the polarization of plasma, characterized by the corotation charge density, also called *Goldreich–Julian density* (Goldreich and Julian, 1969),

$$\rho_c = \frac{1}{4\pi}\mathrm{div}\,\mathbf{E_c} = -\frac{\mathbf{\Omega B}}{2\pi c}, \qquad n_c = \frac{|\rho_\mathbf{c}|}{|e|} = \frac{\mathbf{\Omega B}}{2\pi c|e|}. \tag{2.8}$$

The particle density n_c is particularly high compared to Earth's magnetosphere: pulsar magnetosphere density is $\approx 10^{12}\,\mathrm{cm}^{-3}$ while in Earth's case it is only about $10^{-6}\,\mathrm{cm}^{-3}$ (Gurevich et al., 1993, p. 94). Corotation density (same as magnetic field) decreases rapidly with increasing distance from the star

$$n_c(r) \simeq n_c(R)\left(\frac{r}{R}\right)^{-3}. \tag{2.9}$$

Plasma can corotate with the star only to a distance R_L,

$$R_L = \frac{c}{\Omega}, \tag{2.10}$$

as the fields cannot propagate faster than the speed of light (see Figure 2.3). This quantity dictates the characteristic size of the magnetosphere and is commonly several thousand times larger than the pulsar radius (discussed in Gurevich et al., 1993).

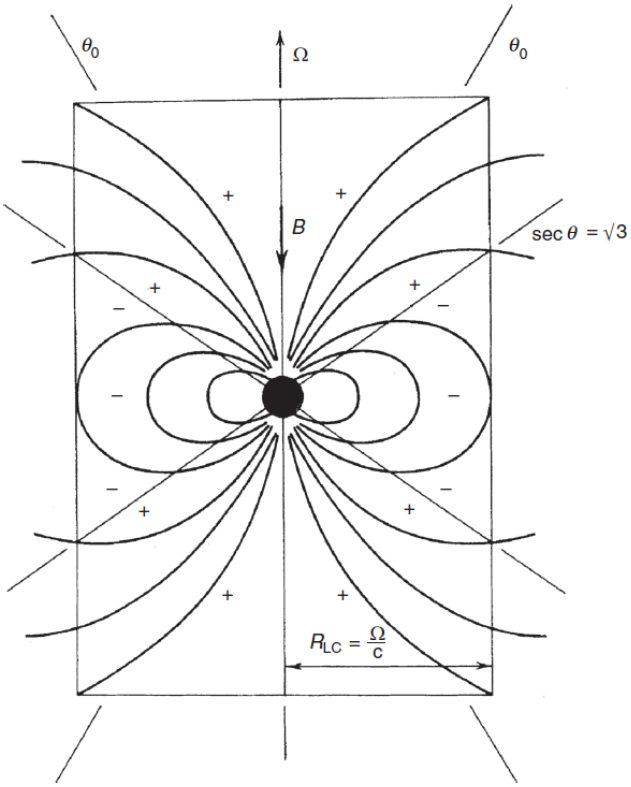

Figure 2.3: Magnetosphere of the Goldreich–Julian model showing the light cylinder at the distance R_L. Neutral surface at $\sec\theta = \sqrt{3}$ divides the positive and negative charge regions (Lyne and Graham-Smith, 2012).

2.2.2 *Magnetic Field Structure*

Electric currents have a deforming effect on the magnetic field of the neutron star. Although not as substantial near the star's surface, these effects become very influential at larger distances.

The distance, where the speed of plasma reaches the speed of light, is called *light cylinder radius*. As stated in (2.10), at this distance, the plasma cannot corotate anymore with the star. The existence of a light cylinder divides the assumed bipolar magnetic field lines into two groups (see Figure 2.4):

A. Closed field lines that close within the radius of the light cylinder,

B. Open field lines that do not close and extend further away from the star.

The region of open field lines defines the *polar cap* of the star. This region is rather small (see Lorimer et al., 2005, p. 66):

$$R_{\mathrm{p}} \simeq R \sin\theta_{\mathrm{p}} = \sqrt{\frac{2\pi R^3}{cP}} = 150\,\mathrm{m}\left(\frac{P}{\mathrm{s}}\right)^{-1/2}, \tag{2.11}$$

where the radius of the polar cap R_{p} is given by the boundary of the last open field line (R, θ_{p}).

Although the Goldreich–Julian model is not entirely realistic (see Michel, 2004), it illustrates some basic principles that are vital for understanding the pulsar observations. While the model expects the overall magnetic structure to be dipolar, in reality some multipole configuration could be the case.

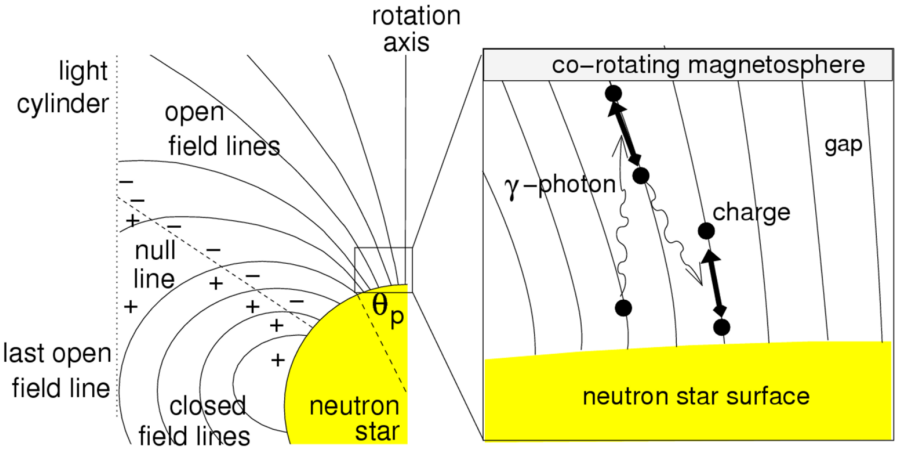

Figure 2.4: Magnetosphere of the Goldreich-Julian model. (a) closed and open field lines divide at the light cylinder radius; (b) scheme of electron-positron pair cascades at the polar gap region (Lorimer et al., 2005).

2.2.3 *Electron-Positron Plasma Generation*

As per Sturrock (1971), the plasma generation process is as follows. Due to the strong electric field at the surface of the star, plasma escapes along the open field lines of the magnetic field. Owing to this, a significant potential difference appears near the polar cap. The longitudinal electric field then accelerates the particles, which move along the strong magnetic field. Since the magnetic field is curvilinear, once particles acquire sufficient energy they start emitting high-energy curvature photons.

These photons are radiated in the same direction as the motion of the particles. Once the electron-positron pair is created, the positron goes away from the star, while the electron becomes accelerated by the electric field in the opposite direction. This is critical for the pair-producing chain reaction because this accelerated electron can also

radiate high-energy photons that can eventually produce pairs. Repeating the process leads to chain multiplication of electron-positron plasma and gamma-ray quanta near the star (see Figure 2.4b).

2.2.3.1 *Double Layer*

The existence of a significant potential difference between the surface of the star and its magnetosphere provides a natural layer near the surface, where there is a strong electric field. The layer, often called *double layer*, does not contain any plasma due to its escape along the magnetic field lines. In this layer, the particles acquire the necessary energy required for radiation of curvature photons; therefore, the existence of the double layer is critical for the generation of an electron-positron plasma. In the literature, the suitable size of this double layer is often called *pulsar ignition condition*.

2.2.3.2 *Secondary Plasma*

At high energies, another process leads to a cascade production of electron-positron pairs: the *synchrotron radiation*. After the curvature photons are absorbed, they generate electron-positron pairs, which is the first generation of produced plasma. The electrons and positrons are at the non-zero Landau level in the strong magnetic field of the neutron star. Subsequently, within a very short time of $\approx 10^{-19}$ s, they pass to a zero level and emit synchrophotons, whose energy is usually several times lower than that of the curvature photon. Pair production by synchrophotons then gives the second generation of plasma. This process also results in further production of synchrophotons with energy again lower than that of the previous generation by about the order of magnitude. Usually, plasma generation stops in the second, and sometimes in the third, generation (discussed in Gurevich et al., 1993).

2.3 EMISSION PROCESSES

Apart from the thermal radiation observable in the X-ray bandwidth from the star surface, the sources of radiation are located in two different regions of the magnetosphere: the *polar gap* and the *outer gap*. Outside these two regions, the electric field induced by the rotating dipole is shielded by the charged plasma.

The outer gap is a surface situated adjacently to the open magnetic field lines and extending to and beyond the light cylinder. Electrons or positrons, accelerated within the gap, generate gamma-ray photons at the highest observable energies.

Even though the mechanism of the coherent radio emission is not yet understood, its origin can be deduced from the integrated pulse

profiles. Most normal pulsars radiate radio emission from the polar cap, while, in the case of young pulsars, it originates in the outer gap.

Pulsars essentially radiate in three regimes:

A. thermal radiation from the neutron star surface generally observed in X-ray,

B. beamed incoherent curvature emission from electron-positron plasma in the outer gaps,

C. beamed coherent radio emission from electrons and positrons located in polar caps as well as outer gaps.

The obvious distinction in the radiation processes is the fact that the radio emission must be coherent to produce the observed very high brightness temperatures. There is no general agreement on the nature of the radio emission. Some of the mechanisms suggested for the observed non-thermal high-energy emission are synchrotron radiation, curvature radiation, and inverse Compton scattering.

Brightness temperature refers to the temperature at which a black body would have to be to produce the observed radiation intensity.

2.3.1 *Cyclotron Radiation*

Charged particles (with charge e and mass m) move on a circular path around the magnetic field at the *Larmor frequency* ω_{L}

$$\omega_{\mathrm{L}} = \frac{eB}{2\pi mc}. \tag{2.12}$$

For the case of electrons and positrons, $\omega_{\mathrm{L}} = 2.8\,\mathrm{MHz}\cdot\mathrm{G}^{-1}$. The energy loss rate due to cyclotron radiation is

$$\frac{\mathrm{d}E}{\mathrm{d}t} = -\frac{8\pi^2}{3}\frac{\omega_{\mathrm{L}}^2\beta^2 e^2}{c}, \tag{2.13}$$

where the velocity of the charged particle is written in the term of βc. Assuming typical radio frequency of 100 MHz, the loss rate using (2.13) is $2.03\times10^{-19}\beta^2$ W. This mechanism occurs at very large frequencies due to high intensities of magnetic fields. Classical cyclotron emission occurs at the cyclotron frequency (Lyne and Graham-Smith, 2012).

$\beta^2 = \frac{v^2}{c^2}$.

2.3.2 *Synchrotron Radiation*

Charged particles gyrating in a magnetic field with relativistic velocity ($\beta \sim 1$) radiate a spectrum that can extend to very high harmonics of the Larmor frequency ω_{L}. This mechanism is called synchrotron radiation. The theory of synchrotron radiation has been presented by Ginzburg and Syrovatskii (1965). Since the detailed interpretation of the mechanism is very complex, only the base idea will be presented.

Also known as magnetobremsstrahlung.

Considering the electric field radiated by a single electron, which is gyrating in the magnetic field, the field consists of pulses that occur continuously as the electron moves towards the observer. Due to the relativistic velocity of the particles, particles emit radiation at cyclotron frequency bumped up by the Lorentz factor. The synchrotron spectrum is concentrated at a characteristic frequency,

$$\omega_C = \gamma^3 \omega_{ce} = \gamma^2 \omega_L. \tag{2.14}$$

Synchrotron radiation resembles the aforementioned cyclotron radiation, the difference being the relativistic velocities of gyrating particles. Synchrotron radiation wavelengths are usually in the X-ray bandwidth (Lyne and Graham-Smith, 2012).

2.3.3 *Curvature Radiation*

Due to the presence of a strong magnetic field in the magnetospheres of pulsars, charged particles can be constrained to follow the magnetic field lines very closely with nearly zero pitch angle. As the field lines are generally curved, the electrons are accelerated transversely to their motion and therefore radiate. This type of radiation is known as *curvature radiation* and is closely related to synchrotron radiation.

Assuming an electron with relativistic velocity, constrained to follow the curved field line with curvature radius ρ, the electron radiates similarly to an electron in a circular orbit. As in the case of synchrotron radiation, curvature radiation has a characteristic frequency given by

$$\omega_c = \frac{3c}{4\pi\rho}\gamma^3. \tag{2.15}$$

Coherent curvature emission has been proposed as one of the possible mechanisms for pulsar radio emission. In the case of young pulsars, incoherent curvature emission may extend to gamma-ray wavelengths (Lyne and Graham-Smith, 2012).

2.3.4 *Inverse Compton Scattering*

In an event of a collision between high-energy photons and low-energy electrons, the photons transfer some of their energy to the electrons and therefore emerge with longer wavelengths. This effect is classical *Compton effect*.

In the inverse case, the transfer of energy comes from high-energy electrons (or positrons) to photons. This effect may be regarded as synchrotron radiation of the *charged particles*, as they move in the electromagnetic field of the radiation. Subsequently, the cloud of high-energy particles increases the total radiation energy flux while lowering the wavelengths of the photons. This high-energy mechanism

does not depend on collisions or the presence of a steady magnetic field.

2.3.5 *Maser Amplification*

Radio emission from pulsars, at the time of their discovery, was observed at very high brightness temperatures. Looking for an explanation, Ginzburg and Zheleznyakov (1970) suggested that the radiation comes from some form of instability-driven maser amplification that might occur outside the actual source of radiation. Sometimes regarded as a mechanism effectively based on negative absorption, the maser mechanism relies on amplifying certain plasma wave modes that can escape the plasma in the form of electromagnetic waves. The electron-cyclotron maser will be discussed in greater detail in the next chapter.

3

ELECTRON-CYCLOTRON MASER

The electron-cyclotron maser is a process capable of producing coherent radiation from plasma. Originally proposed as a somewhat exotic concept, it gained a lot of traction during the last 30 years as a dominant mechanism for producing strong emissions in high-temperature magnetized plasmas. Under extreme astrophysical conditions, major energy losses can be attributed to radiation from plasma.

However, to generate the observed radiation strength, the plasma must be in a state where the energy release in the form of radiation is favorable. This is commonly realized at the point when the plasma is no longer able to digest the available free energy, which is transferred from outside and subsequently stored in particle distribution. Given that the plasma is collisionless and the particle density is low, the amount of free energy per particle is large, and direct emission becomes favorable.

The electron-cyclotron maser successfully explains the mechanisms of Auroral kilometric radiation, radio bursts of Jupiter, or solar radio bursts and spikes. In the current state of knowledge, it is also considered a possible candidate for the means of pulsar radio emission. In this chapter, a brief overview of the electron-cyclotron maser theory is presented, as well as a showcase of recent works done by others. As the discussion about the theory of electron-cyclotron maser and its prevalence is still ongoing, many contributions have been done, some of which contradict each other. In this thesis, the content of the reviews done by Treumann (2006) and Zheleznyakov et al. (2016) is mainly presented.

3.1 CYCLOTRON MASER THEORY

The generation of radiation across nearly all wavelengths is commonly thought of as well understood. This holds for most of the optical emission and absorption processes. The theory behind infrared and submillimeter bands, as well as the generation of X-ray and gamma-ray emission, is more complicated, but also quite well described.

The situation at radio wavelengths is, however, much more complex. Although cyclotron and synchrotron emission (mentioned in Section 2.3) provide good results in mapping the large-scale structures, these proved to be true only for the case of long temporal scales.

The situation became even more obscure when high-resolution techniques became available, which showed that the radio emission oc-

curred in narrow bands, varied with time, and its peak power levels reached up to several percent of the available kinetic plasma energy.

The values of observed brightness temperatures were so high that only a coherent emission mechanism could be responsible for the generation of such radiation. The mechanism was ultimately identified as direct linear amplification of the electromagnetic modes by energetic electrons present in the plasma.

The generation of intense radiation is one of the many ways for the plasma to get rid of excess energy. This usually happens when other means of dissipating the free electron energy, such as heating or particle acceleration, become slow. This condition is fulfilled when the non-thermal component of particle distribution dominates in a dilute plasma or a strong magnetic field. However, only the most extreme conditions would transform all free energy into radiation. Therefore, efficiencies of only up to several percent are already very high, with the remaining ∼90% excess energy being dissipated in other ways.

3.1.1 *Basic Properties*

The concept of an electron cyclotron maser that emits radiation at frequencies near the electron cyclotron frequency and its harmonics was first investigated almost simultaneously by Twiss (1958) and Schneider (1959). The authors explored the possibility of direct amplification of the high-frequency electromagnetic waves in plasma. It was realized that this amplification could occur due to a resonant interaction between the wave and energetic electrons, the resonance condition being

$$\omega - k_{\parallel} v_{\parallel} = l \frac{\omega_{ce}}{\gamma}, \tag{3.1}$$

where $k_{\parallel}$ is the wavenumber of parallel wave propagation with respect to the magnetic field, $v_{\parallel}$ is the parallel component of the particle velocity, ω_{ce} is the electron cyclotron frequency and l is the cyclotron harmonic number.

In the magneto-ionic plasma (cold plasma) limit, the solutions of dispersion relation (see Figure 3.1) are the 'fast' RX and LO modes, which propagate above their respective cutoff frequencies and plasma frequency, and the 'slow' RZ. The Z-mode cannot leave the plasma, as it is confined below the upper hybrid frequency, defined as (Budden, 1988)

Commonly written simply as Z-mode.

$$\omega_{uh} \equiv \sqrt{\omega_{pe}^2 + \omega_{ce}^2} < \omega_X. \tag{3.2}$$

Even in the case of very weakly relativistic plasmas, the inclusion of the Lorentz factor γ is important. It was realized by Wu and Lee (1979) that the relativistic correction has a decisive effect on the efficiency of amplification of the emitted wave.

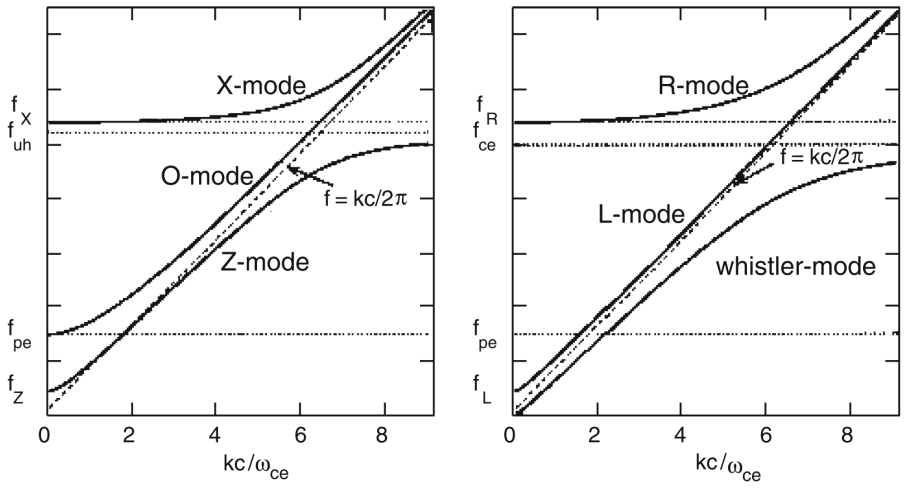

Figure 3.1: The dispersion relations of the magneto-ionic wave modes in plasma for: perpendicular wave propagation (left); parallel wave propagation (right) with respect to the surrounding magnetic field. In the perpendicular case, the X-mode is the 'fast' branch of the wave, the Z-mode is the 'slow' branch of the wave. The X-mode propagates only above the marked cutoff frequency f_X, analogically Z-mode propagates only above f_Z and below the upper hybrid frequency f_{uh}. The O-mode propagates above the plasma frequency f_{pe}. For parallel propagation, the X-mode becomes the R-mode, the O-mode analogically L-mode, and the Z-mode becomes the whistler-mode confined below the electron cyclotron frequency f_{ce} (Treumann, 2006).

3.1.2 *Physics of Electron-Cyclotron Maser*

To generate radiation, the electron-cyclotron maser requires instability in the particle velocity distribution function f. This condition can be expressed by having a positive gradient with respect to perpendicular velocity, $\partial f/\partial v_\perp > 0$. This is realized by having a high-energy component in the distribution, caused by the presence of a strong magnetic field. Interpreting the electron-cyclotron maser as a simple fluid-like plasma instability that is pumping a free-space electromagnetic mode (Chu and Hirshfield, 1978, Winglee, 1983), one can solve the linearized relativistic Vlasov equation for the distribution function f

$$\partial_t f_1 + \mathbf{v}\cdot\nabla f_1 - e\mathbf{v}\times\mathbf{B}_0\cdot\partial\mathbf{p} f_1 = e(\mathbf{E}+\mathbf{v}\times\mathbf{B})\cdot\partial\mathbf{p} f_0, \tag{3.3}$$

where f_0 and f_1 are the constant, respectively perturbed by the presence of the magnetic field, velocity distribution functions, and $\mathbf{p}$ stands for the relativistic momentum $\mathbf{p} = \gamma\mathbf{v}$. However, by taking the undisturbed distribution as that of the cold relativistic plasma and applying known methods (Chu and Hirshfield, 1978) to solve equation (3.3)

and Maxwell equations for plane waves of frequency ω and wave number $\mathbf{k}$, one obtains the dispersion relation

$$\omega^2 - k_\parallel^2 c^2 = \frac{\omega_{pe}^2}{\gamma}\left[\frac{\omega}{\omega - \omega_{ce}/\gamma} + \frac{k_\perp^2 v_\perp^2 (1 - \omega^2/k_\perp^2 c^2)}{2(\omega - \omega_{ce}/\gamma)^2}\right]. \tag{3.4}$$

The solution for real $\mathbf{k}$ and complex $\omega = \omega_r + i\Gamma$ (Γ being the instability growth rate) is shown in Figure 3.2.

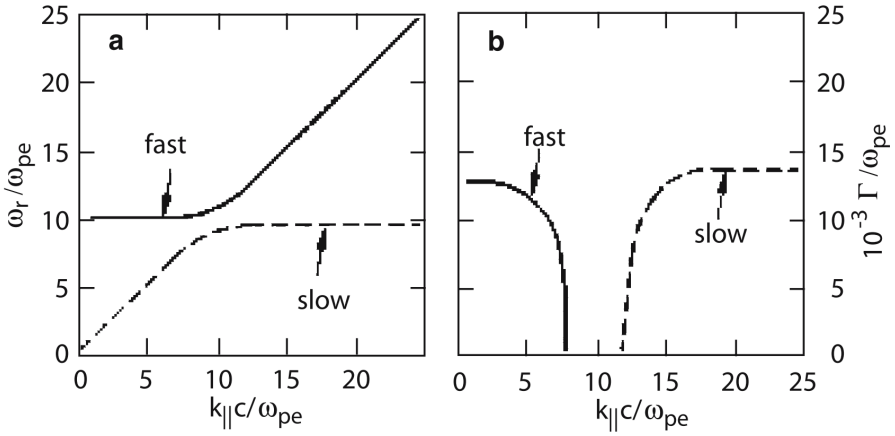

Figure 3.2: Dispersion relations $\omega_r(k_\parallel)$ of the electromagnetic 'fast' and 'slow' wave modes in a plasma and their growth rates $\Omega(k_\perp)$. The unstable 'fast' mode branch is amplified at a frequency close to the electron-cyclotron frequency. The 'slow' is amplified at a slightly lower frequency (Chu and Hirshfield, 1978).

3.2 DOUBLE PLASMA RESONANCE

The double plasma resonance effect (DPR) is the phenomenon of a sharp increase of instability of plasma waves in a magnetized plasma under the condition that the upper hybrid frequency coincides with the harmonics of cyclotron frequency, i.e., the plasma frequency, which is higher than the cyclotron frequency. The radiation mechanism attributed to this effect provides an explanation for the observed so-called *zebra patterns* in the radio spectra of the Sun, Jupiter, and, importantly for our case, the Crab pulsar. Intensive studies of instabilities of plasma waves at DPR frequencies began in the middle of the 1970s, notably after the discovery of zebra pattern in the dynamic solar radio spectra (Elgarøy, 1961). Regarding the zebra patterns in pulsar observations, they were first observed by Hankins and Eilek (2007). This was unexpected at the time, significantly changing how the pulsar magnetospheres were perceived. The evident analogy between the zebra patterns in the solar radio emission and the ones seen in the microwave radiation of the Crab pulsar, which could be interpreted via the DPR effect, suggests that the pulsar magnetospheric

plasma could contain local non-relativistic regions (with lower temperature and weaker magnetic field).

Throughout the last 40 years, Zheleznyakov, among many others, made good progress in the theory of masers driven by the DPR effect. As the theory is not concluded, to avoid ambiguity, subsequent sections mainly draw from his and his collaborators' work (see Zheleznyakov et al., 2016).

3.2.1 *Introduction to the DPR Effect*

As stated above, the coincidence of the hybrid, upper or lower, frequency and a harmonic of cyclotron frequency is known as the double plasma resonance. The DPR affects the plasma in a way that the plasma waves are enhanced at the DPR frequencies in nonequilibrium plasma. Conversion of plasma waves into electromagnetic waves then leads to strong emission of radiation.

According to theoretical works done by Pearlstein et al. (1966) and Zheleznyakov and Zlotnik (1975a,b,c), the instability of plasma consisting of particles with velocity component perpendicular to a magnetic field steeply increases at the upper hybrid resonance frequency ω_{uh}, defined in equation (3.2), given this frequency is close to harmonics of the electron cyclotron frequency, with s being the harmonic number,

$$\omega_{uh} \approx s\omega_{ce}. \tag{3.5}$$

This condition can only be satisfied for many harmonics in a weak magnetic field where the cyclotron frequency is much lower than the one of plasma

$$\omega_{ce} \ll \omega_{pe}. \tag{3.6}$$

Because of this, the resonance condition reduces to the approximate equality.

$$\omega_{pe} \approx s\omega_{ce}. \tag{3.7}$$

The plasma is composed of electrons with a non-equilibrium velocity distribution. The dispersion properties of the system are therefore determined by its background and hot component, while the instability is primarily governed by the energetic hot electrons/positrons. The wave amplification at the DPR levels is due to an almost perpendicular propagation of plasma waves to the magnetic field. This is because, at frequencies close to the electron cyclotron frequency (and its harmonics), the waves that propagate at small angles to the magnetic field are subjected to a strong collisionless decay in the background component of the plasma (see Mikhailovsky, 1974). As a result, the waves at frequencies close to the cyclotron harmonics excited by hot

energetic electrons are limited to exist only at a narrow angle near $\pi/2$ between the magnetic field and the direction of wave propagation (discussed in Zheleznyakov et al., 2016).

For the electron-cyclotron maser with the DPR effect, a distribution function is considered in the form of

$$f(v_\parallel, v_\perp) \propto v_\perp^2 \exp\left(-\frac{v_\parallel^2 + v_\perp^2}{2v_e^2}\right). \tag{3.8}$$

Often referred to as DGH distribution.

This particle velocity distribution function, introduced by Dory et al. (1965), describes the expected properties of particles trapped by the magnetic field, characterized by a deficit of particles with slow velocities and particles with a zero mean velocity along the magnetic field. The maximum particle velocity in the distribution is at the velocity v_e.

3.2.2 *Coalescence of Plasma Waves*

Landau damping is an effect that causes the plasma to exponentially weaken the longitudinal plasma waves, preventing the formation of instability (see Mikhailovsky, 1974).

Upper hybrid and Bernstein waves, which are excited in a source with sufficient density, cannot leave the plasma either because of strong Landau damping, due to the dependence of longitudinal waves on the plasma, or because of their low group velocities, which makes them very slow to propagate. This points toward the fact that the radiation mechanism must necessarily include a transformation of the longitudinal plasma waves into electromagnetic waves, which can freely escape the plasma. The transformation mechanism is described, for example, in Tsytovich (1967). In the case of astrophysical plasmas, the most effective are the processes of either nonlinear convergence of longitudinal waves, their scattering on plasma particles, or coalescence of high-frequency with low-frequency waves, written as

$$\begin{aligned} &\omega_{hf} + \omega_{hf} \approx 2\omega_{hf}; \\ &\omega_{hf} + \omega_{lf} \approx \omega_{hf}. \end{aligned} \tag{3.9}$$

The coalescence occurs between two longitudinal waves, resulting in a transverse wave. The coalescence of a plasma wave with a low-frequency wave gives rise to electromagnetic radiation with a frequency slightly different from the plasma frequency, while the coalescence of two plasma waves generates radiation at double the plasma frequency.

In magnetoactive plasma, the transformation of longitudinal waves leads to the creation of two normal transversal waves, ordinary and extraordinary. The spectral intensity of the electromagnetic radiation due to coalescence of two plasma waves, with respective frequencies

ω_1 and ω_2, wave numbers k_1 and k_2, and spectral energy densities W_{k_1} and W_{k_2}, can be written as (Tsytovich, 1967)

$$I_\omega = (4\pi)^4 \frac{\omega_{pe}^3}{c^3} \frac{L}{n_{o,e}|\partial(\omega^2 n_{o,e}^2)/\partial\omega|} \times \int |S|^2 W_{k_1} W_{k_2} \delta(\omega - \omega_1 - \omega_2)\delta(k - k_1 - k_2) dk_1 dk_2. \tag{3.10}$$

Here, L denotes the source size along the line of sight, $|S|$ is the contraction of the nonlinear conductivity tensor, which acts as an probability amplitude for the coalescence, and $n_{o,e}$ are the refractive indices for ordinary and extraordinary wave modes. Calculations of the probability of the coalescence process and the intensity of the electromagnetic radiation generated for small ratios of ω_{ce}/ω_{pe} are well described in the literature, e.g. Melrose et al. (1980).

To summarize the constraints of the DPR effect, the following conditions are necessary for the DPR effect to occur at different cyclotron harmonics in the radio emission source (discussed in Zheleznyakov et al., 2016):

A. the source must be described with a distribution function consisting of an equilibrium non-relativistic component and a highly energetic component with non-equilibrium velocity components normal to the magnetic field;

B. the magnetic field strength must be low enough to ensure that the plasma is weakly anisotropic and the cyclotron harmonics are within the observed frequency bandwidth;

C. the velocity of high-energy electrons must be significantly higher than the velocity of the background plasma electrons, although still below the relativistic limit.

3.2.3 *Fine Structure of the Radiation Spectrum*

The zebra pattern in Crab pulsar radio emission was observed using the 300 m radio telescope Arecibo (Figure 1.3) using a dynamic spectrograph with a very high time resolution (Hankins and Eilek, 2007; Hankins and Rankin, 2010). The discovery of the fine structure of the dynamic spectrum (see Figure 3.3), in the form of narrow quasi-harmonic stripes drifting parallel in time, provided a new perspective on the problem and significantly constrained the possible radio emission mechanisms.

The observed dynamic spectra of short bursts in the interpulse of the microwave radio emission from the Crab pulsar are in many regards reminiscent of the zebra pattern found in the solar radio emission:

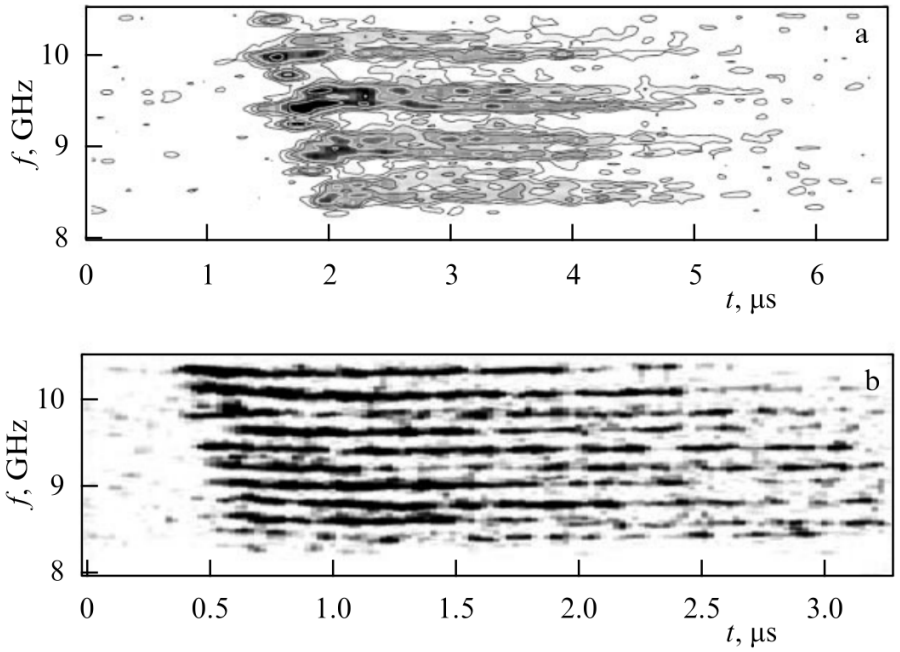

Figure 3.3: Examples of observed dynamic spectra of Crab pulsar with zebra pattern obtained with the 300 m radio telescope Arecibo. (a) Hankins and Eilek (2007); (b) Hankins and Rankin (2010).

A. both structures represent a set of quasi-harmonic enhanced emission stripes with a stripe spacing much smaller than the emission frequency;

B. the stripe spacing is not constant, the spacing increases with frequency (Hankins and Eilek, 2007; Zlotnik et al., 2003).

In the case of solar radio emission, the zebra patterns are observed in the wavelength range from several centimeters to several meters, most frequently recorded in the decimeter range. The zebra patterns from the Crab pulsar were detected in the microwave range. The upper frequency limit for pulsar observations might be receiver-related, so there is a possibility that the zebra pattern spectrum extends to higher frequencies.

The proposed mechanisms of emission with a zebra pattern emerged immediately after the discovery of the fine structure. For example, Lyutikov (2007) proposed that the observed structure is related to the instability of relativistic electrons due to the anomalous Doppler effect under the condition

$$\omega - k_{\parallel} v_{\parallel} = \frac{s\omega_{ce}}{\gamma}, \qquad s < 0. \tag{3.11}$$

Assuming that the source is located near the light cylinder, where the magnetic field strength is $B \sim 10^6$ G, for the radiation to be in the microwave range, the Lorentz factor of the emitting particles must be $\gamma \approx 7 \cdot 10^7$ and the plasma number density in the emitting region

about $3 \cdot 10^5$ times larger than the Goldreich–Julian density (2.8). Furthermore, ultrarelativistic electrons can hardly generate radio emission with the detailed structure of a zebra pattern.

In the work done by Karlický (2013), the zebra pattern in the Crab Pulsar radio emission is explained by the modulation of the plasma wave amplification coefficient. However, this model is unable to explain the observed polarization of the ordinary waves. The polarization was investigated in greater detail by Zlotnik et al. (2014), who argued that the polarization can be determined by different transformation efficiencies of plasma waves as well as by different propagation and escape conditions of ordinary and extraordinary waves.

The geometry of the radio emission source, which could generate the observed quasiharmonic emission bands with fine structure, was addressed by Zheleznyakov and Shaposhnikov (2020). To explain the fine structure of the emission, they considered a planar configuration of the magnetic field and plasma density in the current sheet. The radiation is generated in local formations, where the DPR condition (3.7) is fulfilled. The structure of the radiation spectrum is determined by the nature of inhomogeneity of the plasma and magnetic field in the current sheet.

3.3 RECENT THEORETICAL WORKS

To put the idea of the thesis into a broader context, a summary of recent journal papers is presented. Although these works are mainly aimed at providing an explanation of the solar phenomena instead of those of pulsars, they are done using a similar theoretical framework and computational methods, thus providing important constraints and relatively comparable results.

3.3.1 *Benáček and Karlický (2018)*

Benáček and Karlický (2018) in *Double plasma resonance instability as a source of solar zebra emission* investigated the instability created by the DPR effect from a numerical point of view. The authors used 3D Particle-In-Cell code TRISTAN (see Chapter 5). The simulations were conducted in two distinct regimes: (a) *multi-mode* model that is spatially extended, but computationally more demanding; (b) *specific-mode* model, which only spatially accommodates only a few wavelengths of plasma waves; however, it is less demanding and allows one to survey a broader range of possible configurations while consuming less resources. For the hot electron component of the plasma, the authors used a DGH distribution in the form of

$$f = \frac{v_\perp^2}{2(2\pi)^{3/2} v_{\mathrm{th}}^5} \exp\left(- \frac{v_\perp^2 + v_\parallel^2}{2 v_{\mathrm{th}}^2} \right), \tag{3.12}$$

while the background electron plasma component was considered to be Maxwellian.

They found that during the simulation the hot electron distribution changes (Figure 3.4). Moreover, it was shown that the instability growth rate, as well as the saturation energy, are proportional to the hot electron number density, and the contrast between the maximum and minimum of the growth rate diminishes by increasing the hot electron temperature.

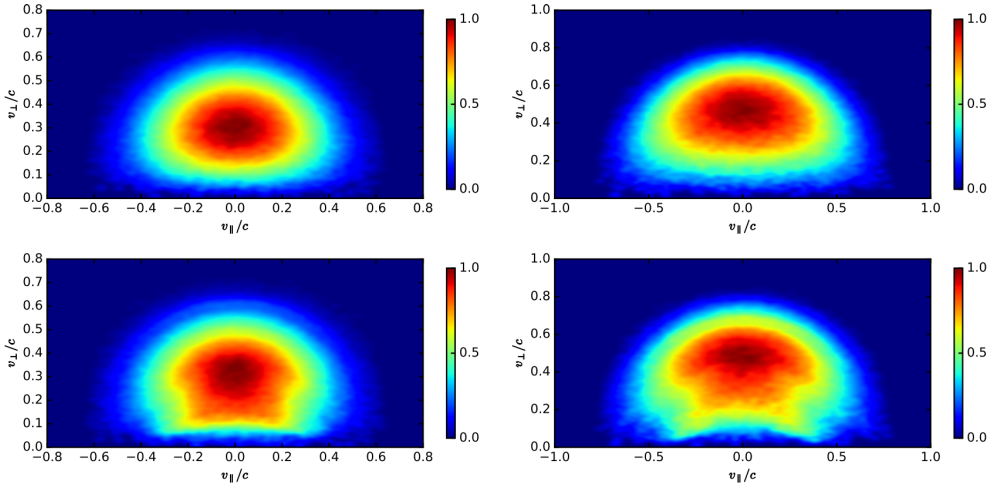

Figure 3.4: Changes of the hot electron distribution functions during the DPR instability at the start (top row) and at time $\omega_{pe}t = 1000$ (bottom row). *Left column*: simulation with $v_{th} = 0.2$, $v_{tb} = 0.03$, and $s = 6$. *Right column*: simulation with $v_{th} = 0.3$, $v_{tb} = 0.03$, and $s = 5$ (Benáček and Karlický, 2018).

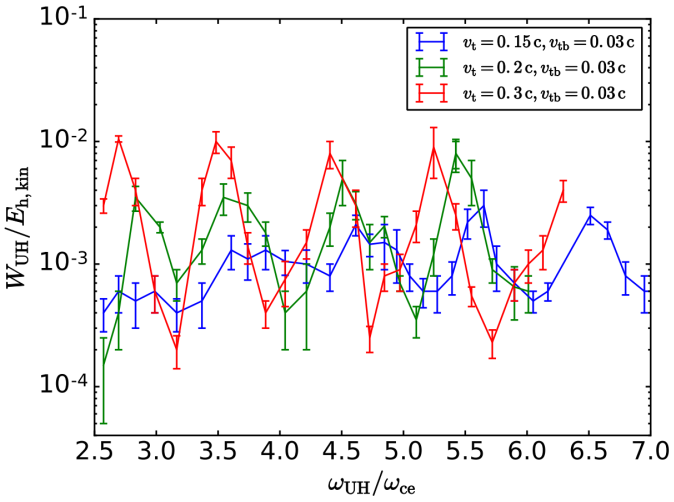

Figure 3.5: Saturation energy of the instability as a function of ω_{uh}/ω_{ce} for different hot electron temperatures (Benáček and Karlický, 2018).

3.3.2 *Li et al. (2021)*

Li et al. (2021) in *PIC Simulation of Double Plasma Resonance and Zebra Pattern of Solar Radio Bursts* investigated the DPR effect based on electron cyclotron maser instability-driven emission mechanism. They carried out multiple simulations with varying values of ω_{pe}/ω_{ce} using the Particle-In-Cell method. In their study, as in Benáček and Karlický (2018), they assumed that the plasma distribution consists of a background Maxwellian component and a hot electron component described by the DGH distribution (3.12). They found that both the electrostatic UH wave and electromagnetic Z and whistler modes are excited through the maser instability, consistent with the DPR effect theory. Furthermore, the authors found that the energy of energetic electrons is important for the characteristics of the UH mode and the radiation pattern of the harmonic emission since for larger electron velocities (0.3 and 0.4c) the UH mode distributes more diffusively.

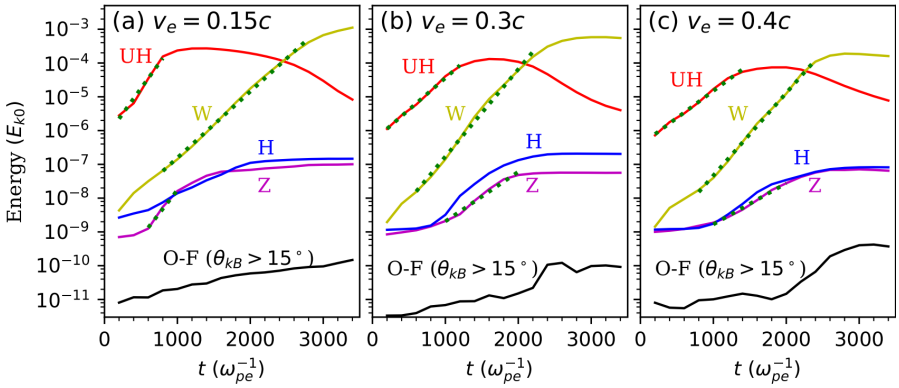

Figure 3.6: Temporal energy profiles of the upper hybrid (UH), Z, and whistler (W) modes with $\omega_{pe}/\omega_{ce} = 10$ for various values of the hot electron velocity. The energy values are normalized to respective initial kinetic energy of total electrons. The three dotted lines represent exponential fittings to energy profiles (Li et al., 2021).

3.3.3 *Ning et al. (2021)*

Ning et al. (2021) in *Harmonic Maser Emissions from Electrons with Loss-cone Distribution in Solar Active Regions* conducted simulations of solar active regions under conditions required for electron cyclotron maser emission. They used a fully kinetic Particle-In-Cell code to investigate the wave excitations and subsequent nonlinear processes induced by the energetic component. Analogically to works listed above, the authors used a Maxwellian velocity distribution function for the background electron plasma component, however, instead of DGH dis-

tribution, a double-sided loss-cone distribution (see Figure 3.7) was used in the form

$$f(v,\mu) = AG(\mu)\exp\left(-\frac{v^2}{2v_{\text{th}}^2}\right),$$
$$G(\mu) = 1 - \tanh\frac{|\mu| - \mu_0}{\delta}, \tag{3.13}$$

where A denotes the normalization coefficient, $\mu = v_{\parallel}/v$ is the cosine of the pitch angle, and $\delta = 0.1$ determines the smoothness of the loss-cone boundary. The loss-cone angle was set to 30°. The density ratio of hot electrons to total electrons was $1/10$.

The authors found that at $\omega_{\text{pe}}/\omega_{\text{ce}} = 0.25$ the first harmonic X-mode (X1) and Z-mode waves are amplified via the electron cyclotron maser instability. Moreover, they obtained strong emissions at the second-harmonic X-mode (X2). They believe that while the X1 and Z-modes are amplified directly via the maser instability, the X2 emissions could be produced by nonlinear coalescence between two Z-modes or Z and X1-modes.

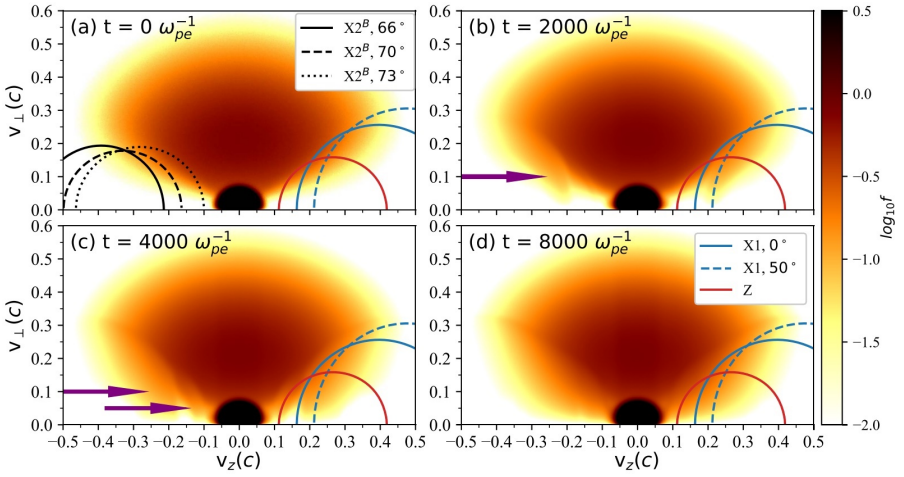

Figure 3.7: Visualization of hot electrons distribution function at times $t = 0$, 2000, 4000, and 8000 ω_{pe}^{-1}. The purple arrows point to the areas of electron diffusion. The curves in blue, red, and black represent the resonance curves corresponding to the amplified waves in X1, Z, and X2 modes (Ning et al., 2021).

Part II

NUMERICAL MODEL

As the neutron stars are only tens of kilometers wide, they are immensely difficult to observe. That is why a different approach was chosen in order to describe the phenomena, and that is trying to replicate the behavior of the studied environment using high-performance numerical simulations.

4

PARTICLE-IN-CELL FUNDAMENTALS

4.1 INTRODUCTION TO PLASMA SIMULATIONS

There are several approaches to accurately simulate the behavior of a plasma system. Some of the popular methods are *magnetohydrodynamic* simulations, commonly written as MHD models, and *Particle-In-Cell* simulations (PIC). MHD models, as their name suggests, consider the plasma to be a conductive fluid that can be described using statistical properties. On the other hand, the PIC approach describes the plasma on a kinetic level, using particles that are interacting with electric and magnetic fields. Worth mentioning are also hybrid codes that combine MHD and PIC codes (e.g. using the fluid description for electrons and kinetic for ions) or Fokker-Planck codes, that consider collisions between particles.

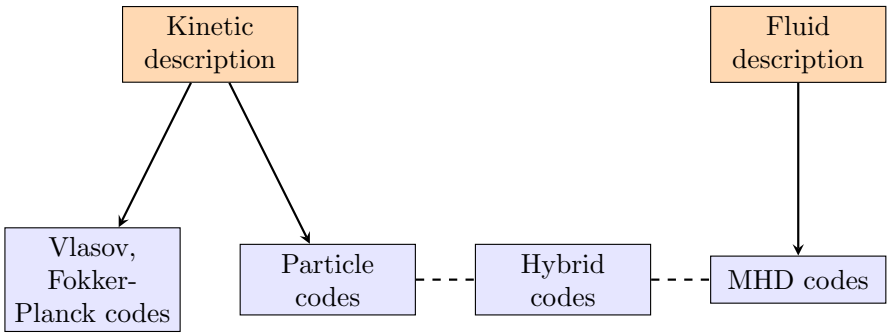

Figure 4.1: Different approaches to plasma simulations (Benáček, 2019).

4.2 FUNDAMENTAL EQUATIONS

Starting point of a plasma simulation is a velocity distribution function that is the solution of the Boltzmann equation

$$\frac{\partial f(\mathbf{r},\mathbf{v},t)}{\partial t} + \mathbf{v}\cdot\frac{\partial f(\mathbf{r},\mathbf{v},t)}{\partial \mathbf{r}} + \frac{\mathbf{F}}{m}\cdot\frac{\partial f(\mathbf{r},\mathbf{v},t)}{\partial \mathbf{v}} = \left(\frac{\partial f(\mathbf{r},\mathbf{v},t)}{\partial t}\right)_{\text{coll}}. \quad (4.1)$$

In many astrophysical applications, it is assumed that the plasma is collisionless, therefore the right hand term reduces to zero, becoming the so-called Vlasov equation

$$\frac{\partial f(\mathbf{r},\mathbf{v},t)}{\partial t} + \mathbf{v}\cdot\frac{\partial f(\mathbf{r},\mathbf{v},t)}{\partial \mathbf{r}} + \frac{\mathbf{F}}{m}\cdot\frac{\partial f(\mathbf{r},\mathbf{v},t)}{\partial \mathbf{v}} = 0. \quad (4.2)$$

As the method is applied to the simulation of plasma, a basic understanding of plasma physics is recommended. A good starting point might be the author's previous thesis (Labaj, 2020), which includes references to suitable literature.

The fields are computed from the Maxwell equations

$$\nabla \times \mathbf{E} = -\frac{\partial \mathbf{B}}{\partial t}, \qquad \nabla \cdot \mathbf{E} = \frac{\rho_e}{\epsilon_0}, \tag{4.3}$$
$$\nabla \times \mathbf{B} = \mu_0 \left(\mathbf{j} + \epsilon_0 \frac{\partial \mathbf{E}}{\partial t} \right), \qquad \nabla \cdot \mathbf{B} = 0.$$

Velocities of the particles at time $t = 0$ are given by the velocity distribution function f. During the time of the simulation, the particle motion is solved using the Lorentz-Newton system of equations

$$\frac{d\mathbf{p}}{dt} = q\left(\mathbf{E} + \frac{\mathbf{v} \times \mathbf{B}}{c} \right), \qquad \frac{d\mathbf{r}}{dt} = \mathbf{v}. \tag{4.4}$$

With the use of the above-mentioned equations, the system is self-consistent with no contradictions or anomalies.

4.3 PARTICLE-IN-CELL PRINCIPLES

The origins of PIC date back to the 1950s (Dawson, 1983). The backbone of the PIC method is essentially numerically solving the partial differential equations in the simplest way possible. However, even by making the set of equations as simple as possible, solving the interactions between all of the particles is computationally impossible. PIC overcomes this with the introduction of *grid*. Particles do not feel the fields of each other. Instead, they contribute to the field of the *grid cell* and through them, the fields are interpolated on particle motion.

This applies to the case of collisionless plasma.

Over the years, many key ideas and computational concepts were introduced and implemented into the codes, making them faster and much more optimized than ever before.

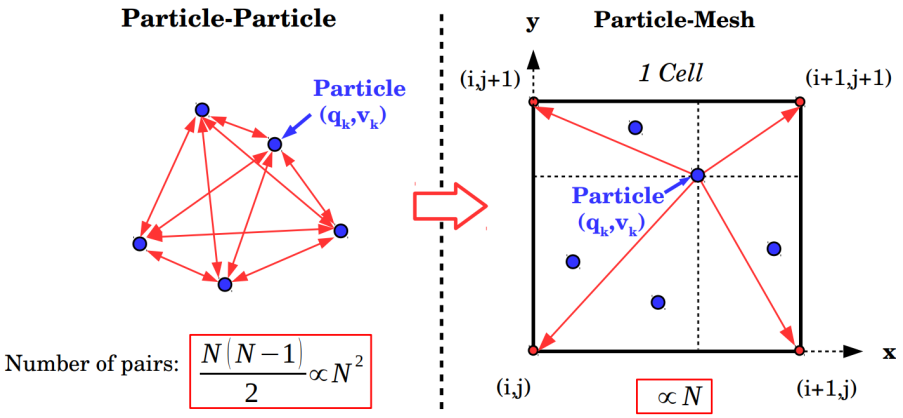

Figure 4.2: The philosophy of PIC method. Instead of interacting with each other, the particles contribute to the field of grid. The relation between number of particles N and total interactions is thus reduced from $\propto N^2$ to $\propto N$ (Cerutti, 2015).

4.3.1 *Superparticles*

Typical particle density of plasma in pulsar magnetosphere can be $\approx 10^{11}\mathrm{cm}^{-3}$ (Zheleznyakov et al., 2016). It is not possible to take every single particle and its impact on the electric/magnetic field into account. A cloud of particles can be approximated as a *superparticle*. The choice is made to represent a particle group that is condensed near each other. Mathematically, the distribution function of each species is given by the superposition of these superparticles:

Sometimes referred to as macroparticles.

$$f_s(\mathbf{r}, \mathbf{v}, t) = \sum_p f_p(\mathbf{r}, \mathbf{v}, t) \tag{4.5}$$

4.3.2 *Particle Mover and Field Solver*

Both field (4.3) and particle (4.4) equations are solved using the so-called *Leap-frog integration*. The method is based on staggering the time levels of the velocity/position in motion equations and electric/-magnetic field in the field equations by half a time step. The physical properties are then computed using the finite difference method. In the case of TRISTAN, the particles are solved using the *Boris push* (Boris, 1970), the fields using the *Yee algorithm* (Yee, 1966). Usually, the used algorithms are referred to as *particle mover* and *field solver*.

Illustratively for the field update, given the electric field $\mathbf{E}$ with cell indices (i', j', k') and the magnetic field $\mathbf{B}(i, j, k)$, $\mathbf{E}$ in the position of $\mathbf{B}$ is given by interpolation of the adjacent cells

$$\begin{aligned} e_x(i,j,k) &= \frac{e_x(i'-1,j',k') + e_x(i',j',k')}{2}, \\ e_y(i,j,k) &= \frac{e_y(i',j'-1,k') + e_y(i',j',k')}{2}, \\ e_z(i,j,k) &= \frac{e_z(i',j',k'-1) + e_z(i',j',k')}{2}. \end{aligned} \tag{4.6}$$

The same process can be applied in the case of $\mathbf{B}$. The particle mover and field solver will be further discussed in the TRISTAN chapter. The schemes are stable for oscillatory motion - if the calculation would be set to compute both variables at the same time step, the simulation would inevitably crash due to a violation of energy conservation.

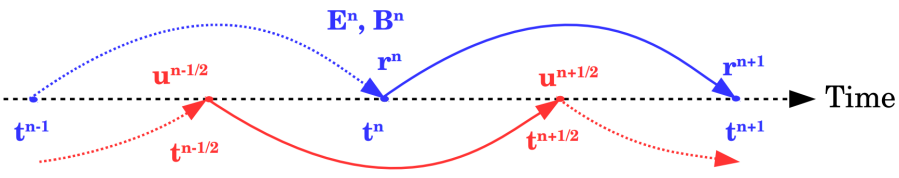

Figure 4.3: Boris push. The velocity and position are staggered in time by half a time step (Cerutti, 2015).

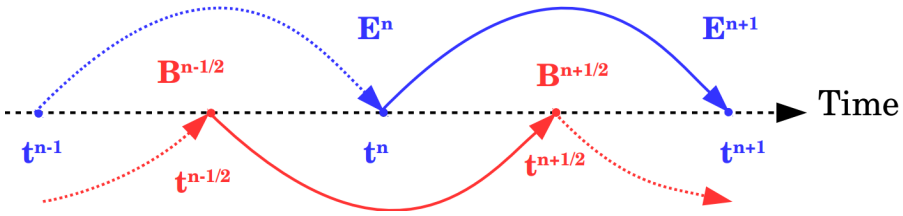

Figure 4.4: Yee Algorithm. The fields are staggered in both space and time (figure illustrates only time) (Cerutti, 2015).

4.3.3 *Particle and Field Weighting*

The name *Particle-In-Cell* originates from the fact that particles can be situated anywhere on the computational domain, but macroscopical quantities such as current or charge density are calculated on the mesh points (just like fields). To obtain the macro-quantities, it is assumed that the particles have a *shape* that is determined by the shape function

$$S(x - X), \tag{4.7}$$

where x is the particle coordinate and X the observation point. Increasing the order of shape function directly increases the accuracy, but also requires more computing power.

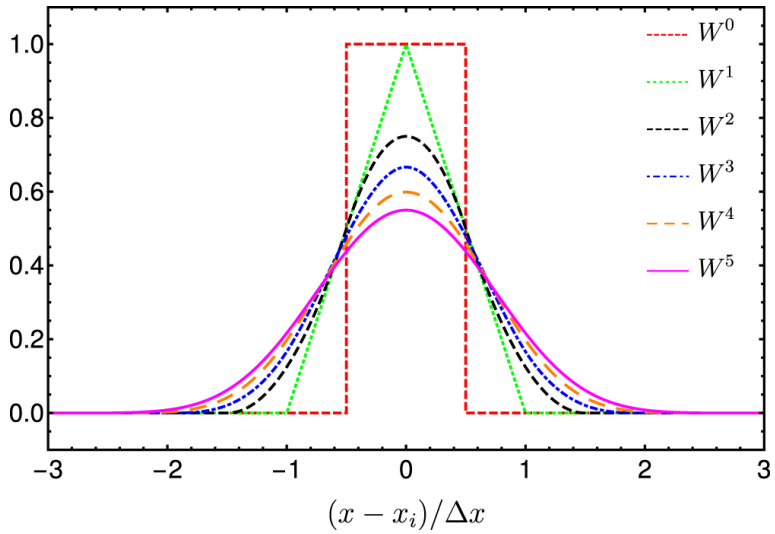

Figure 4.5: Examples of possible shape functions. Higher order schemes require more computational resources, but yield more accurate results (Shalaby et al., 2017).

4.3.4 *Stability Conditions*

PIC simulations are subject to certain conditions of stability. In an event of their exceeding, the energy of the simulation is no longer conserved, rendering any results meaningless.

- *Stability of particle motion*: $\Delta t < 2\omega_{pe}^{-1}$;
  This is derived from the oscillations of one-dimensional plasma (Tskhakaya et al., 2007). If exceeded, the numerical frequency starts to grow exponentially with no physical counterpart, making the solution unstable with the particles heating very quickly. These conditions apply to the Boris push.

- *Stability of the field equations*: $c\Delta t < \Delta x$;
  The condition is commonly known as the *CFL condition*, named after their authors (Courant et al., 1928). The condition states that the time step cannot exceed the time required for the signal to travel through a single cell. The characteristic speed of the signal is the speed of light c. In the case of a 3D system with cell dimensions $\Delta x = \Delta y = \Delta z$, the condition is modified to $c\Delta t < \Delta x/\sqrt{3}$.

These are not the only conditions required for stable computation. For more detail, one should see Hockney and Eastwood (1988).

5 TRISTAN MODEL

TRISTAN (from **Tri**dimensional **Stan**ford Code) was originally published by Buneman et al. (1993) as a code suited for planet magnetosphere simulations, and later was published in a book by Matsumoto and Omura (1993) for general use. Its strengths are that it is fully electromagnetic, relativistic, and charge conserving. In this thesis, modified TRISTAN code is used, with many improvements and better functionality for the application to astrophysical plasma.

The code is written in Fortran. TRISTAN was parallelized using MPI (*Message Passing Interface*) in particles by Karlický and in field domains by Benáček (2019). Thanks to this, it is suited for large-scale computing using thousands of processor cores. In this chapter, its key components will be discussed in greater detail.

Term parallelization indicates that the simulation can effectively run on multiple processors at the same time.

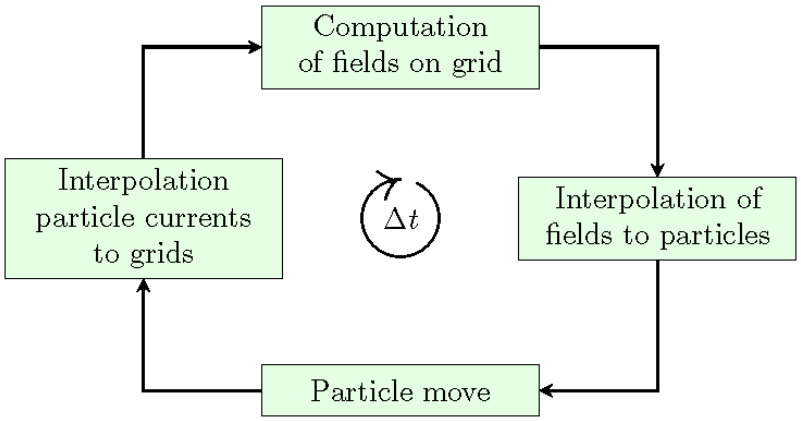

Figure 5.1: Basic computational scheme of a PIC Code (Benáček, 2019).

5.1 MODEL CONFIGURATION

TRISTAN uses model relative scales for the sake of simplifying the calculations. Computational domain is a rectangular grid with cell dimensions being set to $\Delta x = \Delta y = \Delta z = 1$. Time discretization is $\Delta t = 1$. Because of this, the size of the time step directly relates to the choice of plasma frequency ω_{pe}. Usual value of speed of light is $c = 0.5$. This way, the signal can traverse through half a cell atmost in a course of a single time step.

Table 1: Independent physical quantities of TRISTAN model.

Parameter	
speed of light	c
electron mass	m_e
mass ratio	m_i/m_e
thermal velocities	v_{tb}, v_{th}
permittivity	ϵ_0
frequency ratio	ω_{ce}/ω_{pe}
particle density ratio	n_{th}/n_{tb}
time step	$\omega_{pe}\Delta t$

5.2 PARTICLE UPDATE

The time centered, finite difference scheme of the Lorentz-Newton equations (4.4) is

This way, the position $\mathbf{r}$ *is leap-frogged over velocity* $\mathbf{v}$.

$$\mathbf{v}^{new} = \mathbf{v}^{old} + \frac{q\Delta t}{m}\left(\mathbf{E} + \frac{1}{2}(\mathbf{v}^{new} + \mathbf{v}^{old}) \times \mathbf{B}\right) \tag{5.1}$$

$$\mathbf{r}^{next} = \mathbf{r}^{current} + \Delta t \mathbf{v}^{new}. \tag{5.2}$$

For the calculation of particle motion, more complex scheme is used. The three step scheme (Hockney and Eastwood, 1988, Birdsall and Langdon, 1991) of *Boris push* (Boris, 1970) has the following form:

1. The first half of acceleration by electric field

$$\mathbf{v}_0 = \mathbf{v}^{old} + \frac{q\mathbf{E}\Delta t}{2m}, \tag{5.3}$$

2. rotation in magnetic field

$$\mathbf{v}_1 = \mathbf{v}_0 + 2\frac{\mathbf{v}_0 \times \mathbf{v}_0 \times \mathbf{b}_0}{1 + b_0^2} \times \mathbf{b}_0 \tag{5.4}$$

3. and finally the second half of the electric acceleration

$$\mathbf{v}^{new} = \mathbf{v}_1 + \frac{q\mathbf{E}\Delta t}{2m}. \tag{5.5}$$

The fields interacting with the particle are linearly weighted based on their distance from the closest grid point.

5.3 FIELD UPDATE

Speed of light c is set to 0.5, therefore, it can only travel through half of a cell in the course of a single time step Δt. The dielectric constant ϵ_0 is set to 1, so $\mu_0 = 1/c^2 = 4$. The model records **E** components (e_x, e_y, e_z) and $c\mathbf{B}$ components (b_x, b_y, b_z). The magnetic field components are multiplied by c for better computation, maintaining the fundamental symmetry of $e \longleftrightarrow b$ in Maxwell equations (4.3).

The electric and magnetic fields are computed from the Maxwell equations. The calculation of the time change of **B** at grid position (i, j, k) can be written as

$$
\begin{aligned}
b_{\mathrm{x}}^{\mathrm{new}}(i,j,k) &= b_{\mathrm{x}}^{\mathrm{old}}(i,j,k) \\
&\quad + c\Delta t\left[\frac{e_{\mathrm{y}}(i,j,k+1) - e_{\mathrm{y}}(i,j,k)}{\Delta z} - \frac{e_{\mathrm{z}}(i,j+1,k) + e_{\mathrm{z}}(i,j,k)}{\Delta y}\right], \\
b_{\mathrm{y}}^{\mathrm{new}}(i,j,k) &= b_{\mathrm{y}}^{\mathrm{old}}(i,j,k) \\
&\quad + c\Delta t\left[\frac{e_{\mathrm{z}}(i+1,j,k) - e_{\mathrm{z}}(i,j,k)}{\Delta x} - \frac{e_{\mathrm{x}}(i,j,k+1) + e_{\mathrm{x}}(i,j,k)}{\Delta z}\right], \\
b_{\mathrm{z}}^{\mathrm{new}}(i,j,k) &= b_{\mathrm{z}}^{\mathrm{old}}(i,j,k) \\
&\quad + c\Delta t\left[\frac{e_{\mathrm{x}}(i,j+1,k) - e_{\mathrm{x}}(i,j,k)}{\Delta y} - \frac{e_{\mathrm{y}}(i+1,j,k) + e_{\mathrm{y}}(i,j,k)}{\Delta x}\right].
\end{aligned}
$$

For better numerical stability of the code, the magnetic field is advanced in two sub-time steps with $\Delta t = 0.5$. The update of electric field follows the half-advances of magnetic field and analogously can be written as

$$
\begin{aligned}
e_{\mathrm{x}}^{\mathrm{new}}(i,j,k) &= e_{\mathrm{x}}^{\mathrm{old}}(i,j,k) \\
&\quad + c\Delta t\left[\frac{b_{\mathrm{y}}(i,j,k-1) - b_{\mathrm{y}}(i,j,k)}{\Delta z} - \frac{b_{\mathrm{z}}(i,j+-,k) + b_{\mathrm{z}}(i,j,k)}{\Delta y}\right], \\
e_{\mathrm{y}}^{\mathrm{new}}(i,j,k) &= e_{\mathrm{y}}^{\mathrm{old}}(i,j,k) \\
&\quad + c\Delta t\left[\frac{b_{\mathrm{z}}(i-1,j,k) - b_{\mathrm{z}}(i,j,k)}{\Delta x} - \frac{b_{\mathrm{x}}(i,j,k-1) + b_{\mathrm{x}}(i,j,k)}{\Delta z}\right], \\
e_{\mathrm{z}}^{\mathrm{new}}(i,j,k) &= e_{\mathrm{z}}^{\mathrm{old}}(i,j,k) \\
&\quad + c\Delta t\left[\frac{b_{\mathrm{x}}(i,j-1,k) - b_{\mathrm{x}}(i,j,k)}{\Delta y} - \frac{b_{\mathrm{y}}(i-1,j,k) + b_{\mathrm{y}}(i,j,k)}{\Delta x}\right].
\end{aligned}
$$

5.4 CURRENT DECOMPOSITION

TRISTAN, in comparison with other PIC codes, does not employ a charge density array. Instead, direct particle current deposition is used. Because of this, the cohesion between simulated particles is removed and thus parallelization is enabled. TRISTAN conserves charge effectively, using the scheme published by Villasenor and Buneman (1992).

Electric field at the point of the grid (i, j, k), where

$$i = \text{round}(x), \quad j = \text{round}(y), \quad k = \text{round}(z)$$

represent the rounded positional values and

$$\delta x = x - i, \quad \delta y = y - j, \quad \delta z = z - k$$

are the volume weighed distances, is modified by electric current $\mathbf{J} = (\mathrm{j_x}, \mathrm{j_y}, \mathrm{j_z})$. This modification can be written as

$$\begin{aligned}
e_\mathrm{x}(i,j,k) &= e_\mathrm{x}(i,j,k) - j_\mathrm{x} \cdot cy \cdot cz, \\
e_\mathrm{x}(i,j+1,k) &= e_\mathrm{x}(i,j+1,k) - j_\mathrm{x} \cdot \delta y \cdot cz, \\
e_\mathrm{x}(i,j,k+1) &= e_\mathrm{x}(i,j,k+1) - j_\mathrm{x} \cdot cy \cdot \delta z, \\
e_\mathrm{x}(i,j+1,k+1) &= e_\mathrm{x}(i,j+1,k+1) - j_\mathrm{x} \cdot \delta y \cdot \delta z,
\end{aligned}$$

$$\begin{aligned}
e_\mathrm{y}(i,j,k) &= e_\mathrm{y}(i,j,k) - j_\mathrm{y} \cdot cx \cdot cz, \\
e_\mathrm{y}(i,j+1,k) &= e_\mathrm{y}(i,j+1,k) - j_\mathrm{y} \cdot \delta x \cdot cz, \\
e_\mathrm{y}(i,j,k+1) &= e_\mathrm{y}(i,j,k+1) - j_\mathrm{y} \cdot cx \cdot \delta z, \\
e_\mathrm{y}(i,j+1,k+1) &= e_\mathrm{y}(i,j+1,k+1) - j_\mathrm{y} \cdot \delta x \cdot \delta z,
\end{aligned}$$

$$\begin{aligned}
e_\mathrm{z}(i,j,k) &= e_\mathrm{z}(i,j,k) - j_\mathrm{z} \cdot cy \cdot cx, \\
e_\mathrm{z}(i,j+1,k) &= e_\mathrm{z}(i,j+1,k) - j_\mathrm{z} \cdot \delta y \cdot cx, \\
e_\mathrm{z}(i,j,k+1) &= e_\mathrm{z}(i,j,k+1) - j_\mathrm{z} \cdot cy \cdot \delta x, \\
e_\mathrm{z}(i,j+1,k+1) &= e_\mathrm{z}(i,j+1,k+1) - j_\mathrm{z} \cdot \delta y \cdot \delta x,
\end{aligned}$$

where

$$cx = 1 - \delta x, \quad cy = 1 - \delta y, \quad cz = 1 - \delta z.$$

5.5 BOUNDARY CONDITIONS

Certain constraints on simulation boundaries must be applied to successfully simulate the physical environment. These boundary conditions have to be applied to both fields and particles. There are two main categories of boundary conditions: boundaries between subgrids that assure that the neighboring subgrids are effectively sewn in all dimensions, and outer boundaries that are implemented in a way corresponding with the studied situation. Our model uses periodic boundary conditions in y and z axis, and periodic boundary conditions in all axis.

5.6 MODEL WORKFLOW

The model is divided between multiple files (see Table 2). The main part of the model is in `model.f90`. File `savedata.f90` contains the configuration of storage (e.g. what data and how often do you want to save them) and calculation of chosen physical properties, such as kinetic and field energies. The values of constants, the choice of particle density, distribution function, frequency ratios, etc. are declared in `config.f90`. The file `init.f90` includes the properties of the system at $t = 0$: particle number density distributed over the chosen velocity distribution function.

Table 2: File body of TRISTAN model.

filename	**function**
`model.f90`	main body of the model
`config.f90`	simulation parameters
`mover.f90`	particle mover
`current.f90`	current decomposition
`savedata.f90`	storage
`init.f90`	initial conditions
`boundfield.f90`	boundary conditions
`boundptl.f90`	

At the start of the simulation, the MPI parameters for CPU allocation for the fields and particles are loaded. Once allocated, the processors maintain the grid size throughout the simulation process. At first, the density of the particles per processor is constant; however, this changes as the particles start to flow. After the arrays are loaded, the model initializes the MPI interface, which then automatically assigns the grids to processors for computing. The choice is determined in such a way that neighboring subgrids are assigned to processors close to each other. This helps the model in reducing the communication overhead between processors. Then, the physical parameters are loaded. The independent parameters are loaded from the model configuration, and other parameters are computed. Initialization of fields follows, with **E** usually set to 0 and **B** set to reflect the studied phenomena. For data storage , the model uses the high-performance *Hierarchical Data Format* (HDF5), which is internally suited for MPI usage. The computing process is essentially a looped cycle that repeats the calculations until the chosen number of time steps is reached. Each time step consists of computation, MPI communication and data storage. Overview of a simulation cycle is shown on Figure 5.2.

Usually, the data storage takes the longest time and takes a lot of space, therefore data are not stored in every single time step.

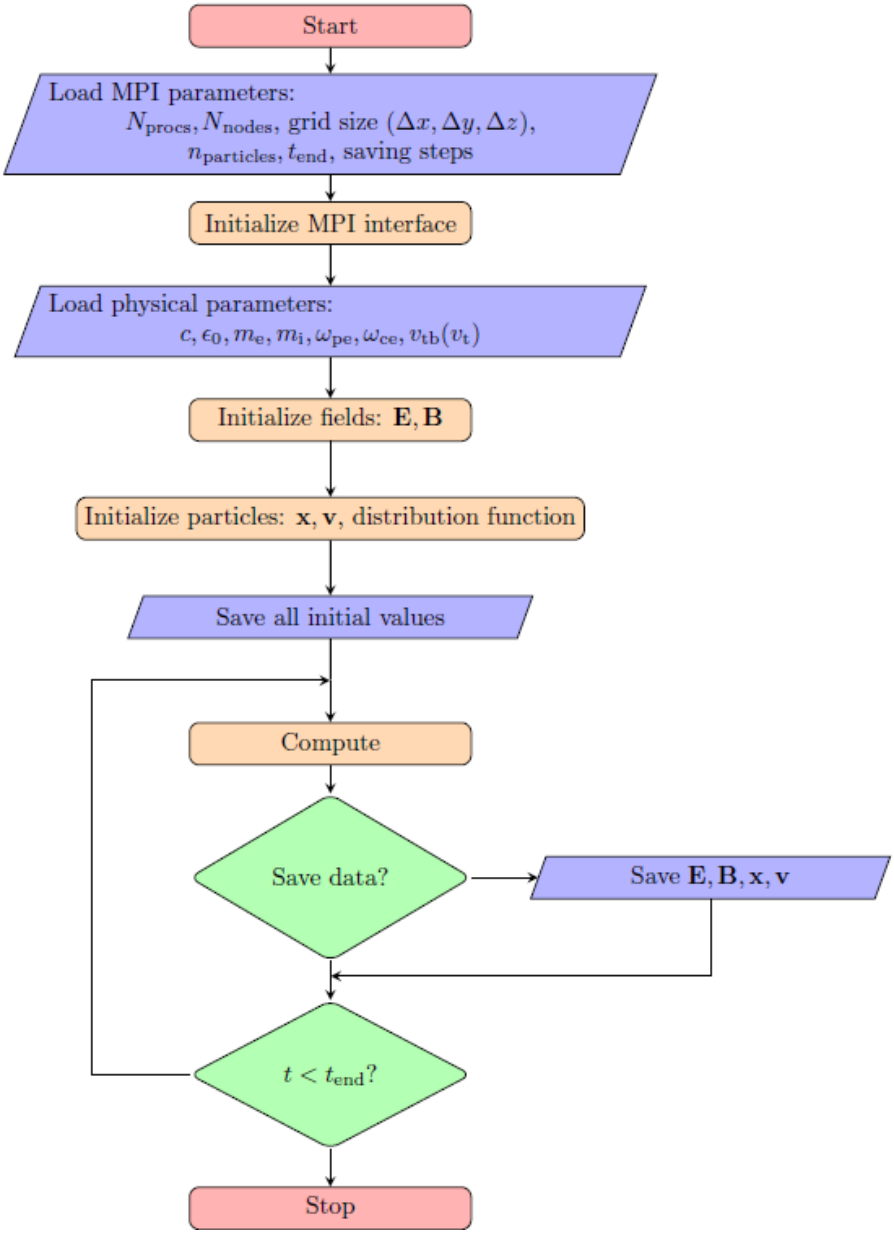

Figure 5.2: Visual overview of a TRISTAN simulation cycle.

Part III

SIMULATIONS & RESULTS

In this part, the results obtained from simulations that were conducted over the past year are presented. Investigated physical effects are subsequently discussed and put into the perspective of the proposed theory.

6 SIMULATIONS

Given the physical motivation stated in this work so far, a series of simulations were conducted to simulate plasma wave amplification driven by the electron–positron cyclotron maser instability. The simulations were carried out in 3 cycles:

A. Optimization of the code through tests of different orders of shape function for the current deposition to find the best ratio between the accuracy of the result and required computing power (see Appendix B);

B. $\sim$ 60 small-scale simulations with various physical and computational configurations to find an ideal setup and grasp the effects of investigated physical quantities;

C. $\sim$ 20 large-scale simulations for detailed dispersion analysis of formed plasma waves.

The modified TRISTAN code (see Chapter 5) was used in all simulations. The analysis of the results was performed using the NumPy and SciPy Python libraries. For the optimization of the code, computational resources were provided by the Department of Theoretical Physics and Astrophysics, Masaryk University, with the *Crab* 24-core cluster. For the main part of the thesis, 215 000 supercluster CPU-hours were provided by IT4Innovations via the *23rd Open Access*, where I have successfully applied and obtained the computational time (see Appendix A).

6.1 SMALL-SCALE SIMULATIONS

The Particle-In-Cell method provided good results in application to solar plasma in an investigation of double plasma resonance effects and electron–cyclotron maser instability (works mentioned in Section 3.3); however, it has not been used to simulate the maser phenomena in electron–positron plasma of pulsars yet.

Before a detailed investigation of the wave features of the pulsar electron–positron plasma was carried out, several simulations were performed to find the ideal setup for the studied physical phenomena. Following the theory of maser-amplified radiation (Zheleznyakov et al., 2016), the aim was to simulate plasma at a distance of a light cylinder from the pulsar (see Figure 2.3), where the mechanism of electron–positron cyclotron maser is relevant. Here, the magnetic field strength reduces to $\sim 10^6$ G. However, a magnetic field with such

strength would still be too high for the observed frequency range $f = (6 - 10)$ GHz (Hankins and Eilek, 2007). This frequency range corresponds to relatively low electron–cyclotron harmonics and is obtained for much smaller magnetic fields $B \sim 10^2$ G. This could occur in the regions of magnetic reconnection at the light cylinder distance. Assuming that the emission is generated near ω_{pe}, the estimated plasma frequency is in the range $(11.3 - 18.9)$ GHz. From that, the estimated particle number density at the source is $N \approx (0.9 - 1.2) \cdot 10^{11}\,\mathrm{cm}^{-3}$ (Zheleznyakov et al., 2016).

At first, effectively two-dimensional (3D system with two dominant axes) simulations were planned. However, the numerical resolution and required domain size needed to distinguish the amplified wave modes proved to be beyond the available computing resources at the time and will be investigated in the near future. It was therefore decided to instead conduct simulations that are effectively one-dimensional but provide much better numerical resolution in the chosen dominant direction. In all the simulations, the only nonzero component of the magnetic field is in the z axis, as the aim of the thesis is to primarily study waves that generate in the direction perpendicular to the magnetic field.

In simulations, the DGH velocity distribution function (3.8) is used, proposed for the studied region in works done by Zheleznyakov and Zlotnik (1975a) and Winglee and Dulk (1986). The distribution function describes well the characteristic behavior of particles trapped in a magnetic field, with a deficit of slow velocities and a zero mean velocity along the direction of the magnetic field. The distribution function essentially consists of background (cold) particles with characteristic thermal velocity v_{tb} and non-equilibrium thermal hot particles with their respective characteristic velocity v_{th}. The following sections show how the different values of the cyclotron frequency and characteristic velocity of the hot plasma component impact the electron–positron maser instability.

Data analysis was done using the Python libraries NumPy and SciPy. In the case of graphs of the temporal evolution of a given physical quantity, the Savitzky–Golay filter (Savitzky and Golay, 1964) is applied to the data to reduce noise. Dispersion diagrams are computed using the Fast Fourier Transform (FFT) from the SciPy library. The electric field data is averaged over the y and z directions. The Hann window function (discussed in Essenwanger, 1986) is applied to smooth the data before FFT.

6.1.1 *Varying Plasma to Cyclotron Frequency Ratios*

The double plasma resonance theory (see Section 3.2.1) is based on the resonance of the plasma frequency ω_{pe} and harmonics of the cyclotron frequency ω_{ce}. It is expected that configurations that satisfy

Table 3: Physical and computational parameters of simulations with varying plasma to cyclotron frequency ratio. Eight simulations were carried out for frequency ratio in range 10.20 - 11.76.

parameter	**value**
Domain size x,y,z	$1536 \times 12 \times 8$
particle density per cell	396
hot/background particle density ratio $n_{\mathrm{th}}/n_{\mathrm{bg}}$	1/10
time step Δt	$0.025\,\omega_{\mathrm{pe}}^{-1}$
total time steps	60 000
hot particle characteristic velocity v_{th}	$0.2\,c$
background particle thermal velocity v_{tb}	$0.03\,c$
plasma/cyclotron frequency ratio $\omega_{\mathrm{pe}}/\omega_{\mathrm{ce}}$	10.20 - 11.76

Table 4: Different subsequent configurations of setup with $\omega_{\mathrm{pe}}/\omega_{\mathrm{ce}} = 11$.

Simulation	$\omega_{\mathrm{pe}}/\omega_{\mathrm{ce}}$	$n_{\mathrm{th}}/n_{\mathrm{bg}}$	v_{th}	v_{tb}
I	11	100/1000	$0.2c$	$0.03c$
II	11	100/1000	$0.3c$	$0.03c$
III	11	100/1000	$0.2c$	$0.05c$
IV	11	333/1000	$0.2c$	$0.03c$

this condition lead to the highest growth rates of plasma instability. A set of simulations with varying plasma-cyclotron frequency ratios was carried out to demonstrate this effect, with the respective configurations listed in Table 3. The choice of physical parameters is based on the analytical theory of Zheleznyakov et al. (2016). The computational parameters, such as the domain size and duration, are based on the results of preliminary simulations. Eight simulations were conducted covering $\omega_{\mathrm{pe}}/\omega_{\mathrm{ce}}$ 10.20 to 11.76. The choice of the frequency range was based on analytical calculations by Zheleznyakov et al. (2016). The integer number ratio of 11 was in the middle of the set; 3 subsequent configurations explored the effects of increasing the ratio, while the remaining 4 configurations did the opposite.

The temporal evolution of the x component of the electric field E_x scaled to the initial kinetic energy E_{k0} for various values of $\omega_{\mathrm{pe}}/\omega_{\mathrm{ce}}$ is shown in Figure 6.1, left. It is evident that the closer to being an integer number the ratio is, the faster the instability grows. The maximum electrostatic energy is also reached in the scenario, which fulfills the resonance condition. This fact can be better visualized in Figure 6.2. Here, the values of the instability growth rate Γ and $\omega_{\mathrm{pe}}/\omega_{\mathrm{ce}}$ of each of the eight simulations are shown. Using cubic interpolation, the periodic character of Γ is evident, with its maxima being the in-

Growth rates were obtained by fitting the exponential part of the temporal evolution.

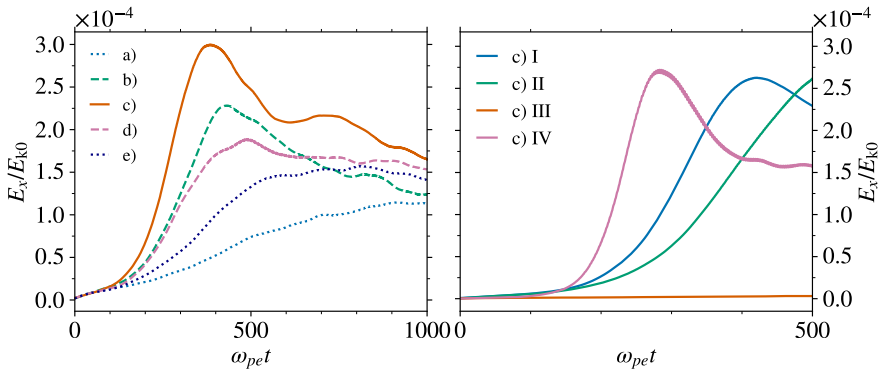

Figure 6.1: *Left*: temporal evolution of x-component of the electrostatic energy E_x scaled to the initial kinetic energy E_{k0} for electron cyclotron to plasma frequency ratio: a) 11.50; b) 11.24; c) 11.00; d) 10.75; e) 10.63. See Table 3 for configuration details. *Right*: temporal evolution of E_x/E_{k0} using the frequency ratio with the highest growth rate (case of $\omega_{pe}/\omega_{ce} = 11$) for various configurations. See Table 4 for configuration details.

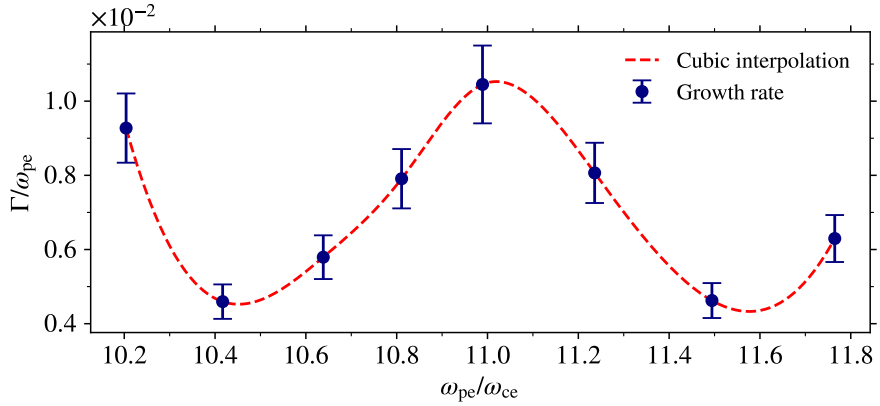

Figure 6.2: Growth rate of electrostatic energy as a function of cyclotron to plasma frequency ratio. Data points are calculated from simulations shown on Figure 6.1, left.

teger number values of ω_{pe}/ω_{ce} and the minima between them. In large-scale simulations, the wave features of $\omega_{pe}/\omega_{ce} = 11$ (the same as in test simulations), 5, and 3 (possible cases with stronger magnetic fields) are investigated.

To further study the impacts of different simulation configurations, the value of $\omega_{pe}/\omega_{ce} = 11$ was taken and studied in 4 different configurations (including the original setup) with increased particle density per cell. A simulation was computed for these configurations:

A. original setup;

B. thermal velocity of the hot component v_{th} increased from $0.2c$ to $0.3c$;

c. thermal velocity of the background component v_{th} increased from $0.03c$ to $0.05c$;

d. ratio between hot and background particle density increased from $1/10$ from $1/3$.

The configuration details of these simulations are shown in Table 4. High density is used to eliminate possible noise. The temporal evolution is displayed on Figure 6.1, right.

In the case of simulation I, which had an increased total density compared to the original setup in Figure 6.1 left, the development of the instability was similar to that of the original, with a lower maximum of the electrostatic energy. This shows that the choice of particle density does not play a key role in the way instability develops in simulations. Therefore, for subsequent larger simulations particle density of 450 per grid cell is used, an increase of roughly 15%, which is a reasonable value yielding good results while not consuming tremendous amounts of computing time.

Simulations II and III show what effect different thermal velocities of the hot/background component of the velocity distribution function do have on the evolution of the studied instability. Increasing v_{th} to $0.3c$ causes the instability to take longer to form; however, it seems that it might reach higher saturation energy than $v_{th} = 0.2c$. This is expected because the hot component, which primarily governs the behavior of the instability, carries more total energy. Since the testing simulations were short and accommodated for the original setup time–wise, the instability was not fully grown at the end of the simulations. Therefore, the configurations of different values of v_{th} were further tested in the next section. On the contrary, increasing the thermal velocity of the background plasma component from $0.03c$ to $0.05c$ completely suppresses the instability and prevents its formation.

Changing the density ratio of hot to background plasma component was tested with Simulation IV. In this configuration, the n_{th}/n_{bg} is changed from the original $1/10$ to $1/3$, effectively increasing the number of hot particles in the simulation. This simulates a scenario of high-energy plasma outflow from the inner magnetosphere. The setup yields the highest growth rate of all the configurations, and its maximum value is slightly higher than that of Simulation I, a simulation with similar particle density. The effects of different density ratios seem to play a key role in the instability development and are consequently investigated further in the large–scale simulations section.

Table 5: Computational parameters of simulations with varying value of characteristic velocity v_{th}. For each of the selected values, 5 simulations were carried out for frequency ratio in range 10.63 - 11.50. Values marked by asterisk were only computed for the fastest growing frequency ratio of 11.

parameter	**value**
Domain size x,y,z	$1536 \times 12 \times 8$
particle density per cell	1100
hot/background particle density ratio $n_{\mathrm{th}}/n_{\mathrm{bg}}$	1/10
time step Δt	$0.025\,\omega_{\mathrm{pe}}^{-1}$
total time steps	40 000
hot particle characteristic velocity v_{th}	0.15, 0.2*, 0.3, 0.5* c
background particle thermal velocity v_{tb}	$0.03\,c$
plasma/cyclotron frequency ratio $\omega_{\mathrm{pe}}/\omega_{\mathrm{ce}}$	10.63 - 11.50

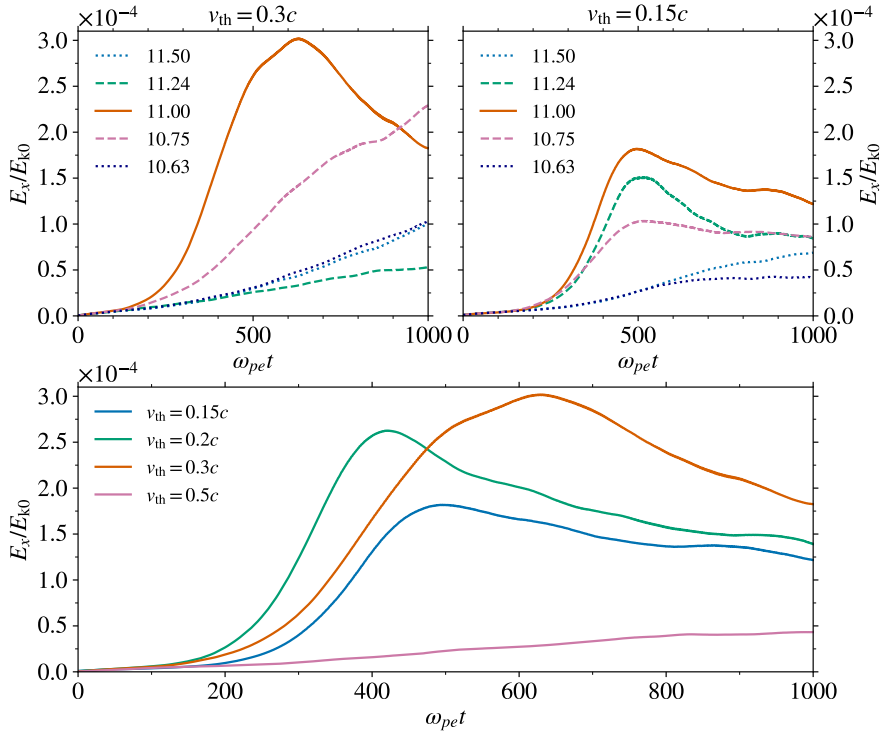

Figure 6.3: *Top left*: temporal evolution of electrostatic energy E_x scaled to initial kinetic energy E_{k0} for different values of $\omega_{\mathrm{pe}}/\omega_{\mathrm{ce}}$ with $v_{\mathrm{th}} = 0.3\,c$. *Top right*: temporal evolution of E_x/E_{k0} for different values of $\omega_{\mathrm{pe}}/\omega_{\mathrm{ce}}$ with $v_{\mathrm{th}} = 0.15\,c$. *Bottom*: temporal evolution of the fastest growing setup $\omega_{\mathrm{pe}}/\omega_{\mathrm{ce}} = 11$ for different values of v_{th}. See Table 5 for configuration details.

6.1.2 *Varying Characteristic Velocity of Hot Component*

Following the results of the previous tests, before proceeding to large–scale simulations, two additional series of simulations were performed with v_{th} being $0.15c$ and $0.3c$ covering ω_{pe}/ω_{ce} from 10.63 to 11.50. To provide an extreme case, an additional simulation with $v_{th} = 0.5c$ was computed to provide a comparison with other fastest growing configurations. The details of these simulations are listed in Table 5. Figure 6.3, top left, shows the temporal evolution of electrostatic energy E_x scaled to the initial kinetic energy E_{k0} for different values of ω_{pe}/ω_{ce} with $v_{th} = 0.3c$. Opposed to this, Figure 6.3, top right, shows the same scenario, this time with v_{th} being $0.15c$. A higher energy of the hot distribution component appears to allow for a better transformation of the kinetic energy into the electrostatic energy, since the maximum for the fastest growing mode with $\omega_{pe}/\omega_{ce} = 11$ is twice as high in the $0.3c$ case compared to the $0.15c$ setup.

However, increasing the characteristic velocity of the hot plasma component does not necessarily mean that the instability will grow more. Figure 6.3, bottom, shows the temporal evolution of E_x/E_{k0} with $\omega_{pe}/\omega_{ce} = 11$ for the characteristic velocities v_{th} of 0.15, 0.2, 0.3, and $0.5c$, respectively. The highest saturation energy is reached for $v_{th} = 0.3c$, however, its growth rate is not as high as that of the $0.2c$ setup. Although the saturation energy of the $0.15c$ configuration is not as high as that of the previously mentioned setups, the growth remains exponential.

Interestingly, in the setup with $v_{th} = 0.5c$ the instability does not form at all throughout the time scale of the simulations. The reasoning behind this behavior can be explained by looking at the velocity distribution function at times $\omega_{pe}t = 0$ and $\omega_{pe}t = 1000$ (Figure 6.4). The color scaling of the Figure 6.4 is intentionally over-saturated, so the disturbances in the hot component are better visible. Looking at the simulation with $v_{th} = 0.15c$, development in the hot component is apparent; however, the evolution of the hot part of the velocity distribution does not exhibit 'shock' patterns in the state at $\omega_{pe}t = 1000$. These are clearly distinguishable for the simulations with v_{th} being $0.2c$ and $0.3c$. The simulation with $v_{th} = 0.5c$, in which the instability does not form, shows very little development in its velocity distribution. The instability depends on the positive gradient of $v_{\perp}$ (Treumann, 2006), which is not as steep as in the previous cases. Essentially, as there are no significant developments in the velocity distribution, charged particle motion in the given state does not support the formation of a strong electric field, and thus not enough kinetic energy is transformed into the electrostatic energy.

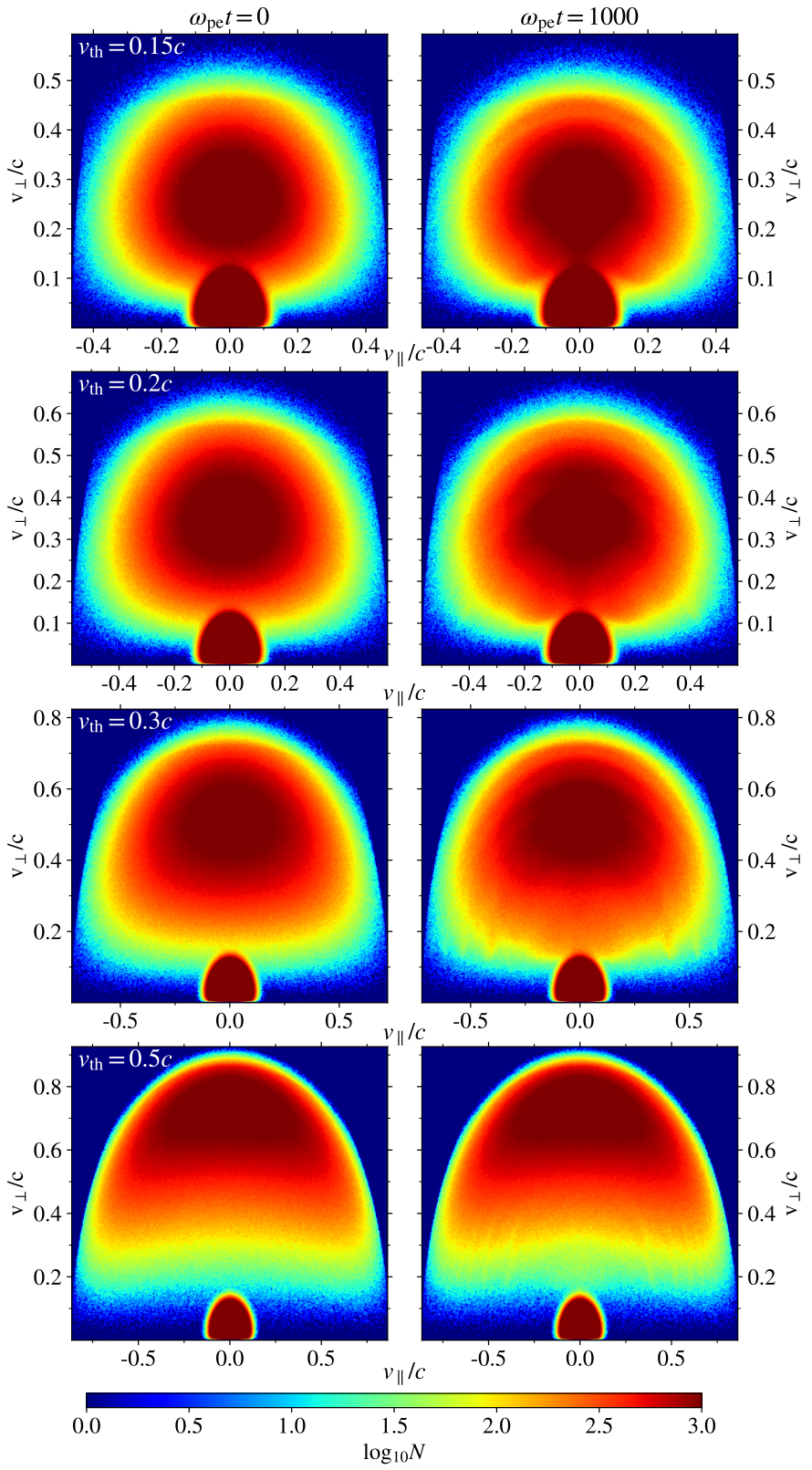

Figure 6.4: Electron velocity distributions at time $\omega_{pe}t = 0$ (left column) and $\omega_{pe}t = 1000$ (right column) for various values (rows) of characteristic velocity of the hot component v_{th}. Color indicates the logarithmic number density of simulation particles with given velocity.

6.2 LARGE-SCALE SIMULATIONS

After analyzing the results obtained from the smaller simulations discussed in previous sections, a series of simulations approximately 5 times larger were computed. The decision regarding the domain size and cell density was made to obtain sufficient resolution in the Fourier space of the simulation. The main motivation for the large–scale simulation was to investigate two important factors:

A. how does different *integer* number ratio of plasma to cyclotron frequency affect wave features?

B. what impact do different hot to background distribution components have on the dispersion of studied plasma waves?

Therefore, three different frequency ratios ω_{pe}/ω_{ce} (3, 5 and 11) were chosen and for each five simulations with a varying density ratio n_{th}/n_{bg} were computed. After the analysis of these results, the simulation configuration with the strongest wave mode was selected and subsequently computed for the referential case of electron–ion plasma. The electron–ion plasma simulation is also fundamental for the verification of the results by comparing them with the recent publications. The details of the simulations are listed in Table 6. The results of the large–scale simulations are interpreted through dispersion diagrams similar to those in Figure 3.1. Dispersion diagram is obtained through calculation of the Fourier transform for each component of electric field vector $\mathbf{E} = (E_x, E_y, E_z)$. The magnetic field has a nonzero component only in the z axis, $\mathbf{B} = (0, 0, B_z)$. Directions x and y are most important since the theory proposes the amplification of waves with perpendicular propagation to the magnetic field (see Section 3.2).

Table 6: Physical and computational parameters of larger simulations with varying values of ω_{pe}/ω_{ce} and n_{th}/n_{bg}. Configuration using values marked by asterisk was also used for a simulation of electron–ion plasma.

parameter	**value**
Domain size x,y,z	$6144 \times 12 \times 8$
particle density per cell	450
hot/background particle density ratio	1/10, 1/3, 1/2*, 1/1
time step Δt	$0.025\,\omega_{pe}^{-1}$
total time steps	60 000
hot particle characteristic velocity v_{th}	$0.2\,c$
background particle thermal velocity v_{tb}	$0.03\,c$
plasma/cyclotron frequency ratio ω_{pe}/ω_{ce}	3, 5*, 11

6.2.1 *Comparison to Electron-Ion Plasma*

With a goal of generating results comparable to recent simulations of a similar plasma environment, e.g. Ning et al. (2021) or Li et al. (2021), the configuration of the electron–positron simulation with the most remarkable wave features was simulated for the scenario of electron–ion plasma (the setup marked by an asterisk in Table 6). Figure 6.5 shows the plasma wave dispersion for electron–ion plasma (left column) and electron–positron plasma (right column). Known electron–ion plasma modes are denoted by the corresponding letter.

In the E_x dispersion of the waves in an electron–ion plasma, Bernstein (discussed in Zheleznyakov and Zlotnik, 1975a), Z, X, and O wave modes formed. Compared with the results of electron–positron plasma, even though electrostatic Bernstein waves do form at the cyclotron harmonics, on the contrary, there is no distinguishable Z and X electromagnetic modes. The Z mode in the electron–positron plasma either does not form, or it merges with the X mode. Furthermore, the ionic Z mode propagates at a frequency lower than the ω_{pe}, while the X mode at a frequency higher than ω_{pe}.

The results for the electron–ion plasma were already obtained before (simulations of solar plasma), for example in the publications stated above, therefore the simulation setup can be deemed as plausible. In contrast, the 'XZ' mode in the electron–positron simulation propagates directly at ω_{pe}. The difference between the two plasmas can be best seen in the dispersion of the electric field component E_y (Figure 6.5, middle row). Z and X modes are apparent in the electron–ion plasma. In contrast, there is either no Z mode or it merges with the X mode. This is a new result, and we will study its occurrence in further detail in the near future. Similarly to the dispersion of E_x, the X mode is above and the Z mode is below ω_{pe} in the electron–ion plasma, whereas the 'XZ' mode of the electron–positron plasma propagates directly on ω_{pe}. Both the X and the 'XZ' modes are further amplified at upper cyclotron harmonics above ω_{pe}. Moreover, an enhanced whistler mode (W) emerges at the first cyclotron harmonic in the case of an electron–positron plasma. Dispersion of E_z, which is parallel to the magnetic field, is similar for both plasmas, with only the ordinary wave mode (O).

6.2.2 *Analysis of Various Frequency and Density Ratios*

Motivated by the results obtained in small-scale simulation series that surveyed the configuration of different density and frequency ratio configurations, additional large-scale simulations exploring different combinations of these ratios were computed.

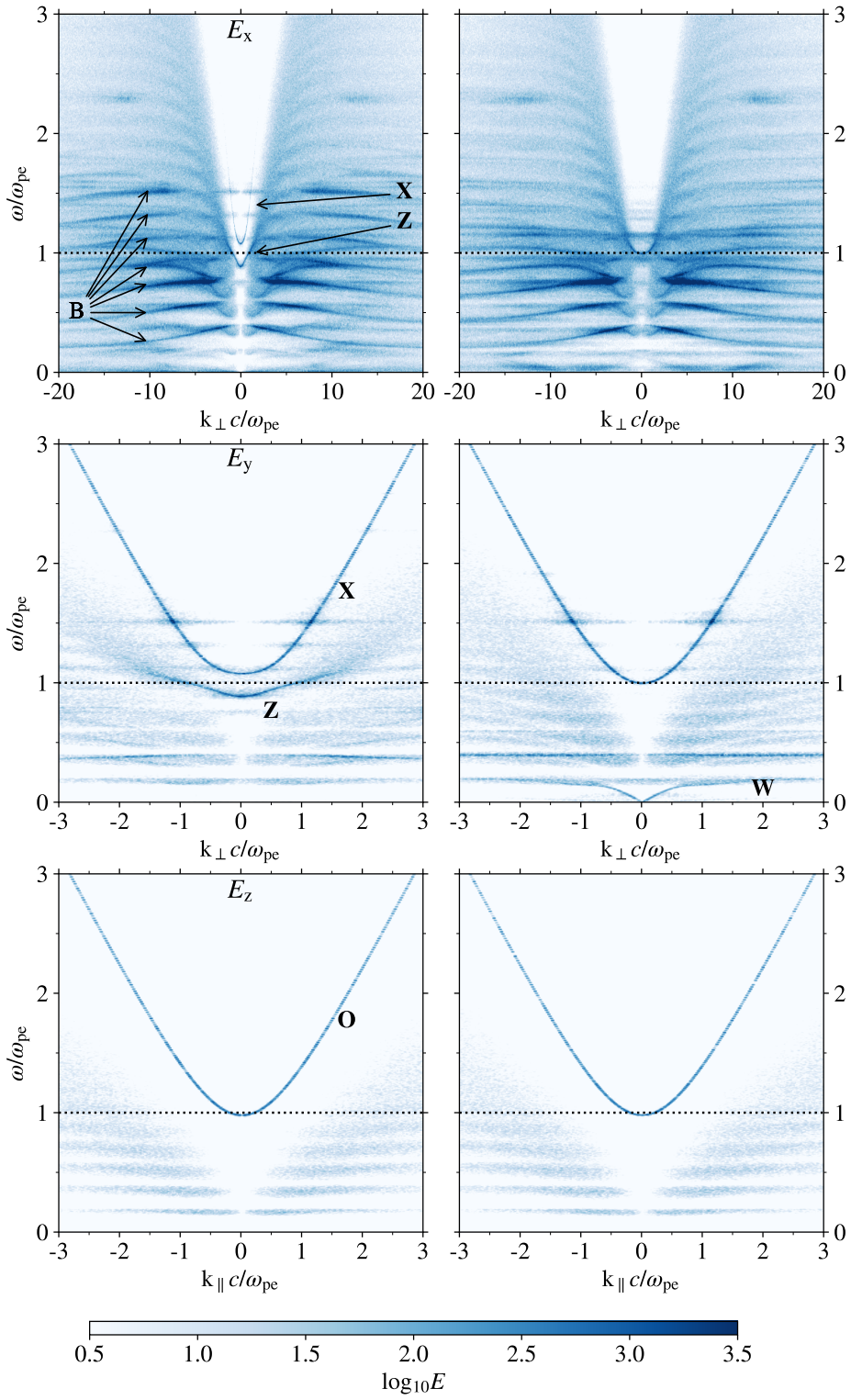

Figure 6.5: Dispersion diagrams for electron–ion plasma (left column) and electron–positron plasma (right column) with frequency ratio $\omega_{pe}/\omega_{ce} = 5$ and density ratio $n_{th}/n_{bg} = 1/2$. Rows show dispersion in the E_x, E_y, and E_z. Bernstein (B), X, Z, whistler (W), and ordinary (O) modes are denoted.

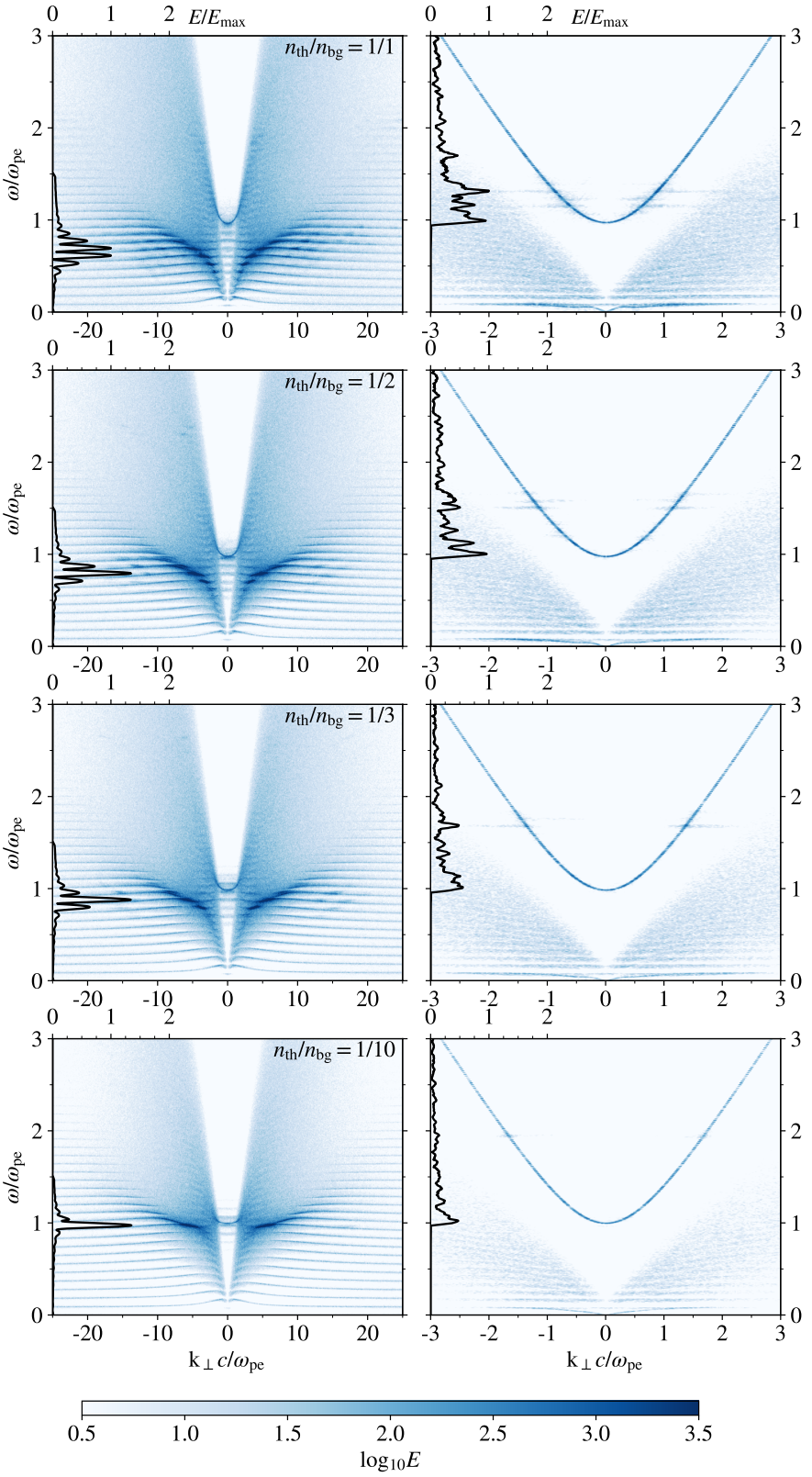

Figure 6.6: Dispersion diagrams for various values of n_h/b_{bg} with frequency ratio $\omega_{pe}/\omega_{ce} = 11$. Dispersions are overlaid with an integrated frequency profile scaled to the maximum of the top-most case.

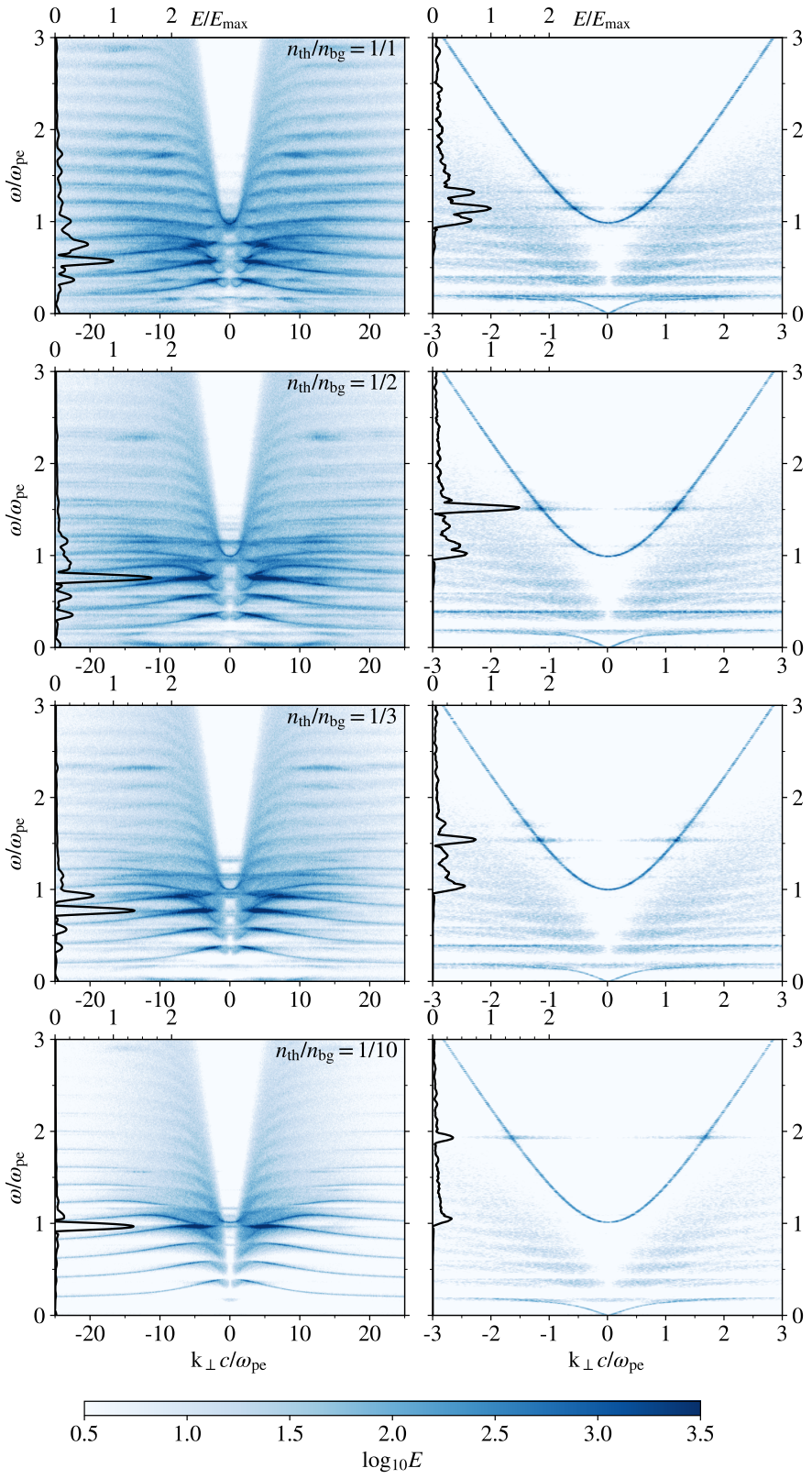

Figure 6.7: Dispersion diagrams for various values of n_h/b_{bg} with frequency ratio $\omega_{pe}/\omega_{ce} = 5$. Dispersions are overlaid with an integrated frequency profile scaled to the maximum of the top-most case.

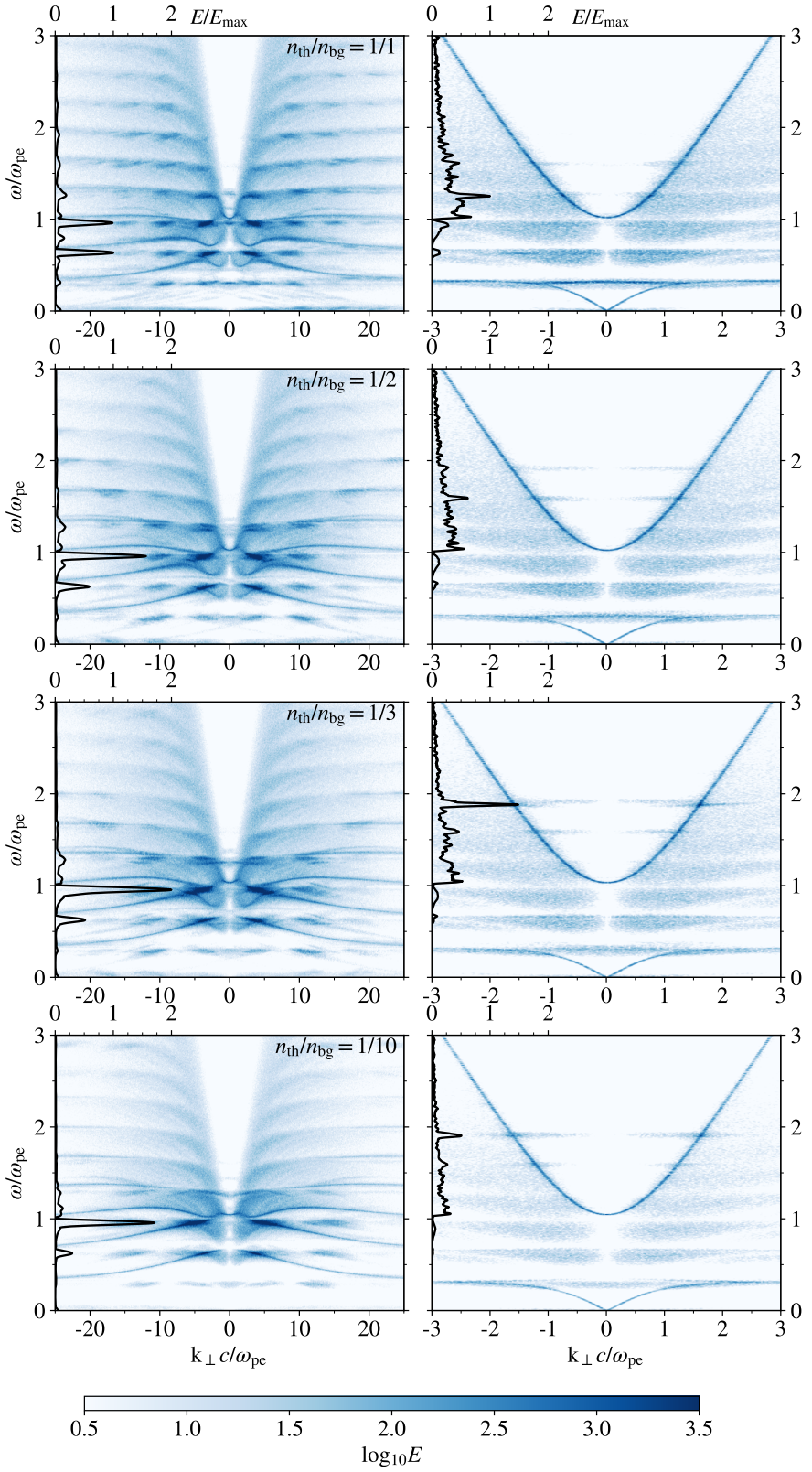

Figure 6.8: Dispersion diagrams for various values of n_h/b_{bg} with frequency ratio $\omega_{pe}/\omega_{ce} = 3$. Dispersions are overlaid with an integrated frequency profile scaled to the maximum of the top-most case.

Dispersion diagrams are shown on Figures 6.6 ($\omega_{pe}/\omega_{ce} = 11$), 6.7 ($\omega_{pe}/\omega_{ce} = 5$), and 6.8 ($\omega_{pe}/\omega_{ce} = 3$), where each row represents dispersion in E_x and E_y of the formed plasma waves for different hot to background density ratios. These configurations explore the possibility of stronger magnetic fields by decreasing the frequency ratio and scenarios of hot plasma outflow from the inner magnetosphere of the pulsar by increasing the density of the hot plasma component. The dispersion diagrams are overlaid with an integrated frequency profile of Bernstein waves for dispersion in E_x and 'XZ' mode for dispersion in E_y, each scaled to the maximum of the topmost figure. Analyzing the dispersions in the E_x, the energy carried by the Bernstein modes shifts closer to ω_{pe} with decreasing density ratio. Moreover, the number of Bernstein modes formed, in agreement with the theory, is the same as the frequency ratio. In general, the pattern of the Bernstein modes is not affected by different density ratios, and the frequency ratio directly affects the number of Bernstein modes formed. The character of dispersion in E_y is not as systematic as that of E_x.

Dispersions are highly affected by both frequency and density ratios. In the $\omega_{pe}/\omega_{ce} = 11$ scenario, peaks of the energy are located in the cyclotron harmonics above and close to ω_{pe}, with its maxima being higher the higher the density ratio is. In the $\omega_{pe}/\omega_{ce} = 5$ scenario, increasing density shifts the energy peaks to higher cyclotron harmonics; however, their maximum energy is reduced. The maximum is reached in simulation with $n_{th}/n_{bg} = 1/2$, where there is notable peak at the third cyclotron harmonic above ω_{pe}. In the most extreme scenario with $\omega_{pe}/\omega_{ce} = 3$, the energy of the 'XZ' mode is condensed between ω_{pe} and the third cyclotron harmonic. The maximum is reached in the setup with $n_{th}/n_{bg} = 1/3$, which is different from the previous cases.To further measure the output of the simulated wave modes, Bernstein modes from the E_x and 'XZ' mode from the E_y dispersion were taken and their inverse Fourier transform was computed, yielding the temporal evolution of electrostatic energy carried by given mode.

Figure 6.9 shows the temporal evolution of the Bernstein and XZ modes for simulations with $\omega_{pe}/\omega_{ce} = 11$. For the Bernstein waves, it is evident that increasing the density ratio increases the growth rate of the waves; however, the saturation energy is roughly the same for all tested density ratios. The XZ mode is energetically very weak in all cases, with only $\sim 10^{-6}$ % of the initial energy being transformed into the electrostatic energy of the XZ mode, 4 orders of magnitude lower than the energy of Bernstein waves. XZ mode in this scenario does not rise exponentially in any case, with its energy value being so low that its inverse Fourier transform might be polluted by the surrounding numerical noise.

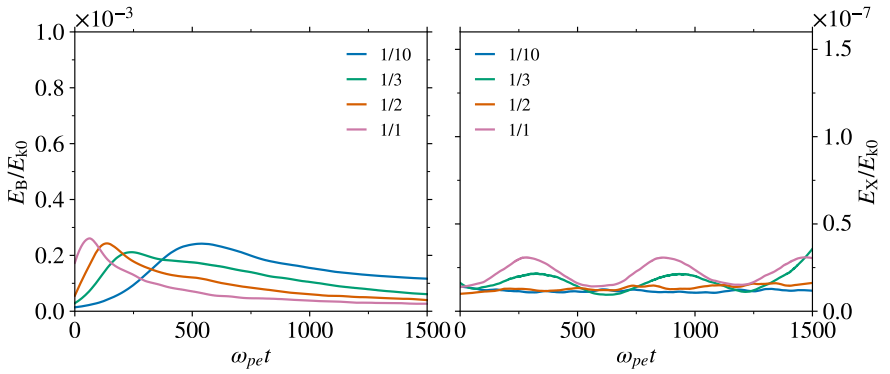

Figure 6.9: Temporal evolution of energy scaled to initial kinetic energy of Bernstein waves (left) and XZ mode (right) with frequency ratio $\omega_{pe}/\omega_{ce} = 11$ for different values of hot/background density ratio.

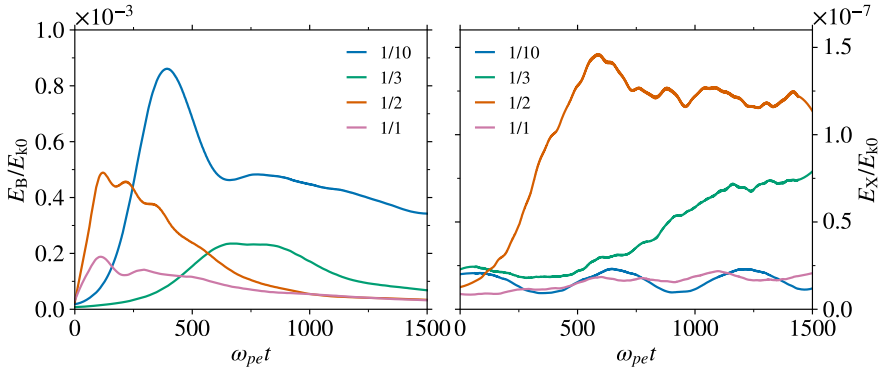

Figure 6.10: Temporal evolution of energy scaled to initial kinetic energy of Bernstein waves (left) and XZ mode (right) with frequency ratio $\omega_{pe}/\omega_{ce} = 5$ for different values of hot/background density ratio.

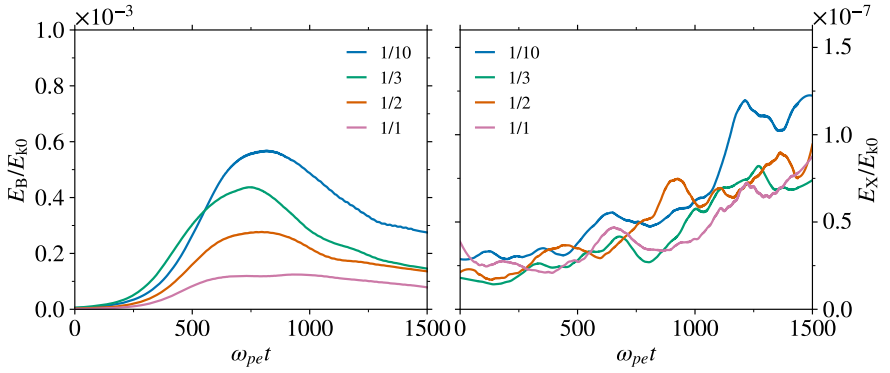

Figure 6.11: Temporal evolution of energy scaled to initial kinetic energy of Bernstein waves (left) and XZ mode (right) with frequency ratio $\omega_{pe}/\omega_{ce} = 3$ for different values of hot/background density ratio.

The temporal evolution of electrostatic Bernstein and electromagnetic 'XZ' modes in simulations with $\omega_{pe}/\omega_{ce} = 5$ is shown in Figure 6.10. Bernstein modes for all density ratios rise exponentially until they saturate and diminish. The highest saturation energy is reached in $n_{th}/n_{bg} = 1/10$, approximately four times higher than the configurations discussed above. The most interesting is the setup with $n_{th}/n_{bg} = 1/2$. Here, the Bernstein waves develop the fastest out of all setups and the XZ mode grows faster and to higher saturation energy than any other configuration. Taking the results shown in Figure 6.7, this configuration exhibits the strongest amplification at the third cyclotron harmonic above ω_{pe}. The maximum saturation energies of Bernstein waves are equal to $\sim 10^{-1}$ %, while the XZ carries $\sim 10^{-5}$ %.

To conclude the remaining simulation series, Figure 6.11 shows the temporal evolution of Bernstein and X modes in simulations with $\omega_{pe}/\omega_{ce} = 3$. Bernstein waves have similar growth rates; however, their saturation energy increases with a decreasing density ratio. All XZ modes also increase over time, most notably the setup with the density ratio $n_{th}/n_{bg} = 1/3$.

Unlike the simulation with $\omega_{pe}/\omega_{ce} = 5$ and $n_{th}/n_{bg} = 1/2$, which was strongly amplified in the third cyclotron harmonic, this setup appears to be strongly amplified in the fourth cyclotron harmonic above ω_{pe} (see Figure 6.8). Saturation energies are of similar order of magnitude as the simulations with $\omega_{pe}/\omega_{ce} = 5$.

6.2.3 *Radiative Flux Estimate*

To calculate the real physical size of the simulated system, a conversion through plasma skin depth, which is defined as

Also called electron inertial length.

$$d \equiv \frac{c}{\omega_{pe}} \approx 5.31 \cdot 10^5 \frac{1}{\sqrt{n_e}} \,\mathrm{cm}, \tag{6.1}$$

is used. In numerical units of the simulation, the numerical plasma skin depth d is

$$d = \frac{c}{\omega_{pe}} = \frac{0.5}{0.025} = 20\Delta \,(\text{grid points}).$$

Real physical value of d, using the estimated density $n_e = 10^{11}\,\mathrm{cm}^{-3}$ (Zheleznyakov et al., 2016), is therefore

$$d \approx 5.31 \cdot 10^5 \frac{1}{\sqrt{n_e}} \,\mathrm{cm} = 5.31 \cdot 10^5 \frac{1}{\sqrt{10^{11}}} \,\mathrm{cm} = 1.68 \,\mathrm{cm}.$$

Combining the results, one grid cell is approximately 0.084 cm long. The length of the dominant axis in the large-scale simulations is $\approx$ 516 cm and the total volume of the system is $\approx$ 350 cm^3.

To estimate the energy carried by the strongest simulated XZ mode (setup with $\omega_{pe}/\omega_{ce} = 5$ and $n_{th}/n_{bg} = 1/2$, Figure 6.10), an estimate of total kinetic energy is made. For this, the classical kinetic energy formula is used (relativistic effects are neglected)

$$E_k = \frac{1}{2} m_e c^2, \tag{6.2}$$

Since the density ratio between hot ($v = 0.2c$) and background ($v = 0.03c$) plasma particles is $1/2$, with the use of above stated particle density, the value of the kinetic energy density is

$$\rho(E_k) \approx 114.1\,\mathrm{J}\cdot\mathrm{m}^{-3} = 1141\,\mathrm{erg}\cdot\mathrm{cm}^{-3}.$$

Given the simulation size and kinetic energy density, the total kinetic energy of the simulation is therefore $E_k \approx 0.04\,\mathrm{J} = 4\cdot 10^5$ erg. From the Figure 6.10, it is apparent that the maximum saturation energy of the XZ mode is $\approx 1.5\cdot 10^{-7}\,E_k$. This translates to radiative flux density of $\approx 2\cdot 10^{-5}$ Jy assuming that the distance of the source is 1 kpc, the thickness of the emitting region is 5.16 m (as is in simulation), and its area is 1 km^2. This value is much lower than the observed radiative flux (Hankins and Eilek, 2007) by approximately 7 orders of magnitude. This can be partly explained by the small, effective 1D domain size, resulting in lower total energy; another cause is the low particle density of the simulations, which is responsible for the frequency widening of the peaks in wave dispersion due to the effects of numerical particle noise. Moreover, the real size of the emitting region remains uncertain.

7

DISCUSSION & FUTURE INSIGHT

Through numerical simulations of an electron–positron plasma in the outer pulsar magnetosphere, several conclusions can be drawn. Even though the phenomenon of electron–cyclotron maser and double plasma resonance was investigated by others using the Particle-In-Cell method in great detail, e.g. Benáček and Karlický (2018), Li et al. (2021), Ning et al. (2021), these works focused on the application to the solar plasma. As proposed by Zheleznyakov et al. (2016), the mechanism could be extended to the pulsar plasma as a source of coherent radio emission. However, no works have been published exploring the idea from the numerical standpoint of Particle-In-Cell simulations.

After performing a series of small-scale simulations, surveying various simulation configurations reflecting different physical scenarios of the studied system, and demonstrating the effects of electron–positron cyclotron instability driven by the double plasma resonance effect, the focus was put on performing larger simulations that would provide sufficient Fourier space resolution for detailed plasma wave dispersion analysis. Comparing the obtained results with the results presented in recent publications mentioned above, similar results were obtained from the referential electron–ion simulation; therefore, the numerical model used can be deemed plausible.

In contrast, the electron–positron simulations yielded results that were not proposed, to the best of our knowledge, by any established electron–cyclotron maser theory. The theory is based on the coalescence of amplified Z wave modes to form electromagnetic waves. However, there was no directly distinguishable Z mode in any of the simulations; instead, a new mode emerged directly at the plasma frequency, which could be X and Z modes merged into the so-called 'XZ' mode. Whether the modes merge or the Z mode does not form at all is at this point unclear. As this result is new, it will be further investigated in the near future.

Bernstein modes that formed in the electrostatic perpendicular E_x dispersion of all simulations formed consistently with their analytic theory (i.e. Zheleznyakov and Zlotnik, 1975a). It was found that a lower density ratio between the hot and background plasma components of the velocity distribution allows for greater saturation energy. The investigated electromagnetic 'XZ' modes reached notable maximum saturation energies in two different configurations: first setup with $\omega_{pe}/\omega_{ce} = 5$ and $n_{th}/n_{bg} = 1/2$; second setup with $\omega_{pe}/\omega_{ce} = 3$ and $n_{th}/n_{bg} = 1/3$. In the first setup, the third cyclotron harmonic

above the plasma frequency was strongly amplified, in the second setup, it was the fourth cyclotron harmonic instead. No wave amplification at a frequency different to one that meets the double plasma resonance condition (3.7) was recorded. The DPR theory is consistent with the simulations.

Calculations of the radiative flux, which would be observed from the simulation with the largest saturation energy of the 'XZ' electromagnetic mode, resulted in values approximately 7 orders of magnitude lower than the observed radiative fluxes. There are multiple valid reasons for the calculated radiative flux to be this low: (a) the simulations were relatively small and effective 1D; (b) low particle density causes stronger numerical noise, which leads to widening of the frequency peaks in the Fourier transform; (c) radio radiation source with a thickness of 5 m and an area of 1 km^2 was assumed. The real size of the emitting region is still uncertain.

In the very near future, even larger simulations are planned to investigate the instability in 2D with higher resolution. This would allow for an even more detailed plasma wave dispersion analysis and additionally study the wave propagation in the $(k_\perp, k_\parallel)$ space. Further plans include a comparison of possible radiation power output with the available observational data.

Part IV

APPENDIX

A

PROPOSAL

To carry out the simulations, a substantial amount of computational power was needed. We, therefore, participated in *IT4I Open Access Call 23*. Our proposal was accepted and we were given 215 000 CPU hours for our project. The proposal is included in the following pages.

IT4Innovations 23rd Open Access Call

To be submitted before: 2021-08-02 23:59:00 +0200

Name of the project: Investigation of the Pulsar Radio Emission by the means of Electron-Positron Cyclotron Maser

Number of core hours requested: 190000,25000

Multi year access: 18

Name and surname of primary investigator: Matúš Labaj

Affiliation of primary investigator: Department of Theoretical Physics and Astrophysics, Masaryk University, Kotlářská 2, 611 37 Brno, Czech Republic

e-mail: matus.labaj@mail.muni.cz

Names and surnames of other investigators[1]:

Jan Benáček, Marian Karlický

Affiliations of other investigator 1: Technical University of Berlin,

Straße des 17. Juni 135, 10623 Berlin, Germany

e-mail: benacek@tu-berlin.de

Affiliations of other investigator 2: Astronomical Institute of the Czech Academy of Sciences,

Fričova 298, 251 65 Ondřejov, Czech Republic

e-mail: karlicky@asu.cas.cz

Research area: Astrophysics

1 Comma separated list

Popular abstract:

Pulsars (from **Pulsa**ting **R**adio **S**ources) are highly magnetized neutron stars. They, together with magnetars, possess the strongest magnetic fields in the known universe. Beams of radiation in radio wavelengths are emitted out of its magnetic poles. As the star rotates, if one of the magnetic poles is pointing toward Earth, we observe the radiation in dense yet very regular periods, which are usually less than a second. This makes them the bearers of a rather poetic nickname, *the space lighthouses*.

The 1.33 second signal originating from the same location in the sky signal was first observed in 1967 by Martin Ryle and Anthony Hewish - there was no explanation, as they did not correspond with any kind of astrophysical or human-made source. In 1974, Ryle and Hewish were awarded the Nobel Prize in Physics for their discovery.

At this point, pulsars have already been studied for more than fifty years. There have been many approaches trying to explain the process of generation of the radio emission, such as curvature radiation, particle drifting in plasma, or our chosen approach, the electron-positron cyclotron maser. However, none of these processes have been described enough to fully explain the observed pulsar features. As far as we know, we are the first who want to study the electron-positron maser and its wave properties at kinetic scales to comprehend its radio emission features.

Scientific readiness:

Aims and objectives

There have been several works with a goal to explain the mechanisms and ongoing processes of pulsars throughout the last 50 years (e.g. Sturrock 1971, Lyne & Manchester 1988, Bhattacharya & van den Heuvel 1991). However, there is still no consensus on a proper emission process that contains all the features of the observed radio emission.

Observed dynamic spectra of the Crab pulsar show a distinct zebra pattern (Zheleznyakov 2016), Figure 1. It appears as equidistant parallel drifting stripes of increased intensity in certain emission frequencies. For the solar environment, this pattern has been recorded for more than 40 years in the meter and decimeter radio wavebands. Models with a zebra pattern in the solar radio spectrum were further studied by Zheleznyakov & Zlotnik 1975, Kuznetsov 2005, and Benáček & Karlický 2019.

Electron-cyclotron maser might be the source of radio emission in pulsars (Winglee & Dulk 1986) – similar to solar zebras. Considering a high ratio between plasma and cyclotron frequency (>>1), the maser emission is produced by electron interaction through harmonic resonance. Coalescence processes lead to the conversion of electrostatic waves into transverse radiation. Whether the resulting spectrum has a fine structure (observed zebra pattern) depends on the distribution of electrons.

Recent studies show that the Particle-In-Cell simulation approach is suitable for the study of solar zebra emission. Benáček & Karlický 2018, even though these simulations consisted of electron-ion plasma, shown that computing multiple single-mode and several multi-mode simulations is an efficient way of achieving desired results throughout a broad range of model parameters. Ni 2020 and Li 2021 have studied generated electromagnetic waves in detail finding that several types of electromagnetic waves can be enhanced.

As far as we know, we are the first ones to simulate the generation of radio emission in the pulsars electron-positron plasma. We want to estimate the instability growth rates, the saturation energies of the electrostatic waves using larger a set of small simulations covering range plasma temperatures and electron cyclotron-to-plasma frequencies. Then, for three selected cases we want to run a larger simulation that allows detailed study of generated electromagnetic waves.

From the numerical point of view, we want to test the newly implemented high-order solvers. Moreover, we would like to implement a GPU version of the most crucial code routines using the Fortran HIP compiler. That allows the code to run at NVIDIA as well as AMD GPUs in the future.

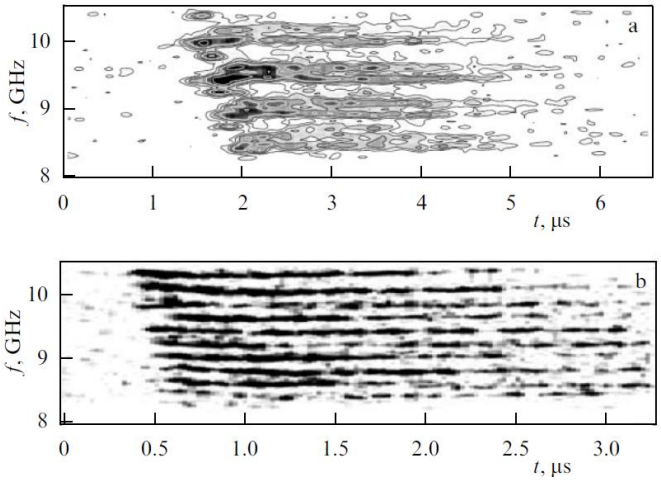

Figure 1: Examples of the dynamic spectra with the zebra pattern in the Crab pulsar microwave emission obtained with the 300 m Arecibo radio telescope with a time resolution of fractions of a nanosecond. This observation might be well explained by electron-positron maser emission (Zheleznyakov 2016).

Methods and state-of-the-art

As the pulsar radio waves are generated by coherent emission mechanisms at kinetic scales, kinetic simulations that solve the Vlasov – Maxwell set of equations for collisionless pair plasma are appropriate.

We intend to use a modified Particle-In-Cell (PIC) code TRISTAN (Matsumoto 1993). TRISTAN is a 3-dimensional, relativistic, and fully electromagnetic code. The PIC model consists of the electric and magnetic fields with a predetermined number of moving particles (electrons & positrons in our case), all represented by arrays. Initially, particles are generated via the rejection method. The time evolution of the system is computed via a self-consistent set of equations: the Lorentz equation for the particles and the Maxwell equations for the electric and magnetic fields. The particle shape function is calculated to 1st order and field solver to 2nd order approximation.

In past studies (Benáček & Karlický 2018), the model was used with full domain parallelization. The model is therefore already tested on Salomon and Anselm clusters. Our model does not majorly diverge from the previously used model. The results will be processed in Python using the NumPy and SciPy modules. The modules for computation of relevant parameters from the model outputs (energies, currents, densities, the distribution function of particles, etc.) are already prepared.

Also, we recently managed to implement computations of shape function up to 6th order and field solver up to 4th order. These higher order approaches are necessary to properly describe ultra-relativistically hot plasmas, but they are not necessary for the range of temperatures that we intend to use in our relativistic approach. Its testing and optimization is one of the aims of this proposal.

Moreover, as most of the European larger supercomputers are equipped with GPU accelerators, we plan to re-implement the most computational heavy code subroutines to HIP C++ code and use the official ROCm-hipfort compiler for an interface between the Fortran and C++ code.

Impact and outlooks

This proposal is a part of international GAČR-DFG, grant numbers GACR 20-09922J and DFG BU77-17-1. As the given area of research is largely undescribed, our study would provide a new perspective on the processes that lead to the generation of several radio emission features of pulsars. We would simulate the environment using the proposed mechanisms of electron-positron cyclotron maser. We would explicitly estimate the physical properties of the maser and compare them to the data available from observations. This would bring new insight into a modern problem. Furthermore, our study could improve the widely used TRISTAN PIC code by testing and optimizing the newly implemented computation in higher numeric orders than before and develop

the GPU version of the core. Both tasks significantly contribute to the future application of the code to larger and more precise simulations.

Computational readiness:

Computational approach, parallelization and scalability:

We intend to use the PIC code TRISTAN. Its parallelization is implemented using MPI. The model is written in Fortran 2003 and its compilation depends solely on the HDF5 ≥1.10 library, which is used for parallel and highly scalable data storage. The code is compiled using the *hdf5pf* GNU/Intel compiler. The outputs are saved on disks in predetermined time intervals (e.g., every 10 steps), therefore the results can be analyzed even during the run. Hence, the continuation or termination of the job can be decided.

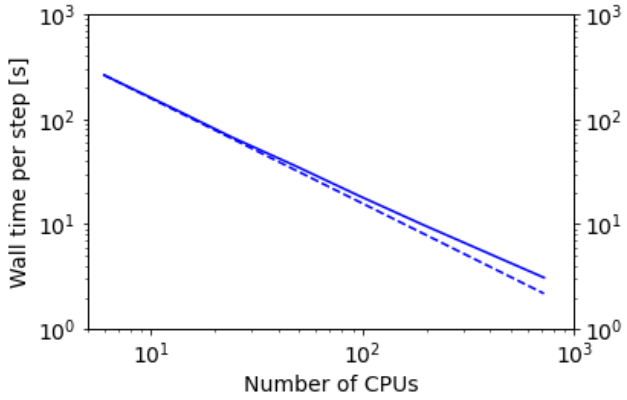

Figure 2: Scaling test of the model for simulation with a grid size 120 × 60 × 1800 and 960 PPC. Solid line represents the scaling of the parallelized model, dashed line represents the scaling of the ideal model.
For the GPU implementation we plan to use ROCm-hipfort compiler.

Computational resources:

We intend to conduct simulations in 2 cycles using 128 cores on universal nodes during the first 9 months as part of the diploma theses. In the first cycle, we plan to run 30 small simulations with different initial conditions, each with 80 000 time steps (mean time step is 0.536 s). The expected computational resources are around 1500 core hours per simulation. After the evaluation of these simulations, we would choose 3 that best define the needed initial setup for our physical phenomena (e.g., energy growth and its saturation). Then, we would simulate 3 large-scale simulations with 80 000 time steps (mean time step is 14.870 s). These simulations are expected to require around 43 000 core hours each. Therefore, simulations alone require 174 000 core hours. We expect an overhead of ~10 % for the preparation of the simulations, storage manipulation, and data analysis. In total, we request 190 000 core hours. During the second access year, we want to run 3 typical simulations for the testing of high order implementation, 5000 core hours each. For the testing of the GPU implementation, we expect to need 10000 core hours on accelerated nodes.
Our simulations require memory of ~1 GB of RAM per processor core – the nodes at IT4I fulfill this condition. Regarding the storage, the typical output (field and particles) of a small simulation would be equal to 7.5 GB. The typical output of large-scale simulation would take up to 940 GB. The expected total is therefore around 3 TB.

Economic readiness:

Socioeconomic impact:

The aims of our work are mainly scientific. Given resources would be essential to fulfill the aims of the diploma thesis (Master's degree in Astrophysics at Masaryk University, Brno, expected submission in 05/2022). The opportunity to work on one of Europe's most powerful superclusters would provide a very important experience for future research in the area of large-scale, massively parallel simulations. Furthermore, as the researched area is modern and its phenomena undescribed, the results of the simulations might be published in scientific periodicals. Finally, we intend to enhance the widely used TRISTAN PIC code by implementing more accurate computations and GPU version for future use.

References:

R. A. Dory, G. E. Guest & E. G. Harris, 1965, PhRvL, **14** 131
P. A. Sturrock, 1971, ApJ, **164** 529
V. V. Zheleznyakov & E. Y. Zlotnik, 1975, Sol Phys, **43** 431
R. M. Winglee & G.A. Dulk, 1986, ApJ, **307** 808
A. G. Lyne & R. N. Manchester, 1988, MNRAS, **234** 477
D. Bhattacharya & E. P. J. van den Heuvel, 1991, Phys. Rep., **203** 1
H. Matsumoto, Y. Omura, 1993, *Computer Space Plasma Physics: Simulation Techniques and Software*, Terra Scientific Pub. Co., Tokyo, 487, 488704111X
A. A. Kuznetsov, 2005, A&A, **438** 341
V. V. Zheleznyakov et al, 2016, Phys.-Usp., **59** 997
J. Benáček & M. Karlický, 2018, A&A, **611** A60
J. Benáček & M. Karlický, 2019, ApJ, **881**, 21
Sulan Ni et al, 2020, Apiol, **891** L25
Chuanyang Li et al, 2021, ApJL, **909** L5

B

OPTIMIZATION: SHAPE FUNCTIONS

Before the main part of the project, higher order schemes for current decomposition (Esirkepov, 2001) were implemented by Jan Benáček and subsequently tested by me. The accuracy tested was of the first (original), second, fourth, and sixth order.

Tests were carried out using the faculty cluster *Crab* simulating an arbitrary quasi one–dimensional configuration of the electron–ion plasma with an unstable distribution function. From the outputs, the temporal evolution of relevant quantities was computed to determine how efficiently each higher-order scheme preserves energy and enables the conversion of the kinetic energy into the field energy. What is evident from the results is that higher order schemes preserve total energy much better than the first order scheme. While the first-order scheme generates additional 0.025% of total E at $\omega_{\mathrm{pe}}t = 1500$, the sixth-order scheme generates only additional 0.005%, essentially five times less (Figure B.1, left).

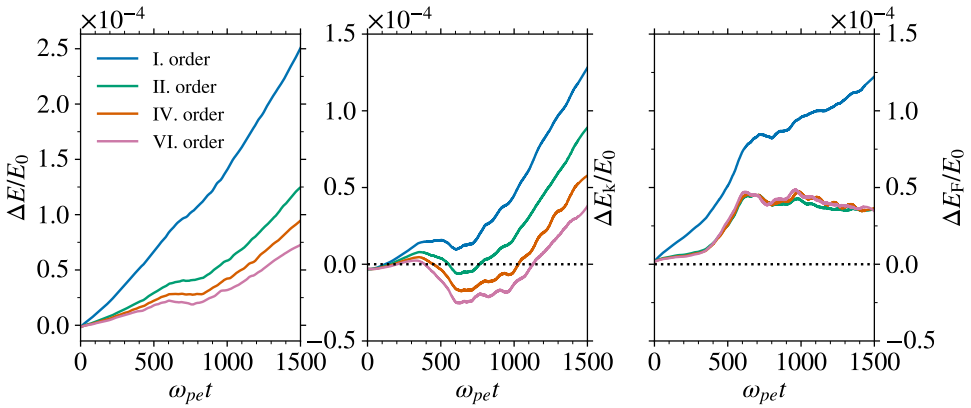

Figure B.1: Temporal evolution of physical quantities relative the initial value of total energy for different orders of accuracy of the current deposition. *Left*: total energy; *Center:* kinetic energy; *Right*: field energy.

The temporal evolution of the kinetic energy E_{k} shows a character similar to that of the total energy (Figure B.1, center). Physically, it is not expected for E_{k} to increase throughout the simulation due to its conversion into the field energy. However, due to computational limits (the simulations are small) and contributions from all directions (not just the dominant x–direction), the kinetic energy in the test simulations rises in all cases. If we took into account only the energy in the dominant x axis, the results would show a decrease that saturates at the same point as the field energy (Figure B.1, right).

In the case of field energy, apart from the first-order scheme, the temporal evolution for all cases is essentially the same. Taking only the x component of E_F into account, they are the same. The choice of a higher-order scheme, therefore, does not provide a meaningful difference as in the case of total or kinetic energy.

Even though the sixth-order scheme preserves total energy five times more efficiently than the first order, it carries a strong disadvantage. While the first order scheme takes only 0.8 seconds per time step on average, time step duration is increased to an average of 2.6 seconds when using the sixth order scheme. This increase is crucial due to the limited computational resources available. Due to this reason, we mainly choose the second order scheme with an average of 1.3 seconds per time step and comparatively accurate results. It is worth mentioning that further simulations in the main part are also much larger in domain size with much higher particle density, which makes them more accurate and less susceptible to inaccuracies possibly caused by a lower-order scheme.

INVESTIGATION OF NUMERICAL ARTIFACTS

Since the cell size in the simulation is finite, not all wavelengths can be accommodated within its limits. This is an extension of the Nyquist theorem (Nyquist, 1928), which states that to produce accurate results, the sampling frequency must be at least twice the sampled signal frequency. The computational grid is, therefore, unable to sample the waves correctly, leading to periodic energy overflows further contributing to the total energy of the system. These overflows are prominently visible in the Fourier space image of the electric field and are called numerical *artifacts*.

Figure B.2 shows the Fourier space image of the test simulations for the first, second, fourth, and sixth order scheme of current decomposition. Unwanted numerical artifacts can be seen as bright points extending toward higher frequencies. It is evident that with a higher order scheme, the creation of artifacts is suppressed. Note that the color scheme and range of the picture are over-saturated, so the artifacts are more distinguishable. Throughout the main part of the project, waves that form in the region with $k_\perp c/\omega_{pe}$ between -20 to 20 and ω/ω_{pe} of 0 to 3 are investigated. Using a simulation setup with sufficient resolution and the application of a window filter (Harris, 1978) further reduces the creation of artifacts.

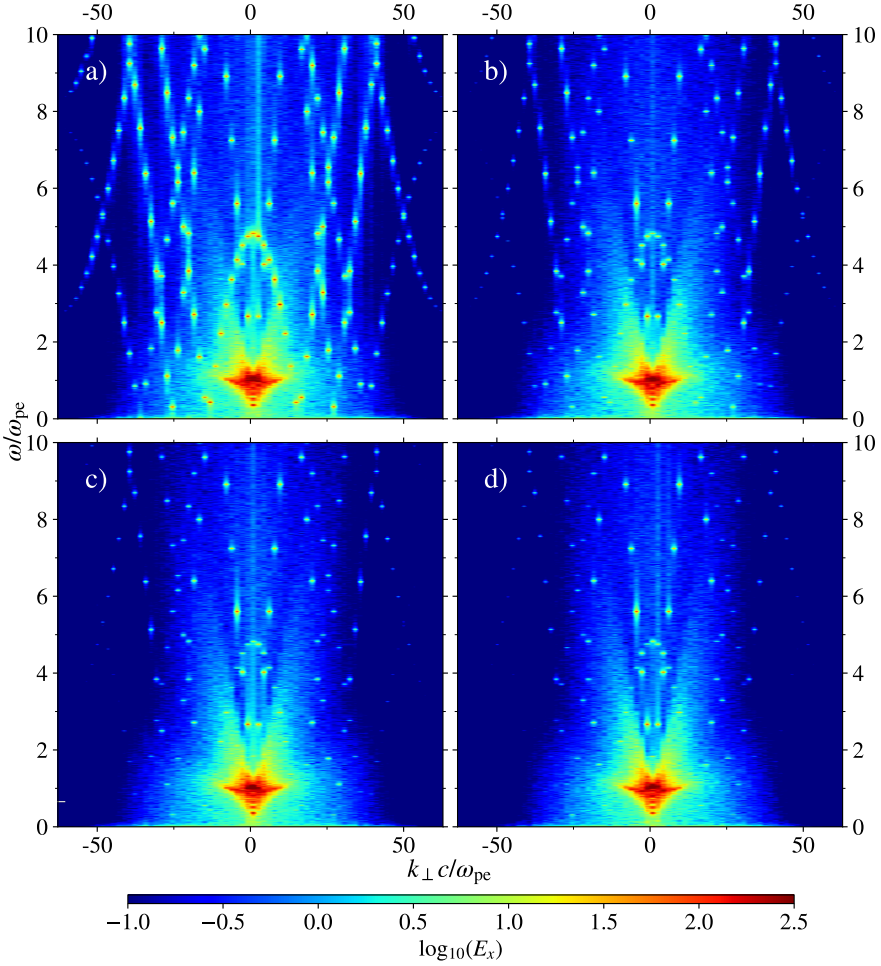

Figure B.2: Dispersion relation of the test simulation using a) first order; b) second order; c) fourth order; d) sixth order of accuracy of field solver. Progressively less bright points with increasing order of accuracy are numerical artifacts with no physical counterpart.

BIBLIOGRAPHY

[1]E. Aliu, H. Anderhub, L. A. Antonelli, P. Antoranz, M. Backes, C. Baixeras, J. A. Barrio, H. Bartko, B. et. al., and MAGIC Collaboration, "Observation of Pulsed γ-Rays Above 25 GeV from the Crab Pulsar with MAGIC," Science **322**, 1221 (2008).

[2]W. Baade and F. Zwicky, "On Super-novae," Proceedings of the National Academy of Science **20**, 254–259 (1934).

[3]D. C. Backer, S. R. Kulkarni, and J. H. Taylor, "Timing observations of the millisecond pulsar.," Nature **301**, 314–315 (1983).

[4]J. Benáček and M. Karlický, "Double plasma resonance instability as a source of solar zebra emission," Astronomy and Astrophysics **611**, A60, A60 (2018).

[5]J. Benáček, "Particle-in-cell simulations and analytical study of the proesses generating radio solar bursts," PhD thesis (Masaryk University, 2019).

[6]D. Bhattacharya and E. P. J. van den Heuvel, "Formation and evolution of binary and millisecond radio pulsars," Physics Reports **203**, 1–124 (1991).

[7]C. Birdsall and A. Langdon, *Plasma physics via computer simulation (1st ed.)* (CRC Press, 1991).

[8]J. P. Boris, "Acceleration calculation from a scalar potential," (1970).

[9]C. B. Boyle, "Mass transfer and accretion in close binaries: A review," Vistas in Astronomy **27**, 149–169 (1984).

[10]K. G. Budden, "Book-Review - the Propagation of Radio Waves - the Theory of Radio Waves of Low Power in the Ionosphere and Magnetosphere," Science **242**, 1452 (1988).

[11]O. Buneman, T. Neubert, and K. Nishikawa, *TRISTAN: TRIdimensional STANford code*, Aug. 1993.

[12]C. Y. Cardall, M. Prakash, and J. M. Lattimer, "Effects of Strong Magnetic Fields on Neutron Star Structure," Astrophysical Journal **554**, 322–339 (2001).

[13]B. Cerutti, *The Zeltron Code*, Online; Accessed from `https://ipag.osug.fr/~ceruttbe/Zeltron/index.html`, 2015.

[14]H.-H. Chen, M. A. Ruderman, and P. G. Sutherland, "Structure of Solid Iron in Superstrong Neutron-Star Magnetic Fields," Astrophysical Journal **191**, 473–478 (1974).

[15]K. R. Chu and J. Hirshfield, "Comparative study of the axial and azimuthal bunching mechanisms in electromagnetic cyclotron instabilities," The Physics of Fluids **21**, 461–466 (1978).

[16]R. Courant, K. Friedrichs, and H. Lewy, "Über die partiellen Differenzengleichungen der mathematischen Physik," Mathematische Annalen **100**, 32–74 (1928).

[17]J. M. Dawson, "Particle simulation of plasmas," Rev. Mod. Phys. **55**, 403–447 (1983).

[18]R. A. Dory, G. E. Guest, and E. G. Harris, "Unstable electrostatic plasma waves propagating perpendicular to a magnetic field," Phys. Rev. Lett. **14**, 131–133 (1965).

[19]Ø. Elgarøy, "Studies in high-resolution spectrometry of solar radio emission," Astrophysica Norvegica **7**, 123 (1961).

[20]T. Esirkepov, "Exact charge conservation scheme for particle-in-cell simulation with an arbitrary form-factor," Computer Physics Communications **135**, 144–153 (2001).

[21]O. Essenwanger, *Elements of statistical analysis*, General climatology (Elsevier, 1986).

[22]R. Giacconi, H. Gursky, E. Kellogg, E. Schreier, and H. Tananbaum, "Discovery of Periodic X-Ray Pulsations in Centaurus X-3 from UHURU," Astrophysical Journal **167**, L67 (1971).

[23]V. L. Ginzburg and S. I. Syrovatskii, "Cosmic Magnetobremsstrahlung (synchrotron Radiation)," Annual Review of Astronomy and Astrophysics **3**, 297 (1965).

[24]V. L. Ginzburg and V. V. Zheleznyakov, "On Coherent Mechanisms of Emission and their Application to Pulsars II. Maser Mechanisms of Radiation," Comments on Astrophysics and Space Physics **2**, 197 (1970).

[25]N. K. Glendenning, "First-order phase transitions with more than one conserved charge: Consequences for neutron stars," Physical Review D **46**, 1274–1287 (1992).

[26]P. Goldreich and W. H. Julian, "Pulsar Electrodynamics," Astrophysical Journal **157**, 869 (1969).

[27]A. V. Gurevich, V. S. Beskin, and Y. N. Istomin, *Physics of the pulsar magnetosphere* (Cambridge University Press, 1993).

[28]S. Hahn, K. Kim, K. Kim, X. Hu, T. Painter, I. Dixon, S. Kim, K. R. Bhattarai, S. Noguchi, J. Jaroszynski, and D. C. Larbalestier, "45.5-tesla direct-current magnetic field generated with a high-temperature superconducting magnet," Nature **570**, 496–499 (2019).

[29]T. H. Hankins and J. A. Eilek, "Radio Emission Signatures in the Crab Pulsar," Astrophysical Journal **670**, 693–701 (2007).

[30]T. H. Hankins and J. M. Rankin, "Arecibo Multi-Frequency Time-Aligned Pulsar Average-Profile and Polarization Database," Astronomical Journal **139**, 168–175 (2010).

[31]F. Harris, "On the use of windows for harmonic analysis with the discrete fourier transform," Proceedings of the IEEE **66**, 51–83 (1978).

[32]J. W. T. Hessels, S. M. Ransom, I. H. Stairs, P. C. C. Freire, V. M. Kaspi, and F. Camilo, "A radio pulsar spinning at 716 hz," Science **311**, 1901–1904 (2006).

[33]J. Hester, *Combined X-ray and Optical Images of the Crab Nebula*, Online; Accessed from: `https://hubblesite.org/contents/media/images/2002/24/1248-Image.html`, 2002.

[34]A. Hewish, S. J. Bell, J. D. H. Pilkington, P. F. Scott, and R. A. Collins, "Observation of a Rapidly Pulsating Radio Source," Nature **217**, 709–713 (1968).

[35]J. S. Hey, S. J. Parsons, and J. W. Phillips, "An Investigation of Galactic Radiation in the Radio Spectrum," Proceedings of the Royal Society of London Series A **192**, 425–445 (1948).

[36]R. Hockney and J. Eastwood, *Computer simulation using particles* (CRC Press, 1988).

[37]F. Hoyle, J. V. Narlikar, and J. A. Wheeler, "Electromagnetic Waves from Very Dense Stars," Nature **203**, 914–916 (1964).

[38]R. A. Hulse and J. H. Taylor, "Discovery of a pulsar in a binary system.," Astrophysical Journal Letters **195**, L51–L53 (1975).

[39]M. Karlický, "Radio continua modulated by waves: Zebra patterns in solar and pulsar radio spectra?" Astronomy and Astrophysics **552**, A90, A90 (2013).

[40]M. Kramer, K. M. Xilouris, D. R. Lorimer, O. Doroshenko, A. Jessner, R. Wielebinski, A. Wolszczan, and F. Camilo, "The Characteristics of Millisecond Pulsar Emission. I. Spectra, Pulse Shapes, and the Beaming Fraction," Astrophysical Journal **501**, 270–285 (1998).

[41]M. Labaj, "Particle-In-Cell Simulation of the Thermal Front," Bachelor's Thesis (Masaryk University, 2020).

[42]M. L. Large and A. E. Vaughan, "A search of the galactic plane for high dispersion pulsars," Monthly Notices of the Royal Astronomical Society **151**, 277 (1971).

[43]J. M. Lattimer and M. Prakash, "Neutron Star Structure and the Equation of State," Astrophysical Journal **550**, 426–442 (2001).

[44]C. Li, Y. Chen, S. Ni, B. Tan, H. Ning, and Z. Zhang, "PIC Simulation of Double Plasma Resonance and Zebra Pattern of Solar Radio Bursts," Astrophysical Journal Letters **909**, L5, L5 (2021).

[45]D. Lorimer, N. Roberts, and e. a. Kramer M., *Handbook of pulsar astronomy*, Cambridge Observing Handbooks for Research Astronomers (Cambridge University Press, 2005).

[46]A. G. Lyne and F. G. Smith, "Linear Polarization in Pulsating Radio Sources," Nature **218**, 124–126 (1968).

[47] A. Lyne and F. Graham-Smith, *Pulsar astronomy*, 4th ed., Cambridge Astrophysics (Cambridge University Press, 2012).

[48] M. Lyutikov, "On generation of Crab giant pulses," Monthly Notices of the Royal Astronomical Society **381**, 1190–1196 (2007).

[49] R. N. Manchester, "50 years of pulsars!" Journal of Physics: Conference Series **932**, 012001 (2017).

[50] H. Matsumoto and Y Omura, *Computer Space Plasma Physics: Simulation Techniques and Software* (Terra Scientific Pub. Co., 1993).

[51] D. B. Melrose, G. A. Dulk, and D. E. Gary, "Corrected formula for the polarization of second harmonic plasma emission," Proc. Astron. Soc. Australia **4**, 50–53 (1980).

[52] F. C. Michel, "The state of pulsar theory," Advances in Space Research **33**, 542–551 (2004).

[53] A. B. Mikhailovsky, "Present Status of the Theory of Plasma Instabilities," Advances in Plasma Physics **5**, 121 (1974).

[54] H. Ning, Y. Chen, S. Ni, C. Li, Z. Zhang, X. Kong, and M. Yousefzadeh, "Harmonic Maser Emissions from Electrons with Loss-cone Distribution in Solar Active Regions," Astrophysical Journal Letters **920**, L40, L40 (2021).

[55] H. Nyquist, "Certain topics in telegraph transmission theory," Transactions of the American Institute of Electrical Engineers **47**, 617–644 (1928).

[56] J. R. Oppenheimer and G. M. Volkoff, "On massive neutron cores," Phys. Rev. **55**, 374–381 (1939).

[57] F. Pacini, "Energy Emission from a Neutron Star," Nature **216**, 567–568 (1967).

[58] L. D. Pearlstein, M. N. Rosenbluth, and D. B. Chang, "High-Frequency "Loss-Cone" Flute Instabilities Inherent to Two-Component Plasmas," Physics of Fluids **9**, 953–956 (1966).

[59] C. J. Pethick and D. G. Ravenhall, "Nuclear physics of dense matter," Annals of the New York Academy of Sciences **647**, 503–509 (1991).

[60] C. Sagan, *Cosmos*, Cognitive systems monographs (Ballantine Books, 1985).

[61] A. Savitzky and M. J. E. Golay, "Smoothing and differentiation of data by simplified least squares procedures.," Analytical Chemistry **36**, 1627–1639 (1964).

[62] J. Schneider, "Stimulated Emission of Radiation by Relativistic Electrons in a Magnetic Field," Physical Review Letters **2**, 504–505 (1959).

[63] M. Shalaby, A. E. Broderick, P. Chang, C. Pfrommer, A. Lamberts, and E. Puchwein, "SHARP: a spatially higher-order, relativistic particle-in-cell code," The Astrophysical Journal **841**, 52 (2017).

[64]S. Shostak, *Arecibo Observatory Archive*, Online; Accessed from: https://www.nature.com/articles/d41586-020-03421-y, 1981.

[65]I. H. Stairs, "Pulsars in Binary Systems: Probing Binary Stellar Evolution and General Relativity," Science **304**, 547–552 (2004).

[66]P. A. Sturrock, "A Model of Pulsars," Astronomical Journal **164**, 529 (1971).

[67]R. A. Treumann, "The electron-cyclotron maser for astrophysical application," The Astronomy and Astrophysics Review **13**, 229–315 (2006).

[68]D. Tskhakaya, K. Matyash, R. Schneider, and F. Taccogna, "The Particle-In-Cell Method," Contributions to Plasma Physics **47**, 563–594 (2007).

[69]V. N. Tsytovich, "Nonlinear effects in a plasma," Soviet Physics Uspekhi **9**, 805–836 (1967).

[70]R. Q. Twiss, "Radiation Transfer and the Possibility of Negative Absorption in Radio Astronomy," Australian Journal of Physics **11**, 564 (1958).

[71]J. Villasenor and O. Buneman, "Rigorous charge conservation for local electromagnetic field solvers," Computer Physics Communications **69**, 306–316 (1992).

[72]Wikipedia, *Faraday Effect*, Online; Accessed from: https://en.wikipedia.org/wiki/Faraday_rotator, 2007.

[73]R. M. Winglee and G. A. Dulk, "The Electron-Cyclotron Maser Instability as a Source of Plasma Radiation," Astrophysical Journal **307**, 808 (1986).

[74]R. Winglee, "Interrelation between azimuthal bunching and semirelativistic maser cyclotron instabilities," Plasma Physics **25**, 217 (1983).

[75]A. Wolszczan and D. A. Frail, "A planetary system around the millisecond pulsar PSR1257 + 12," Nature **355**, 145–147 (1992).

[76]C. S. Wu and L. C. Lee, "A theory of the terrestrial kilometric radiation.," Astrophysical Journal **230**, 621–626 (1979).

[77]K. Yee, "Numerical solution of inital boundary value problems involving maxwell's equations in isotropic media," IEEE Transactions on Antennas and Propagation **14**, 302–307 (1966).

[78]M. D. Young, R. N. Manchester, and S. Johnston, "A radio pulsar with an 8.5-second period that challenges emission models," Nature **400**, 848–849 (1999).

[79]V. V. Zheleznyakov and V. E. Shaposhnikov, "Origin of quasi-harmonic emission bands with fine structure in the dynamic spectra of high-frequency interpulses of the Crab pulsar," Monthly Notices of the Royal Astronomical Society **495**, 3715–3721 (2020).

[80]V. V. Zheleznyakov and E. Y. Zlotnik, "Cyclotron Wave Instability in the Corona and Origin of Solar Radio Emission with Fine Structure. I: Bernstein Modes and Plasma Waves in a Hybrid Band," Solar Physics **43**, 431–451 (1975).

[81]V. V. Zheleznyakov and E. Y. Zlotnik, "Cyclotron Wave Instability in the Corona and Origin of Solar Radio Emission with Fine Structure. II: Origin of 'Tadpoles'," Solar Physics **44**, 447–459 (1975).

[82]V. V. Zheleznyakov and E. Y. Zlotnik, "Cyclotron wave instability in the corona and origin of solar radio emission with fine structure. III. Origin of zebra-pattern.," Solar Physics **44**, 461–470 (1975).

[83]V. Zheleznyakov, E. Zlotnik, V. Zaitsev, and V. Shaposhnikov, "Double plasma resonance and its manifestations in radio astronomy," Uspekhi Fizicheskih Nauk **186**, 10.3367/UFNr.2016.05.037813 (2016).

[84]E. Y. Zlotnik, V. V. Zaitsev, and A. T. Altyntsev, "On Polarization of the Zebra Pattern in Solar Radio Emission," Solar Physics **289**, 233–249 (2014).

[85]E. Y. Zlotnik, V. V. Zaitsev, H. Aurass, G. Mann, and A. Hofmann, "Solar type IV burst spectral fine structures. II. Source model," Astronomy and Astrophysics **410**, 1011–1022 (2003).